Downloaded from orbit.dtu.dk on: Dec 19, 2017

Technical University of Denmark

Quantum Dot Devices for Optical Signal Processing

Chen, Yaohui; Mørk, Jesper; Öhman, Filip; Poel, Mike van der

Publication date:
2010

Document Version
Publisher's PDF, also known as Version of record

Link back to DTU Orbit

Citation (APA):
Chen, Y., Mørk, J., Öhman, F., & Poel, M. V. D. (2010). Quantum Dot Devices for Optical Signal Processing. Kgs. Lyngby, Denmark: Technical University of Denmark (DTU).

DTU Library
Technical Information Center of Denmark

General rights
Copyright and moral rights for the publications made accessible in the public portal are retained by the authors and/or other copyright owners and it is a condition of accessing publications that users recognise and abide by the legal requirements associated with these rights.

- Users may download and print one copy of any publication from the public portal for the purpose of private study or research.
- You may not further distribute the material or use it for any profit-making activity or commercial gain
- You may freely distribute the URL identifying the publication in the public portal

If you believe that this document breaches copyright please contact us providing details, and we will remove access to the work immediately and investigate your claim.

Technical University of Denmark

Quantum Dot Devices for Optical Signal Processing

Yaohui Chen

DTU Fotonik
Department of Photonics Engineering
Technical University of Denmark

July 16, 2010
Rev. 1.0 January, 2011

DTU Fotonik
Department of Photonics Engineering

All the models are false, but some are useful...

Abstract

This thesis describes the physics and applications of quantum dot semiconductor optical amplifiers through numerical simulations. As nano-structured materials with zero-dimensional quantum confinement, semiconductor quantum dot material provides a number of unique physical properties compared with other semiconductor materials. The understanding of such properties is important in order to improve the performance of existing devices and to trigger the development of new semiconductor devices for different optical signal processing functionalities in the future.

We present a detailed quantum dot semiconductor optical amplifier model incorporating a carrier dynamics rate equation model for quantum dots with inhomogeneous broadening as well as equations describing propagation. A phenomenological description has been used to model the intradot electron scattering between discrete quantum dot states and the continuum. Additional to the conventional time-domain modeling scheme, a small-signal perturbation analysis has been used to assist the investigation of harmonic modulation properties.

The static properties of quantum dot devices, for example high saturation power, have been quantitatively analyzed. Additional to the static linear amplification properties, we focus on exploring the gain dynamics on the time scale ranging from sub-picosecond to nanosecond. In terms of optical signals that have been investigated, one is the simple sinusoidally modulated optical carrier with a typical modulation frequency range of 1-100 gigahertz. Our simulations reveal the role of ultrafast intradot carrier dynamics in enhancing modulation bandwidth of quantum dot semiconductor optical amplifiers. Moreover, the corresponding coherent gain response also provides rich dispersion contents over a broad bandwidth. One important implementation is recently boosted by the research in slow light. The idea is

to migrate such dynamical gain knowledge for the investigation of microwave phase shifter based on semiconductor optical waveguide. Our study reveals that phase shifting based on the conventional semiconductor optical amplifier is fundamentally limited over a narrow bandwidth determined by the slow carrier density pulsation processes. In contrast, we predict that using quantum dots as the active material instead can provide bandwidth enhancement even beyond 100 gigahertz due to its unique extra ultrafast carrier dynamics.

We also investigate the gain dynamics in the presence of pulsed signals, in particular the steady gain response to a periodic pulse trains with various time periods. Additional to the analysis of high speed patterning free amplification up to 150-200 Gb/s in quantum dot semiconductor optical amplifiers, we discuss the possibility to realize a compact high-speed all-optical regenerator by incorporating a quantum dot absorption section in an amplifier structure.

Resumé

Denne afhandling beskriver, gennem numeriske simuleringer, fysikken bag og anvendelserne af kvantepunkts-optiske forstærkere. Kvantepunkter er nanostrukturerede halvledermaterialer der, i sammenligning med andre halvledermaterialer, besidder en række unikke fysiske egenskaber. Forståelsen af disse egenskaber er vigtig for at forbedre effektiviteten af eksisterende udstyr og for at muliggøre udviklingen af nye halvlederkomponenter til optisk signalbehandling i fremtiden.

Vi præsenterer en detaljeret model af en halvleder kvantepunkts-optisk forstærker med indbygget ladningsbærerdynamik baseret på rate ligninger for kvantepunkter med inhomogen forbredning og ligninger til at beskrive lysudbredelse. En fænomenologisk beskrivelse benyttes til at simulere intrapunkts elektronspredning mellem diskrete kvantepunktstilstande og kontinuummet. Udover konventionel tidsdomænemodellering benyttes en perturbations analyse for små signaler til at analysere forstærkning af signaler med harmonisk modulation.

De statiske egenskaber af kvantepunkts-komponenter, f.eks høj mætningseffekt, er blevet kvantitativt analyseret. Udover forstærkeregenskaber i det lineære regime, udforsker vi forstærkerdynamik på tidsskalaer der strækker sig fra sub-picosekunder til nanosekunder. Blandt de optiske signaler der undersøges er simple sinusformer med typiske modulationsfrekvenser i området 1-100 gigahertz. Vores simulationer afslører at ultrahurtig intrapunkts-ladningsbærerdynamik kan være medvirkende til en øget modulationsbåndbredde. Det tilhørende kohærente forstærkerrespons resulterer desuden i en kompleks dispersion over en stor båndbredde. En vigtig anvendelse er for nyligt blevet promoveret gennem forskning i langsomt lys. Idéen er her at overføre viden om dynamisk forstærkning til brug i faseskiftere i halvleder-optiske bølgeledere designet til mikrobølgeområdet. Vores undersøgelse viser, at

faseskift baseret på konventionelle optiske halvlederforstærkere er grundlæggende begrænset til en relativt smal båndbredde, der bestemmes af langsomme pulserende processer i ladningsbærertætheden. I modsætning hertil forudsiger vi at brugen af kvantepunkter som det aktive materiale kan lede til en forøget båndbredde på 100 gigahertz eller mere på grund af den unikke hurtige ladningsbærerdynamik.

Vi undersøger endvidere forstærkerdynamik ved pulsede signaler specielt forstærkerrespons ved konstant forstærkning af et periodisk puls-tog med variabel periode. Udover analysen af mønsterfri højhastighedsforstærkning op til 150-200 Gb/s i kvantepunkts-optiske forstærkere diskuterer vi mulighederne for at realisere kompakte højhastigheds regeneratorer ved at inkludere sektioner med absorption i en forstærkerstruktur baseret på halvleder kvantepunkter.

Acknowledgements

I would like to thank my supervisors Jesper Mørk, Filip Öhman and Mike van der Poel. In particular, Jesper for the concrete support and theoretical guidance in my entire PhD study, Filip and Mike for the experimental discussion and sharing research, teaching and even soaring experiences in the beginning of my PhD studies. I appreciate their inspiration and encouragement to my study and life.

In addition, I'm grateful to all the people at DTU Fotonik, or formerly COM, for creating a pleasant and positive atmosphere. A great number of colleagues are thanked for joint efforts in the lab, helpful scientific discussions, traveling companionships and all the non-scientific stuff. In particular, I would like to thank Weiqi Xue, Lei Wei, Per Lunnemann Hansen, Ek Sara, Philip Trøst Kristensen, Søren Blaaberg and Kresten Yvind. Philip Trøst Kristensen for sharing office space, beer and croquet. Moreover, I would like to thank all my friends for the understanding and support.

Last, but not least, I would like to thank my parents for their ongoing support during my studies and Jun for being there with me.

Kgs. Lyngby 16/07/2010

Yaohui Chen

List of Abbreviations

1D	One Dimensional
2D	Two Dimensional
3D	Three Dimensional
2R regeneration	Re-amplification + Re-shaping
AC	Alternating Current
AM	Amplitude Modulation
ASE	Amplified Spontaneous Emission
B states	Barrier states
CDP	Carrier Density Pulsation
CH	Carrier Heating
CPO	Coherent Population Oscillations
CRE	Carrier Rate Equations
CW	Continuous Wave
DC	Direct Current
DFB	Distributed Feedback Laser
DME	Density Matrix Equations
DOS	Density Of States
EA	Electro Absorber
EIT	Electromagnetically Induced Transparency
E state	Excited state
FBG	Fiber Bragg Grating
FWHM	Full Width at Half Maximum

FWM	Four Wave Mixing
G state	Ground state
MPREM	Multi Population Rate Equation Model
ODE	Ordinary Differential Equation
PM	Phase Modulation
PRBS	Pseudo Random Binary Sequence
QCSE	Quantum-Confined Stark Effect
QD	Quantum Dot
QW	Quantum Well
R states	Reservoir states
RHS	Right Hand Side
RF	Radio Frequency
SHB	Spectral Hole Burning
SK growth	Stranski-Krastanow growth
SOA	Semiconductor Optical Amaplifier
STM	Scanning Tunneling Microscope
TPA	Two-Photon Absorption
WL	Wetting Layer
XAM	Cross Absorption Modulation
XGM	Cross Gain Modulation
XPM	Cross Phase Modulation

Contents

1 Introduction 1

2 Background 5

2.1 Quantum Dot Semiconductor Optical Amplifiers (QD SOAs) 5

2.2 Applications in Optical Signal Processing 11

2.2.1 Controlling the speed of light 11

2.2.2 Optical signal regeneration 17

3 Fundamentals of Light Matter Interaction in Semiconductors 21

3.1 Semiclassical Density Matrix Equations (DME) 22

3.1.1 Descriptions of phenomenological carrier relaxations 25

3.2 Carrier Rate Equations (CRE) 27

3.2.1 Adiabatic approximation (CRE I) 27

3.2.2 Semi-adiabatic approximation (CRE II) 28

3.3 Impulse Response 29

3.4 Small-signal Harmonic Analysis 34

4 Modeling of QD SOAs 45

4.1 Device Structure 46

4.2 Modeling of Carrier Dynamics of QDs 48

4.2.1 Electron dynamics of QDs 48

4.2.2 Hole dynamics in QDs 51

4.2.3 Stimulated emission/absorption 52

4.2.4 Propagation effect 54

4.3 Numerical Implementation 54

5 Basic Properties of QD SOAs **57**

5.1 Linear Gain and Linewidth Enhancement Factor 57

5.2 CW Gain Saturation 65

5.3 Small-Signal Harmonic Medium Responses 71

5.3.1 Oscillations of carrier populations at a low modulation frequency 72

5.3.2 Oscillations of carrier populations over a broad modulation frequency range 73

5.3.3 Oscillations of gain at a low modulation frequency 82

5.3.4 Oscillations of gain over a broad modulation frequency range 86

5.3.5 Summary 89

6 Coherent Population Oscillations in Semiconductor Optical Waveguide **91**

6.1 Introduction of Optical Filtering Schemes 91

6.2 Modeling of Microwave Phase shifter 93

6.2.1 Microwave modulated optical signal 93

6.2.2 Frequency domain modeling of SOA and semi-analytical solution 94

6.2.3 Photodetection and optical filtering 96

6.3 Phase Shifting Results 99

6.3.1 Comparison to experimental results 99

6.3.2 Parameter dependence 100

6.4 Perturbation Analysis and Discussion 104

6.4.1 Perturbation without spatial variation 105

6.4.2 Perturbation including propagation effects 106

6.5 Summary 110

7 Microwave Phase Shifting based on QD SOAs **111**

7.1 Coherent Population Oscillations Effects 112

7.2 Cross Gain Modulation Effects 116

8 Optical Pulse Regeneration in QD Devices **123**
8.1 Amplification of Pulsed Signals 124
8.2 Regeneration of Pulsed Signals 126
8.3 Summary 129

9 Conclusions **131**

A Propagation Effects in Semiconductor Waveguide **135**

B Derivations of Small-Signal Harmonic Analysis **141**
B.1 General Formulism in a Two-level System 141
B.2 First-order Derivations in QDs 143

C Continuous Band Approximation for QD Electronic Structures **147**

D Analytical Derivation of Three Wave Mixing in SOA **151**

E Simulation Parameters **155**

F List of PhD Publications **157**

Bibliography **161**

Chapter 1

Introduction

In the recent decade, research in a wide range of optical signal processing technologies have gone through a significant growth for potential industrial applications. For applications in modern communication and computing systems, one of the important driving forces is the rapid advance in speed. In fiber-optic network, the bit rate of a single channel optical link is migrating from 10 Gb/s to 40 Gb/s or even higher. Limited available bandwidth is also pushing wireless communication systems into the millimeter (mm) wave region of 30-100 gigahertz. Although great advances in high-speed electronic devices operating at frequencies greater than tens of gigahertz [1] have been able to cover most of the current high-speed demand (large number of slower electronics that operate in parallel), the high-speed electrical signal processing at higher operation frequency is suffering more and more risk of circuit performance degradation with huge device cost and power dissipation [2]. It is natural to migrate at least some of the bandwidth demanding signal processing functions from the electrical domain to the optical domain [3], where the restrain on bandwidth is greatly released. In the field of fiber-optic telecommunication, it has received great attention to build up optical packet switched telecommunication networks. The key issues are to reduce optical-electrical-optical conversion and replace the corresponding intermediate electrical signal processing functions realized by large electronic packet routers. One of the important functions is the realization of all-optical signal regeneration (preferably at the bit rate much greater than 40 Gb/s), which is developed to remedy the optical signal degradation (typically due

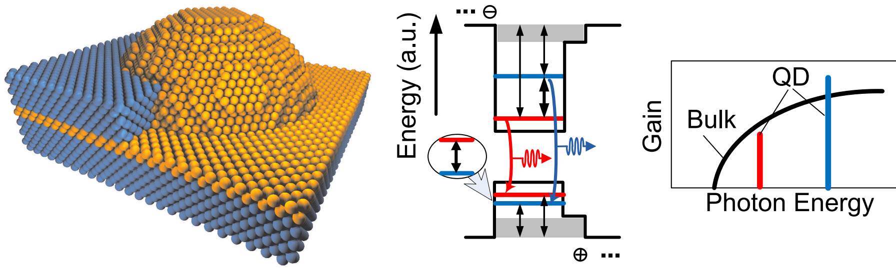

Figure 1.1: Quantum dots. (left) Schematic atomic view, (middle) electronic band diagram and (right) gain spectrum of a quantum dot.

to noise) within compact and inexpensive photonic devices instead of bulky opto-electronic regenerators. Another new area is microwave photonics [4, 5], which is a unification of microwave and photonic techniques for applications such as fibre delivery of millimeter waves (in-fibre radio) or using optical signal processing units to change the millimeter wave signals (optically-fed microwave phase shifter). These new ideas for implementation of optical signal processing not only rely on continuously exploring the limitations of commercially available photonic devices at higher operation frequencies, but also stimulate the demand for new materials as well as devices.

Among the important photonic material candidates, nano-structured semiconductor materials have been of increasing interests for decades in both physics studies and device fabrications like lasers or optical amplifiers. One of the most topical nano-structures is semiconductor quantum dots (QDs) [6, 7], which are very small three-dimensional systems with size ranging from nanometers to tens of nanometers as shown in Figure 1.1. Consisting of only a few hundred to a few hundred thousand atoms, QDs bridge the gap between solid state and single atoms and exhibit a mixture of solid-state and atomic properties. As a result of quantum confinement along all three dimensions, the energy states for carriers and corresponding photon transitions are composed of atomic-like discrete series instead of continuous bands for a bulk material. The three-dimensional freedom in engineering the quantum dot size makes such artificial nano-structure attractive for photonics applications. Different techniques have been used in fabrication of QD semiconductor materials with different compositions, which provide a large variety of corresponding electrical and

optical properties [8, 9]. For example, ultra-fast carrier dynamics in QD materials might make QD-based active semiconductor waveguide promising for various kinds of high-speed optical signal processing applications like linear amplification, signal regeneration and four-wave mixing (FWM) [10, 11].

Novel physical properties are expected to emerge and will give rise to new semiconductor devices as well as to drastically improved device performance. One of the novel phenomena is slow light effect enlightened by the classical experimental demonstration of slowing light to bicycle speeds in atomic gasses [12] and subsequently even completely stopping light. This also leads to a large category of investigations in physics and applications of the slow and fast light in semiconductor waveguide, in particular, coherent population oscillations (CPO) effect [13].

This thesis focuses on the implementation of a comprehensive device model for an active semiconductor waveguide incorporating quantum dots, typically functioning as a semiconductor optical amplifier (SOA). This model tackles some fundamental issues such as gain saturation, recovery and modulation response for quantum dot materials. Detailed numerical investigations have been used to demonstrate the potential of QD semiconductor waveguides for different optical signal processing functions.

The organization of the thesis is as follows: Chapter 2 presents some background knowledges of QD SOAs and the potential optical signal processing applications, in particular, the vision of optically fed microwave phase shifter based on slow and fast light effects and optical pulsed signal regeneration. Chapter 3 describes the basis to model light matter interaction in semiconductor. The aim is to clarify the assumptions and limitations of carrier rate equations. The QD SOAs model used in this work are given in Chapter 4.

The main results of the thesis are presented in chapter 5 to 8. Chapter 5 includes the basic properties of QD SOAs without propagation effects in terms of linear gain, linewidth enhancement factor, gain saturation and harmonic oscillation responses. Chapter 6 presents a theoretical investigation of coherent population oscillations (CPO) as well as microwave phase shifting based on a general wave-mixing model in SOA and an optical filtering scheme. The microwave phase shifting realized in QD SOAs based on CPO and cross gain modulation (XGM) effects are discussed in chapter 7. In chapter 8 the optical pulse regeneration capabilities in a simple QDs

waveguide device are predicted and discussed. Finally, conclusions of the work are provided in chapter 9.

Chapter 2

Background

In this chapter, we will briefly go through the background knowledge of the semiconductor quantum dots and devices. The visions of optical signal processing applications, that motivate the work in the thesis, are presented. One is related to the investigation of slow and fast light effects in semiconductor waveguides. Namely, the possibility of controlling the speed of light through a device may lead to applications in microwave photonics, in particular microwave phase shifting technique. Another is all-optical signal regeneration to remedy optical signal degradation within compact and inexpensive semiconductor devices.

2.1 Quantum Dot Semiconductor Optical Amplifiers (QD SOAs)

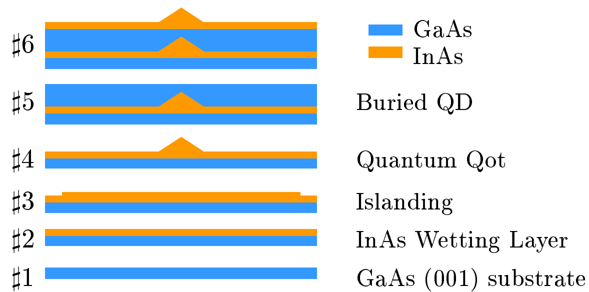

Figure 2.1: Schematic growth steps for self-assembled quantum dots.

Since the introduction of quantum dot with ideal three-dimensional confinement [6, 7], different fabrication methods have been used to realize realistic high quality dots [8, 9]. The quantum dots, that we focus on here, are self-assembled or self-organized dots shown in Figure 2.1. Such islands are realized by Stranski-Krastanow (SK) growth [14] on a semiconductor substrate. For example, growing InAs on a GaAs substrate layer by layer, a thin strained layer is formed due to the lattice mismatch. Under the right growth conditions (temperature, growth rate and etc.) and a critical thickness of epitaxial InAs layer, the accumulated strain in the deposited layers leads to sign reversal in chemical potential and thus switch growth mechenism [15]. Islands, three-dimensional quantum dots, start to form on top of a thin wetting layer (WL) with a few-monolayer thickness. These islands can be completely embedded with the material of the same kind as the substrate and be easily repeated to stack more layers of QDs.

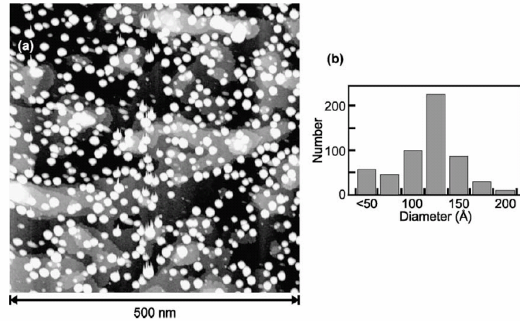

Figure 2.2: STM image of InAs QDs on GaAs (001). The number density of the QDs is 1.9×10^{11} *cm*$^{-2}$*. Histogram of QD size from the STM image [16].*

Due to the nature of self-assembling, size of quantum dots is inhomogeneously distributed. Figure 2.2 shows a scanning tunneling Microscope (STM) image of InAs QDs on GaAs. Normally a large number of quantum dots are randomly located on the wetting layer, see the histogram size distribution of QDs in Figure 2.2(b) as an example [16]. The crystal orientation of substrate, material composition, fabrication process, etc., have different impact on the shape. The unexpected size fluctuation degrades the overall uniformity feature of QDs. On the other hand, the controllable inhomogeneous distribution gives freedom for different device applications.

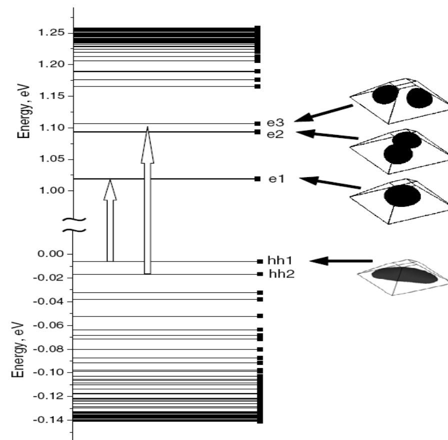

Figure 2.3: Calculated electron energy spectrum and the probability density iso-surfaces for the carriers in several states for InAs/GaAs quantum dot shape as a squared truncated pyramid. The vertical arrows mark the most strong interband optical transitions. The calculation is based on eight-band $\mathbf{k}\cdot\mathbf{p}$ *model [17].*

In general, a quantum dot is a three-dimensional potential system confining the carriers inside. An accurate determination of the electronic properties requires a detailed numerical calculation of eigenstates, which in turn requires knowledge of the precise shape, size, material composition and strains of the dot. Significant research effort has been devoted to the determination of such material parameters. Due to the nature of the self-assembled quantum dots, the measurement of geometry and composition have failed to provide details to a similar level of accuracy to which the electronic structure has been determined. As a result, the size of the dots were often used as adjustable parameters in models to fit experimental spectra. The accuracy and complexity of detailed models, such as multi-band $\mathbf{k}\cdot\mathbf{p}$ methods [18, 19], have been widely investigated and discussed. It is also found that the conventional $\mathbf{k}\cdot\mathbf{p}$ methods applied in the framework of applied specifically in the framework of the Luttinger-Kohn model [20] and the Kane model [21] sometimes can significantly misrepresent the fully converged results even when the shape, size and composition were given. In Williamson's work [22], a more complex model including atomistic interaction and many body effects is used. However, such calculations are very complex and time consuming, besides, they also depend on a number of parame-

ter values that are hardly known. Figure 2.3 shows an example of the calculated electronic energy spectrum based on eight-band $\mathbf{k} \cdot \mathbf{p}$ method [17]. Truncated pyramidal QDs with a particular size have been chosen in calculation to agree with the experimental data. The main interband optical transitions correspond to the two lowest QDs discrete states in the conduction and valence band. The upper states are forming a subband of continuum states. The probability density isosurfaces of wave functions provide a general idea of the three-dimensional confinement for the carriers in several discrete states.

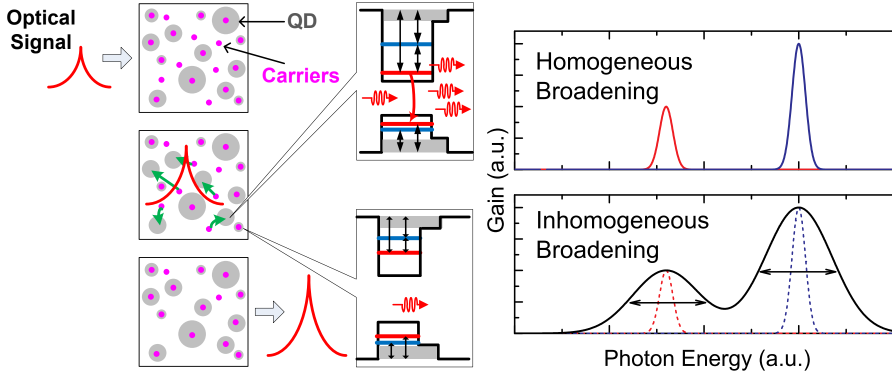

Figure 2.4: Illustration of optical amplification in en ensemble of quantum dots.

The scope of this thesis is focusing on the optical properties of an ensemble of QDs with their unique carrier dynamical processes rather than the fundamental electronic properties of an individual quantum dot. This leads to the investigation of the quantum dots as active medium, typically used in a semiconductor optical amplifier (SOA).

Figure 2.4 shows the general idea of optical amplification in an ensemble of QDs. When an optical signal is incident on an ensemble of QDs in full inversion. The optical signal will be amplified by stimulated emission in the QDs with interband transition energies (of discrete QD states) close to the photon energy. The carriers in the corresponding QD discrete states will be depleted and recovered by surrounding carriers through different carrier dynamical processes. Suggested mechanisms for the carrier relaxation include carrier-carrier scattering [23, 24, 25] and carrier-phonon scattering [26, 27, 28, 29]. Such interaction processes in QDs take place on timescales ranging from sub-picosecond to hundreds of picoseconds, which is

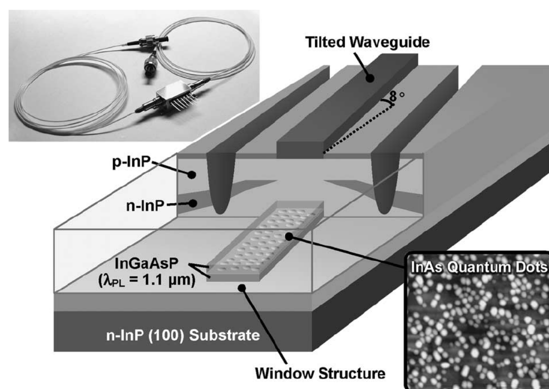

Figure 2.5: Structure of a quantum dot semiconductor optical amplifiers fabricated on an InP substrate. [10].

different from the conventional semiconductors.

Due to the different carrier masses and confinement energies of the conduction and valence band, electron and hole relaxation are expected to take place at different rates. The larger hole mass leads to a smaller mobility, resulting in a slow spatial transport. On the other hand, the larger hole mass also leads to a smaller energy spacing between hole states, resulting in a faster hole relaxation. Thus in most cases, the QDs dynamic properties are limited by the relatively *slow* electron dynamics [30, 31]. The corresponding scattering rates can be included in rate equation models that describe the carrier dynamics in quantum dot structures in terms of carrier densities or occupation probabilities. For highly uniformed QDs, the spectral gain has a narrow bandwidth with the appearance of homogeneous broadening. It is close to an ideal QD device with high material gain. On the other hand, the stimulated emission does not happen in all the QDs. In reality, the dispersion of dot size (inhomogeneous broadening) leads to the change of the interband transition energies for the discrete QD states. The spectral gain determined by the inhomogeneous broadening has a much broader bandwidth.

Figure 2.5 shows one of the reported high-performance QD SOAs [10]. Several layers of quantum dots with required emission wavelengths are embedded in a current-confined structure for a high current density. Anti-reflection designs including anti-reflective coating, tilted waveguide and window regions are often used

to suppress lasing action. Limited by the maximum density and inhomogeneous broadening of QDs, the waveguide is typically several millimeters long to realize a reasonable gain.

Such devices have been intensively studied due to their performance improvement over bulk or quantum-well SOAs in terms of ultrafast gain recovery [32, 33, 34, 35, 36, 37], high four-wave mixing efficiency [38, 39], high-speed operation at 40 Gb/s and beyond [10, 40], high saturation power and broad gain bandwidth [41]. Meanwhile, different versions of QD device theory [30, 31, 42, 43, 44, 45, 46, 47, 48] have been developed to bridge the gap between the measured device performance and the knowledge on QD carrier dynamics. The simulation helps to reveal the physical origins behind the benefits. The understanding of such properties also triggers the development of new semiconductor devices for different optical signal processing functionality.

2.2 Applications in Optical Signal Processing

2.2.1 Controlling the speed of light

The basic concept in controlling the speed of light is the control of group velocity. A continuous wave (CW) light beam propagating in a medium with refractive index n has a phase velocity $v = c/n$, where c is the velocity of light in vacuum. This corresponds to the speed at which a peak of the rapidly oscillating electrical field propagates through the medium. If the intensity of the signal varies in time, i.e. the spectrum of the signal has a finite width, the propagation speed of the intensity modulation is instead given by the group velocity v_g,

$$v_g = \frac{c}{n_g}, \qquad n_g = n + \frac{dn}{d\omega}\omega \tag{2.1}$$

where n_g denotes the group index and ω is the optical frequency. The group velocity thus differs from the phase velocity in media at frequencies, where the refractive index has a non-zero first-order derivative with frequency. In particular, the group index change arose from the material dispersion change, the latter term of Eq. (2.1) is of interest. Fig. 2.6(left) shows in dashed black lines the calculated imaginary and real parts of the complex susceptibility of a two-level medium, corresponding to the absorption and change in relative dielectric constant of the medium. As a general consequence of the Kramers-Kronig relations, the absorption resonance implies a finite frequency dependent contribution to the refractive index. It is seen that an absorption resonance leads to group refractive index which is smaller, at resonance, than the (phase) refractive index, thus corresponding to fast light. From Eq. (2.1) it is clear that in order to achieve a larger change in the group refractive index, the slope of the index with respect to frequency needs to be increased, which translates into the requirement of a sharper resonance with a smaller spectral width. This can be achieved by decreasing the dephasing time associated with the resonance, in many cases obtainable by e.g. lowering the temperature. However, since the maximum change in the group index occurs exactly at the absorption resonance, the increased change of the light speed comes at the prize of a larger absorption and may thus not be of any interest, since practically no light may be transmitted through the structure. Thus, a way of controlling the light speed, i.e. externally changing the group index, is needed.

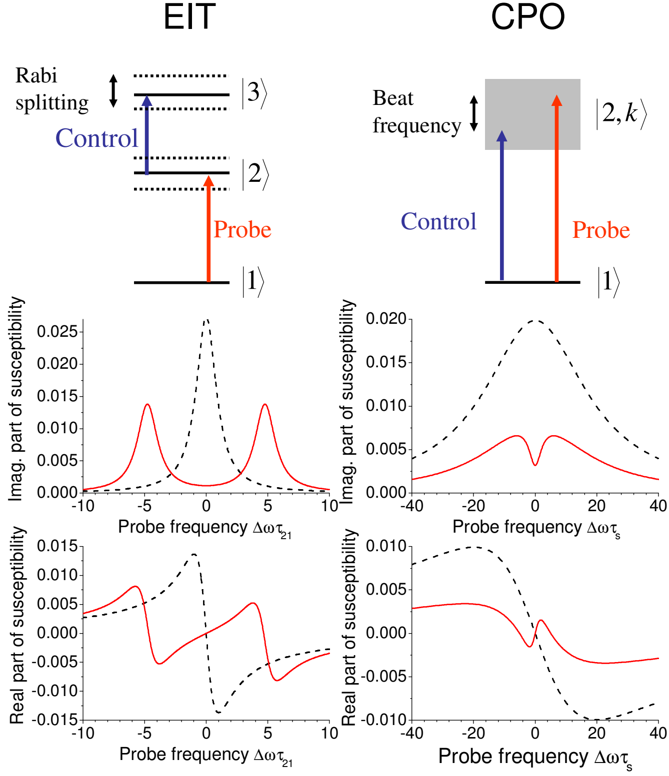

Figure 2.6: Level diagrams and typical examples of susceptibilities for electromagnetically induced transparency (EIT, left column) and coherent population oscillations (CPO, right column) versus detuning frequency. The level schemes (upper row) illustrate the choice of control and probe photon energies, $\hbar\omega_{co}$ and $\hbar\Omega_{pr}$, for the two schemes of excitation. Below, the imaginary and real parts of the susceptibilities are depicted, with dashed lines showing the susceptibilities for zero control signal. The probe frequency is normalized with respect to the 2-1 dephasing time for EIT and with respect to the carrier lifetime for CPO. [49]

The classical experimental demonstrations of slowing light to bicycle speeds in atomic gasses [12] and subsequently even completely stopping light have led to a significant interest in exploring the physics and applications of this phenomenon. Today, light slow-down has been demonstrated in a number of different physical media; in addition to atomic gasses, solid-state crystals [13], semiconductors [50, 51, 52], optical fibers [53, 54, 55], and photonic crystals [56, 57] have been used.

Also, a number of different physical effects have been explored to realize control of the propagation speed in the various media, i.e., electromagnetically induced transparency (EIT) [58], coherent population oscillations (CPO) [13] waveguide dispersion [56, 57], parametric effects, and others.

This progress of controlling the group velocity of an optical signal propagating in a solid state device has attracted increasing attention due to the possibilities of realizing compact devices for signal processing, such as all-optical buffering [59] and phase shifters for microwave photonics [60]. Semiconductor based devices, with their well-developed fabrication technology and the possibilities for integration with other functionalities, are important candidates for practical applications.

The phenomenon of electromagnetically induced transparency (EIT), used in the cold atoms experiments by Hau et al [12], offers a way to change the dispersion of refractive index without being limited by absorption. Semiconductor quantum dots (QD) seem a natural choice to pursue light-slow down in semiconductor media with their discrete electronic levels [61]. In Fig. 2.6(left) we have illustrated the case of a three-level configuration known as a ladder scheme. We consider a probe signal which is resonant, or nearly resonant, with the 1-2 transition. However, in this case we have an additional pump beam which is resonant with the 2-3 transition. When the intensity of the pump beam is increased, the levels 2 and 3 split up due to Rabi oscillations and the absorption line of the 1-2 transition is split in two. The absorption of the probe is seen to be strongly reduced, as seen in solid red curves in Fig. 2.6(left). The corresponding change of the dispersion of the refractive index implies a positive group index at the 1-2 transition frequency, simultaneously with the strongly reduced absorption. However, since EIT relies on a quantum mechanical coherence among levels and dephasing times in semiconductors are short and, at the same time, present-day technology leads to quantum dots with large size dispersion, there are significant challenges to overcome for realizing practical light-speed control in semiconductors based on EIT [61, 62].

Instead, the effect of coherent population oscillations (CPO) [13] may provide a realistic alternative in semiconductors. In this case the interference of a pump and probe signal exciting a continuum of transitions, see Fig. 2.6 (right), leads to coherent oscillations of the populations in the continuum at the pump-probe beat frequency. This, in turn, changes the refractive index dispersion seen by the probe

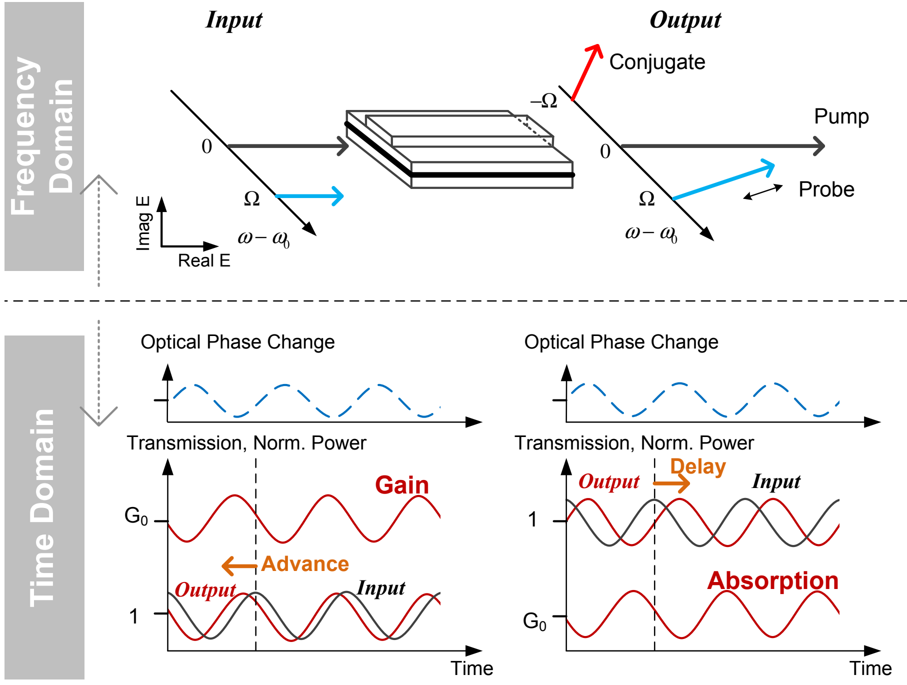

Figure 2.7: Illustration of coherent population oscillations (CPO) as wave mixing between a pump and a probe signal in a semiconductor waveguide, leading to the generation of a conjugate signal as well as the modification of the amplitude and phase of the probe. In the time domain, it corresponds to the modulation of gain/absorption as well as index (optical phase).

due to wave mixing effects. The corresponding real and imaginary parts of the susceptibility are shown in Fig. 2.6 (right). In contrast to EIT, CPO relies on the direct interference between pump and probe beams, which leads to oscillations of the populations at the beat frequency and subsequent modification of the effective absorption and index experienced by the probe signal. For the CPO effect the coherence is thus assured by the interference of the external laser beams at room temperature.

Figure 2.7 illustrates this effect in both time and frequency domain. When applying a signal that is intensity modulated in time, e.g. by the beating of two CW signals, a strong pump and a weaker probe, the rate of stimulated emission or

absorption is also modulated in time. This, in turn, implies a modulation of the excited carrier density of the structure. Since the gain or absorption of the structure and the refractive index depend on this carrier density, these quantities are modulated as well. It is also referred to as the temporal saturation effect of gain dynamics [63]. In frequency domain, the gain or absorption and index modulation correspond to temporal gratings that scatter the strong pump signal to sidebands displaced from the pump carrier frequency by the modulation frequency. One component is scattered to the mirror frequency and leads to the build-up of a so-called conjugate signal as is well-known from wave mixing in nonlinear optics in general and in semiconductor waveguides in particular, see [64]. Another component is scattered to the original probe frequency and leads to a change of both the intensity and phase of the probe field, depending on the phase relation between the original probe field and the scattered component. This effect is also referred to as the Bogatov effect [65]. From the point of view of light-speed control, referring back to Eq. (2.1), the desired effect of the wave mixing is to achieve a large and controllable dispersion of the refractive index.

The basic set-up for characterizing slow and fast light effects in photonic (semiconductor) devices based on a sinusoidally modulated input signal, also generally implemented as a microwave phase shifter, are shown in Figure 2.8. A laser beam is intensity modulated at a microwave frequency of Ω, passed through the device under test (optical signal processor) and sent into a network analyzer, which by comparison with the original signal extracts the microwave phase ϕ and the microwave amplitude. The change in group velocity is related to the phase via

$$\Delta n_g = \frac{c}{L}\Delta t = \frac{c}{L}\frac{\Delta\phi}{\Omega} \tag{2.2}$$

Here, Δt is the change in propagation time, L is the length of the device and $\Delta\phi$ is the change of the microwave phase relative to a fixed reference point, i.e., at a specific input power level and bias condition. The light speed or microwave phase shift can be controlled by changing the input optical power to the device, accomplished via a variable optical attenuator, or by changing the bias conditions for the device.

For several applications in microwave photonics, the achievement of a phase shifting of 360 degree is important in order to realize the full functionality. However, the experimental demonstration in a single element, including bulk, quantum well

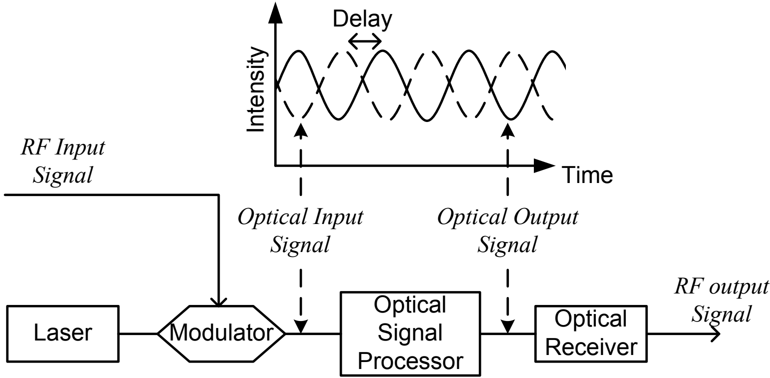

Figure 2.8: Schematic diagram of a microwave phase shifter based on optical signal processing.

(QW) or QD semiconductor optical amplifiers [51, 66, 67, 68], or an electro absorber (EA) [52], shows phase shift of a few tens of degrees. The maximum phase shift and bandwidth will be limited by different effects [59]. In both SOAs and EAs the slow carrier density pulsation process sets an important limit [52, 66]. For absorbing media the residual loss further limits the achievable delay [66]. The amplified spontaneous emission (ASE) limits the available SOA gain, and hence the phase change, in long amplifiers [69].

A number of proposals have been investigated to increase the phase shift. One idea is to switch between the regimes of gain and absorption leading to a phase shift larger than 180 degrees [70]. However, the results are limited by the operation frequency of SOA (around 1 GHz) and large changes in net transmissions. Another idea is to cascade the single elements together, i.e. the concatenation of alternating gain and absorber sections, to achieve a larger phase shift tuning range as compared to a single element. A monolithic four section device (2 SOA-EA pair) has been reported to realize a large phase shift 110 degrees at 5 GHz [71, 72]. Such devices can be further designed to provide net zero gain and 360 degree phase shifts with more cascades. Still, the overall phase shift and bandwidth are inherently limited in the single element stage.

One of our proposals is to use optical filtering to explore the refractive index dynamics indicated in Figure 2.7 and further enhance the phase shifting [73, 74].

Details will be discussed in Chapter 6. For the QD SOAs, we theoretically investigate the gain dynamics in QD SOAs and suggest two types of microwave phase shifters. Details will be discussed in Chapter 7. All of our proposals are aiming at providing promising methods for increasing the achievable phase change and bandwidth.

2.2.2 Optical signal regeneration

In fiber-optic communication system, semiconductor optical amplifier attracts the attention mostly for linear inline amplification [75] and fast nonlinear all-optical signal processing [76], e.g., regeneration, wavelength conversion and switching. On developing optical regenerators, much effort has been spent to fulfill the requirements of long-haul systems as well as networks with flexibility and scalability. As the bit rate of a single channel optical link is migrating from 10 Gb/s to 40 Gb/s or even higher, it is becoming more challenging to realize a high-speed optical regenerator that has a simple structure. Many optical regenerators based on SOAs have been proposed [77, 78, 79, 80, 81, 82].

One of them is the simple pass-through semiconductor device with regeneration properties [81, 82, 83] illustrated in Figure 2.9. As the optical signals pass through a semiconductor optical amplifier (SOA), the output signal is partially restored. Both the signals and the background noise are amplified. However, due to gain saturation, output power of signals reaches a constant flat level above a certain limit of input power, referred to as limiting amplification. When the optical signals are passing through an electro absorber (EA), the noise is attenuated while the optical signals are less affected due to saturable absorption. It is possible to have an S-shaped input-output relation (or a "bandpass"-like transfer function) by a combination of saturable gain and absorption. This can be used as 2R-regeneration (re-amplification and reshaping). Such a 2R-regenerator acts like an optical decision circuit, which separates the signal and noise levels (increases of extinction ratio) and reduces the intensity fluctuations. In practice, monolithic components with SOA-EA pairs have been realized using bulk [84] and QW semiconductor materials [85]. So far, experimentally the 2R regeneration based on such devices only reaches the operation at 10 Gb/s [86]. In comparison, the other schemes, i.e. using cross phase modulation (XPM) and elaborate interferometer setup [77, 78, 79, 80], have superior

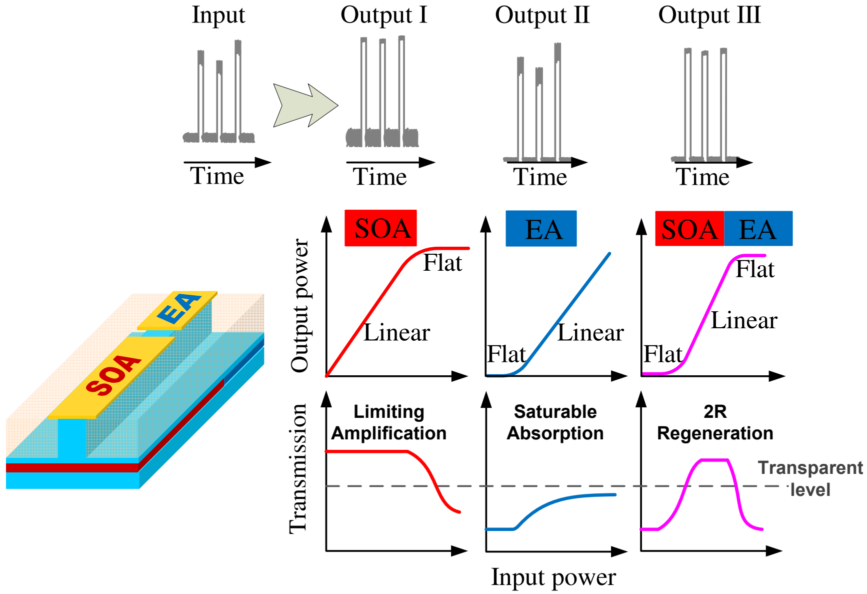

Figure 2.9: Schematic optical signal regeneration based on active semiconductor devices. SOA: semiconductor optical amplifier. EA: Electro-absorber.

performances >40 Gb/s even based on the conventional SOA.

Here, one of the limiting issues for the bulk or QW SOAs is the patterning effects as shown in Figure 2.10. Namely, the amplification of signals, especially in the gain saturation regime, depends on the input data pattern. This effect is due to the carrier depletion during the change of the signal power levels. The slow full gain recovery time (around a few hundreds of picoseconds) limits the maximum operation speed. It is of practical interest to investigate the patterning effects regarding the operation limit. In the performance evaluation of devices, a pseudo random binary sequence (PRBS) is favored to approximate the real data pattern in the transmission system [75]. In general, a long sequence length, typically $2^{31}-1$, is necessary to obtain satisfactory statistics. But a long PRBS is often prohibited in experiments by the temporal multiplexing techniques to generate the signal and needs excessive computation times in simulations. On the contrary, the use of a short PRBS length, e.g. $2^{7}-1$, is also not giving a full measure of the problem, especially at increasingly high bit rates [87].

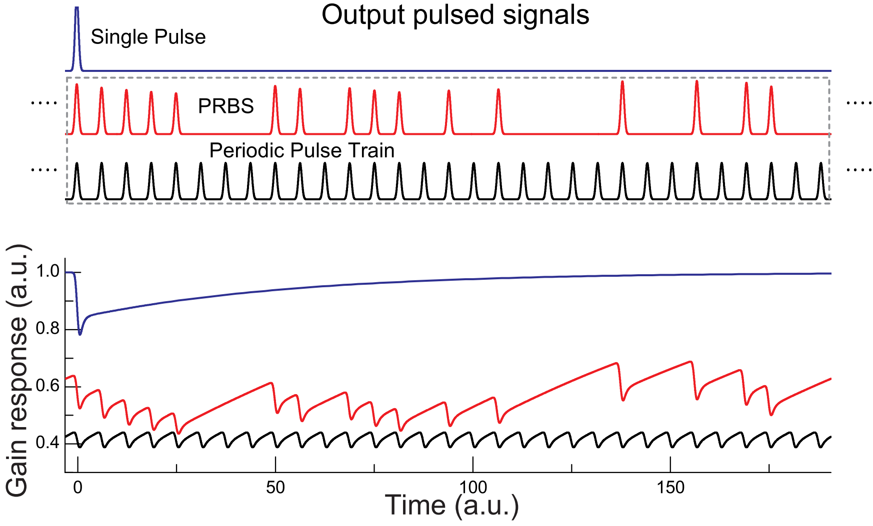

Figure 2.10: Illustration of patterning effects in semiconductor optical amplifiers. Identical input pulsed signals with different data patterns are incident into the devices. PRBS: pseudo random binary sequence.

Instead, another systematic approach using periodic pulse trains has been proposed to predict patterning-effect-free QD SOAs [88]. Such periodic method is equivalent to consistently investigate gain response of SOA to the most heavily-loaded data streams with various time spacing. From this point of view, patterning effects in the amplification of a random data stream are the transients at the output of the SOAs, when switching among periodic pulse trains with repetition frequencies from zero to B_0 incident into the device. If the steady gain for the periodic pulse train at a repetition frequency up to B_0 has a negligible deviation from a single pulse, the patterning effects for the random data stream at the corresponding bit rate are expected to be small.

One of our intentions is to theoretically investigate the simple pass-through QD devices with regeneration properties for high bit rates based on the periodic method. Details will be discussed in Chapter 8.

Chapter 3

Fundamentals of Light Matter Interaction in Semiconductors

In semiconductor optical devices, the laser field and the semiconductor gain medium are coupled by the gain and the refractive index, or equivalently by the induced complex susceptibility. This chapter describes the fundamental elements that we have used to model the dynamics of carriers and induced complex susceptibility to applied electromagnetic fields (laser field) in a semiconductor medium.

There are several different model equations to quantify the physics of gain medium and describe the dynamics of stimulated emission and absorption. The optical Bloch equations, which are a set of coupled time differential equations for population inversion and the induced electric polarization, form the basis of the semiclassical two-level model [89, 90, 91]. A semiconductor medium can be interpreted as the sum of two-level systems with different transition frequencies as determined by the electronic band structure and with separated carrier inversions. Hereby, the induced susceptibility is a superposition of contributions of the various transitions. A more microscopic approach by semiconductor Bloch equations [90, 91] can include Many-body Coulomb effects, where a separate treatment of screened Hartree-Fock approximation and collisional effects is often used [92]. Supplemented with appropriated treatment of the scattering processes, semiconductor

Bloch equations have been used as a theoretical framework for various optical properties of semiconductors and semiconductor microstructures [91].

In parallel, a simplified framework as semiclassical density matrix equations [93, 94, 64, 95] has been derived from the semiconductor Bloch equations. By neglecting the many-body effects and treating the carrier scattering with phenomenological relaxation rates, the numerical demands have been significantly reduced.

In this chapter, we will start with the basics of semiclassical density matrix equations for the classical two-level systems. Regardless of the superposition for a semiconductor medium, two rate equation approximations that eliminate the differential equations for polarizations will be discussed. The different sets of equations will be compared by analysis of impulse response. A general approach will be formulated for the corresponding small-signal harmonic analysis. A brief description of the modeling of propagation effects in semiconductor waveguide is included in Appendix A.

3.1 Semiclassical Density Matrix Equations (DME)

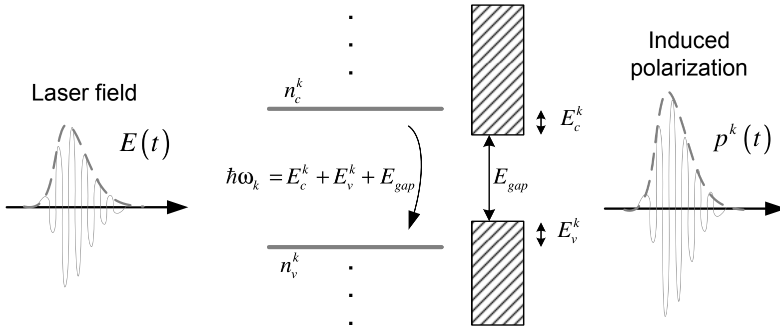

Figure 3.1: Illustration of Light-matter interaction in the classical two-level system for a semiconductor medium.

This section is based on the basics of density matrix equations presented in [90, 91, 95].

The light-mater interaction in the classical two-level system, with upper and lower levels referring to the conduction and the valence band for a semiconductor

medium are illustrated in Figure 3.1. E_{gap} denotes the bandgap energy of semiconductor medium. E_c^k and E_v^k denote the energy levels in the conduction (c) and valence (v) band for state k respectively. The corresponding interband transition energy is $\hbar\omega_k = E_c^k + E_v^k + E_{gap}$. $n_c^k(t)$ and $n_v^k(t)$ denote the corresponding time-variant electron and hole occupation probabilities. t is the time coordinate. For the applied electric field $E(t)$:

$$E(t) = A(t)\exp(-i\omega_0 t) + c.c. \tag{3.1}$$

Here $A(t)$ is the corresponding slow varying complex envelope with the carrier frequency ω_0.[1] The material response is defined as the induced interband dielectric polarization (atomic dielectric polarization) $p^k(t)$:

$$p^k(t) = p_{cv}^k(t)\exp(-i\omega_0 t) \tag{3.2}$$

Here $p_{cv}^k(t)$ is the corresponding slowly varying complex envelope with the carrier frequency ω_0.

The corresponding Bloch equations are given by [90, 91] as following:

$$\partial_t n_c^k(t) = \partial_t n_c^k(t)\Big|_{rel} - \frac{i}{\hbar}\left[d_k^* p^k(t) - d_k p^{k^*}(t)\right] E(t) \tag{3.3}$$

$$\partial_t n_v^k(t) = \partial_t n_v^k(t)\Big|_{rel} - \frac{i}{\hbar}\left[d_k^* p^k(t) - d_k p^{k^*}(t)\right] E(t) \tag{3.4}$$

$$\partial_t p^k(t) = \left[-i\omega_k - \gamma_2^k\right] p^k(t) - \frac{id_k}{\hbar}\left[n_c^k(t) + n_v^k(t) - 1\right] E(t) \tag{3.5}$$

where d_k is the dipole moment of the transition for state k. ∂_t denotes the time derivative operator. The first terms on the right hand side (RHS) of Eq. (3.3) and (3.4) denotes the carrier relaxation/scattering processes. When a phenomenological model is applied for the relaxation, the Bloch equations can be simplified as **density matrix equations** [95]. The second terms on the RHS of Eq. (3.3) and (3.4) denote the occupation probability change induced by stimulated emission/absorption. Eq. (3.5) describes the damped oscillation properties of atomic dielectric polarization. γ_2^k is the corresponding dephasing rate for the dielectric polarization that

[1] An unambiguous definition of the envelope from [96] has the form $A(t)\exp(-i\omega_0 t + i\Psi)$. where $\omega_0 = \int_0^\infty \omega|\tilde{E}(\omega)|^2 d\omega / \int_0^\infty |\tilde{E}(\omega)|^2 d\omega$, $\tilde{E}(\omega)$ is the Fourier transform of $E(t)$ and ψ is defined such that the imaginary part of the complex envelope A(t) is zero at t=0. The envelope $A(t)$ is assumed to remain invariant under a change of ψ.

describes the nonresonant part. The frequency detuning between atomic dielectric polarization and electric field contributes to the resonant part.

The corresponding macroscopic dielectric polarization density $\mathbf{P}(t)$ as the sum over the momentum vector $\mathbf{k}$ is:

$$\mathbf{P}(t) = \frac{1}{V}\sum_{\mathbf{k}}\left(d_k^* p^k + d_k {p^k}^*\right) \tag{3.6}$$

where V is the active region volume.

With the assumption of overall charge neutrality, the corresponding superposition form of total carrier density is:

$$\mathbf{N}(t) = \frac{1}{V}\sum_{k} n_\alpha^k(t) \quad (\alpha = c, v) \tag{3.7}$$

By substituting Eq. (3.1) and (3.2) into density matrix equations, we obtain the set of equations for the envelope:

$$\partial_t n_\alpha^k(t) = \partial_t n_\alpha^k(t)\Big|_{rel} - R_{stim}^k(t) \quad (\alpha = c, v) \tag{3.8}$$

$$\partial_t p_{cv}^k(t) = \left[-i(\omega_k - \omega_0) - \gamma_2^k\right] p_{cv}^k(t) - \frac{id_k}{\hbar}\left[n_c^k(t) + n_v^k(t) - 1\right] A(t) \tag{3.9}$$

where $R_{stim}^k(t)$ is the generation (occupation probability change) rate of electron-hole pairs induced by the stimulated emission/absorption, which can be expressed as:

$$\begin{aligned} R_{stim}^k(t) &= \frac{i}{\hbar}\left[d_k^* p_{cv}^k(t) A^*(t) - d_k {p_{cv}^k}^*(t) A(t)\right] \\ &= 2\mathbf{Im}\left\{\frac{d_k}{\hbar} {p_{cv}^k}^*(t) A(t)\right\} \end{aligned} \tag{3.10}$$

By defining the Fourier transform pair for the envelopes as:

$$\tilde{y}(\Omega) = \int_{-\infty}^{\infty} y(t) e^{i\Omega t} dt \tag{3.11}$$

$$y(t) = \frac{1}{2\pi}\int_{-\infty}^{\infty} \tilde{y}(\Omega) e^{-i\Omega t} d\Omega \tag{3.12}$$

We can further integrate Eq. (3.9) to find a temporal solution for $p_{cv}^k(t)$ as:

$$p_{cv}^k(t) = -\frac{d_k}{\hbar}\int_{-\infty}^{t} dt' e^{-\left[i(\omega_k - \omega_0) + \gamma_2^k\right](t - t')}\left[n_c^k(t') + n_v^k(t') - 1\right] A(t') \tag{3.13}$$

or equivalently using Fourier transform to get a spectral solution for $\tilde{p}^k_{cv}(\Omega)$ as:

$$\tilde{p}^k_{cv}(\Omega) = \frac{d_k}{\hbar} L_k(\omega_0 + \Omega) \left\{ \left[\tilde{n}^k_c(\Omega) + \tilde{n}^k_v(\Omega) \right] \otimes \tilde{A}(\Omega) - \tilde{A}(\Omega) \right\} \tag{3.14}$$

where

$$L_k(\omega) = \frac{1}{\omega - \omega_k + i\gamma^k_2}$$

is the Lorentzian factor. $\otimes$ denotes the convolution operator.

The appearance of the time integral on the RHS of Eq. (3.13) shows that the polarization depends on the values of occupation probabilities and electric field at earlier times $t' \leq t$. Thus the generation rate determined by Eq. (3.10) is a process with such a memory structure, as so called non-Markovian process [91].

3.1.1 Descriptions of phenomenological carrier relaxations

Here we will briefly discuss two types of phenomenological carrier relaxation models with their own physics perspectives.

A simple phenomenological description of the carrier relaxation process is based on the exponential relaxation model. A non-equilibrium distribution n^k_α, for instance, generated by an optical pulse, are driven by collision towards a quasi-equilibrium Fermi-Dirac distribution $n^{k,eq}_\alpha$ with one relaxation time τ_α, $(\alpha = c, v)$:

$$\begin{aligned} \partial_t n^k_\alpha(t) \Big|_{rel} &= -\frac{n^k_\alpha(t) - n^{k,eq}_\alpha}{\tau_\alpha} \\ &= -\gamma^k_\alpha \left[n^k_\alpha(t) - n^{k,eq}_\alpha \right] \quad (\alpha = c, v) \end{aligned} \tag{3.15}$$

here γ^k_c and γ^k_v are the corresponding phenomenological relaxation rates for equilibrium of state k in the conduction and valence band. Solving Eq. (3.8) and (3.9) with relaxation contributions given by Eq. (3.15) requires knowing the Fermi-Dirac distributions at each time step. For a continuum of states, the overall quasi-equilibrium Fermi-Dirac distribution is determined by assuming total carrier conservation in carrier-carrier collisions:

$$\sum_k n^{k,eq}_\alpha = \sum_k n^k_\alpha(t) \tag{3.16}$$

where the quasi-equilibrium Fermi-Dirac distribution description can be further defined as a local equilibrium $n^{k,eq}_\alpha(t)$, which depends on a slowly varying quasi-

fermi energy $E_{f,\alpha}(t)$, temperature T and the corresponding energy level E_α^k:

$$n_\alpha^{k,eq}(t) = \frac{1}{1 + \exp\left(\frac{E_\alpha^k - E_{f,\alpha}(t)}{k_B T}\right)} \tag{3.17}$$

Here k_B is the Boltzmann constant.

Another phenomenological description of carrier relaxation process is based on a balanced scattering model determined by Fermi's golden rule [30, 97]. It is similar to the simplest version of the quantum Boltzmann integral for carrier-carrier collisions [91, 92]. Such model treats the carrier relaxation as one pair of non-equilibrium capture and escape transitions, with a pair of capture and escape time (τ_{cap} and τ_{esc}), between a lower state k and a upper state k':

$$\partial_t n_\alpha^k(t)\Bigg|_{rel} = \frac{n_\alpha^{k'}(t)[1 - n_\alpha^k(t)]}{\tau_{cap}} - \frac{n_\alpha^k(t)[1 - n_\alpha^{k'}(t)]}{\tau_{esc}}, \quad (\alpha = c, v) \tag{3.18}$$

As the non-equilibrium occupation probability approaches thermal equilibrium status, we have:

$$\frac{n_\alpha^{k'}(t)[1 - n_\alpha^k(t)]}{\tau_{cap}} = \frac{n_\alpha^k(t)[1 - n_\alpha^{k'}(t)]}{\tau_{esc}} \tag{3.19}$$

By substituting Boltzmann distribution for the occupation probabilities, which is an approximation of Fermi-Dirac distribution in the limit of non-degenerate statistics, we have the ratio between the escape and capture time under the condition of *detailed balance*:

$$\frac{\tau_{esc}}{\tau_{cap}} = \exp\left(\frac{E_\alpha^{k'} - E_\alpha^k}{k_B T}\right) \tag{3.20}$$

where $E_\alpha^{k'} - E_\alpha^k$ is the energy level difference between the corresponding upper and lower state.

The phenomenological treatments for the non-equilibrium carrier relaxation here are based on Markov approximations. Both of the exponential relaxation and balanced scattering models, depend only on the occupation probabilities at time t and not the values at earlier times. It is important to realize that even when the non-equilibrium occupation probabilities are sufficiently close to the equilibrium status, the balance condition in the balanced scattering model does not imply the absence of scattering events in contrast to the exponential relaxation model. The individual terms in Eq. (3.18) are nonzero and rather large.

3.2 Carrier Rate Equations (CRE)

Very often, the semiclassical density matrix equations are further simplified to the carrier rate equations by eliminating the differential equations for atomic polarizations with different slowly-varying approximations . While all the slowly-varying approximations will provide static solutions identical to those of the density matrix equations, the dynamic responses will vary from each other.

3.2.1 Adiabatic approximation (CRE I)

Assuming the spectral width of the electric field to be much small than γ_2^k as well as $|\omega_0 - \omega_k| << \gamma_2^k$, the polarization follows both the field and occupation probability changes adiabatically. By eliminating the time differential term in Eq. (3.9), we obtain the approximated polarization $\bar{p}_{cv}^k(t)$:

$$\begin{aligned} \bar{p}_{cv}^k(t) &= \frac{\omega_0 - \omega_k - i\gamma_2^k}{(\omega_0 - \omega_k)^2 + (\gamma_2^k)^2} \frac{d_k}{\hbar} \left[n_c^k(t) + n_v^k(t) - 1\right] A(t) \\ &= L_k(\omega_0) \frac{d_k}{\hbar} \left[n_c^k(t) + n_v^k(t) - 1\right] A(t) \end{aligned} \tag{3.21}$$

which is equivalent to set the lorentzian factor in Eq.(3.14) as a constant $L_k(\omega_0)$ for the carrier frequency and then transfer back to time domain.

Thus we have the adiabatic carrier density equations in the form:

$$\partial_t n_\alpha^k(t) = \left.\partial_t n_\alpha^k(t)\right|_{rel} - \bar{R}_{stim}^k(t) \quad (\alpha = c, v) \tag{3.22}$$

where the corresponding generation rate $\bar{R}_{stim}^k(t)$ is:

$$\begin{aligned} \bar{R}_{stim}^k(t) &= i\frac{|d_k|^2}{\hbar^2} \left[L_k(\omega_0) - L_k^*(\omega_0)\right] \left[n_c^k(t) + n_v^k(t) - 1\right] |A(t)|^2 \\ &= 2\frac{|d_k|^2}{\hbar^2} \mathbf{Im}\left\{L_k^*(\omega_0)\right\} \left[n_c^k(t) + n_v^k(t) - 1\right] |A(t)|^2 \end{aligned} \tag{3.23}$$

where

$$\mathbf{Im}\left\{L_k^*(\omega_0)\right\} = \frac{\gamma_2^k}{(\omega_0 - \omega_k)^2 + (\gamma_2^k)^2}$$

In this way, the generation rate is linearly proportional to the product of occupation probabilities and the optical power ($\propto |A(t)|^2$) at time t. Such process has no memory dependence on the values at earlier times. This approximation is

a popular version in semiconductor laser physics [90, 98], especially regarding CW performance or modulation response with modulation frequency much smaller than γ_2^k .

3.2.2 Semi-adiabatic approximation (CRE II)

Alternatively, assuming the difference between optical carrier and optical transition to be comparable to the dephasing rate $|\omega_0 - \omega_k| \sim \gamma_2$, the polarization only follows the occupation probability changes adiabatically [42]. The polarization $\hat{p}_{cv}^k(t)$ can be approximated by extracting the occupation probability terms out of the temporal integral on the RHS of Eq. (3.13) as:

$$\hat{p}_{cv}^k(t) = -\frac{d_k}{\hbar}\left[n_c^k(t) + n_v^k(t) - 1\right]\int_{-\infty}^{t} dt' e^{-\left[i(\omega_k-\omega_0)+\gamma_2^k\right](t-t')} A(t') \tag{3.24}$$

which is equivalent to keeping the multiplication of the Lorentzian function and spectral electric field together for the spectral convolution with occupation probabilities in Eq. (3.14).

Thus we have the semi-adiabatic carrier density equations in the form:

$$\partial_t n_\alpha^k(t) = \partial_t n_\alpha^k(t)\Big|_{rel} - \hat{R}_{stim}^k(t) \quad (\alpha = c, v) \tag{3.25}$$

where the corresponding generation rate $\hat{R}_{stim}^k(t)$ is:

$$\begin{aligned}
\hat{R}_{stim}^k(t) &= i\frac{|d_k|^2}{\hbar^2}\left[n_c^k(t) + n_v^k(t) - 1\right] \\
&\quad \times\left\{\left[\int_{-\infty}^{t} dt' e^{-\left[i(\omega_0-\omega_k)+\gamma_2^k\right](t-t')} A^*(t')\right] A(t)\right. \\
&\quad \left. - \left[\int_{-\infty}^{t} dt' e^{-\left[i(\omega_k-\omega_0)+\gamma_2^k\right](t-t')} A(t')\right] A^*(t)\right\} \\
&= 2\frac{|d_k|^2}{\hbar^2}\left[n_c^k(t) + n_v^k(t) - 1\right] \\
&\quad \times\mathbf{Im}\left\{-\left[\int_{-\infty}^{t} dt' e^{-\left[i(\omega_0-\omega_k)+\gamma_2^k\right](t-t')} A^*(t')\right] A(t)\right\}
\end{aligned} \tag{3.26}$$

Although this approximation is still not strictly equivalent to the exact convolution in the presence of time-varying occupation probabilities, it still provides us with a different perspective about the memory effect of light-matter interactions. In this way, the generation rate is on longer linearly proportional to the optical power ($\propto |A(t)|^2$) at time t.

3.3 Impulse Response

In this section, we will briefly discuss and illustrate how the different treatments of stimulated emission described in the previous sections in a simple two-level system influence the corresponding impulse response.

For simplicity, we use a simple exponential relaxation expression:

$$\partial_t n_\alpha^k(t)\bigg|_{rel} = -\gamma_\alpha^k \left[n_\alpha^k(t) - n_\alpha^{k,eq}\right] \quad (\alpha = c, v) \tag{3.27}$$

where γ_α^k and $n_\alpha^{k,eq}$ are the corresponding relaxation rates and final equilibrium occupation probabilities, which satisfy:

$$\gamma_c^k = \gamma_v^k, \quad n_c^{k,eq} = n_v^{k,eq}, \quad n_c^k(t) \equiv n_v^k(t)$$

Assuming an input unchirped Gaussian shape electric field as:

$$A(t) = \frac{\hbar\gamma_2^k}{2d_k} \cdot A_0 \exp\left(-\frac{1+iC}{2}\frac{t^2}{T_0^2}\right)$$

where A_0 is the normalized amplitude, T_0 is the half-width of $1/e$ intensity, $C = 0$ indicates no frequency chirp of pulse. d_k is assumed to be a real value. For zero frequency detuning between optical carrier and interband transition, $\omega_0 - \omega_k = 0$, the slowly varying envelope of the atomic polarization only has the non-zero imaginary part.

Figure 3.2 shows the calculated impulse responses from the corresponding density matrix equations Eq. (3.8) and (3.9). We first define a "short" pulse with pulse width comparable to the inverse of dephasing rate ($T_0 = \frac{2}{\gamma_2^k}$). As shown in Figure 3.2(a), the occupation probability is rapidly depleted to the transparency point $2n_\alpha^k = 1$ by increasing the input pulse amplitude and slowly recovers back to the equilibrium value $n_\alpha^{k,eq} = 1$. As the amplitude of pulse becomes strong enough, the occupation probability shows several cycles of damped oscillations around the transparency point. The atomic polarization as well as generation rate induced by stimulated emission/absorption shows that the corresponding oscillation is damped out on the scale of the inverse of dephasing rate and comparable to the whole pulse period. The damped oscillations reflect the properties of the non-Markovian light-matter interactions. In contrast, for a "long" pulse ($T_0 = \frac{10}{\gamma_2^k}$), such transient

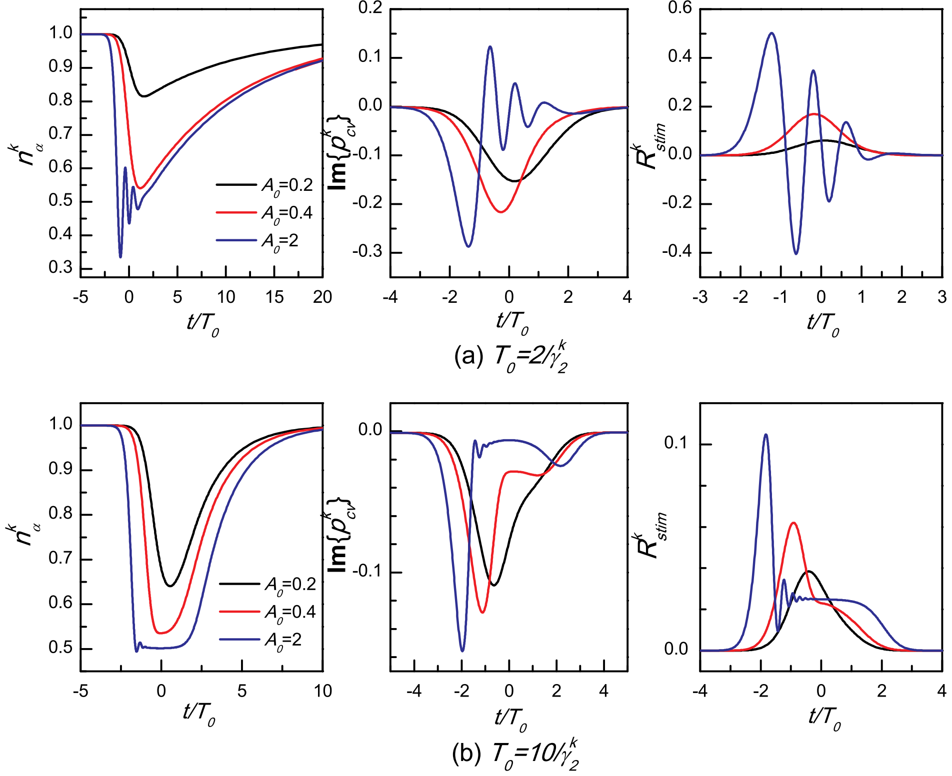

Figure 3.2: Impulse responses calculated from density matrix equations for a single unchirped Gaussian pulse. Results include (left) occupation probabilities n^k_α, (middle) imaginary part of atomic polarization envelope $\mathbf{Im}\{p^k_{cv}\}$ *and (right) stimulated emission R^k_{stim}. Gaussian pulses have different pulse amplitudes A_0 and pulse widths: (a) $T_0 = \frac{2}{\gamma^k_2}$ (b) $T_0 = \frac{10}{\gamma^k_2}$. The other relevant parameters are: $\gamma^k_2 = 1$, $\gamma^k_\alpha = 0.05$, $n^{eq,k}_\alpha = 1$ and $\omega_0 - \omega_k = 0$.*

damped oscillation starts within a small fraction of the leading edge of the pulse. As the pulse becomes much longer than the inverse of the dephasing rate, the oscillation becomes less significant.

We keep the same parameters for the carrier rate equations with two different slowly-varying envelope approximations. Figure 3.3 shows the calculated impulse responses from the carrier rate equations with the adiabatic approximation (CRE I). No damped oscillations is observed even with large pulse amplitude. The de-

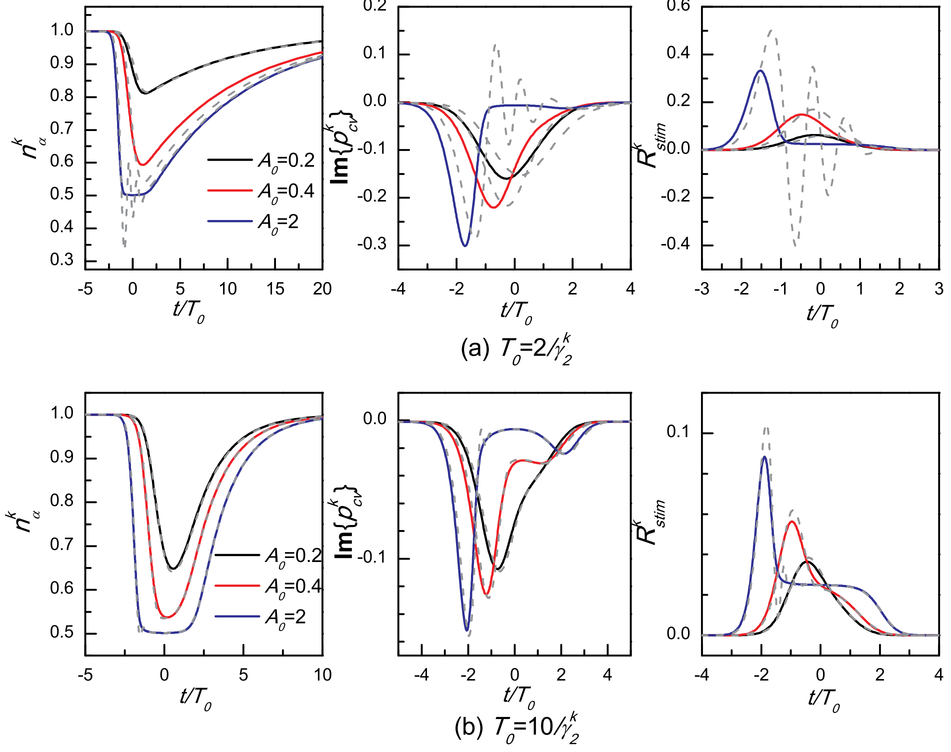

Figure 3.3: Impulse responses calculated from adiabatic carrier rate equations (CRE I) for a single unchirped Gaussian pulse. Results include (left) occupation probabilities n_{α}^{k}, (middle) imaginary part of atomic polarization envelope $\mathbf{Im}\{p_{cv}^{k}\}$ and (right) stimulated emission R_{stim}^{k}. Gaussian pulses have different amplitudes A_0 and pulse widths: (a) $T_0 = \frac{2}{\gamma_2^k}$ (b) $T_0 = \frac{10}{\gamma_2^k}$. The adiabatic results (solid lines) are in comparison with the density matrix equations results (dashed lines). The other relevant parameters are $\gamma_2^k = 1$, $\gamma_\alpha^k = 0.05$, $n_\alpha^{eq,k} = 1$ and $\omega_0 - \omega_k = 0$.

pletion of occupation probability is clamped at the transparency point. As this adiabatic approximation has no memory dependence on the values at earlier times, the density matrix equations results are temporally retarded in comparison with the corresponding envelopes. The temporal difference is proportional to the dephasing times. For pulses with long pulse width, the deviation is negligible.

Figure 3.4 shows the calculated impulse responses from the carrier rate equations with the semi-adiabatic approximation (CRE II). In comparison to the density

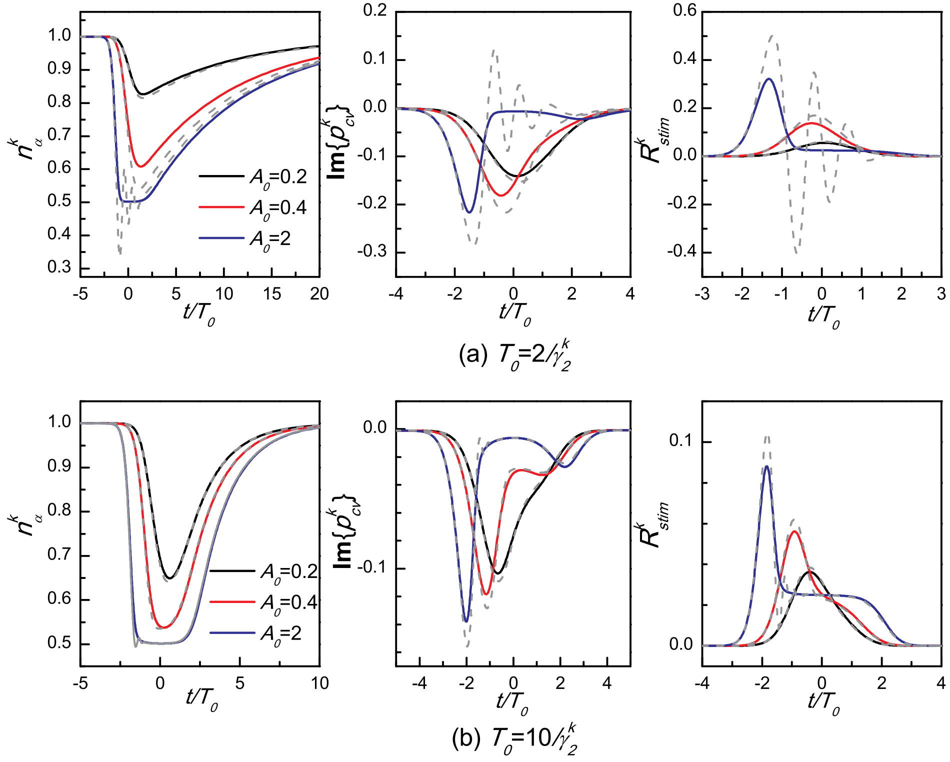

Figure 3.4: Impulse responses calculated from semi-adiabatic carrier rate equations (CRE II) for a single unchirped Gaussian pulse. Results include (left) occupation probabilities n_α^k, (middle) imaginary part of atomic polarization envelope $\mathbf{Im}\{p_{cv}^k\}$ and (right) Stimulated emission R_{stim}^k. Gaussian pulses have different amplitudes A_0 and pulse widths: (a) $T_0 = \frac{2}{\gamma_2^k}$ (b) $T_0 = \frac{10}{\gamma_2^k}$. The semi-adiabatic results (solid lines) are in comparison with the Density matrix equations results (dashed lines). The other relevant parameters are: $\gamma_2^k = 1$, $\gamma_\alpha^k = 0.05$, $n_\alpha^{eq,k} = 1$ and $\omega_0 - \omega_k = 0$.

matrix equation results, the corresponding envelopes shows a similar retardation effect. As pulse amplitude increases, this approximation works at the expense of a reduction of magnitude especially for the atomic polarization during the leading edge of pulse. This approximation is capable to reproduce the results when the occupation probabilities are weakly depleted with small pulse amplitudes. For pulses with long pulse width, the deviation is also negligible.

For a better understanding of damped oscillation properties, the discussion can

be extended to the case of non-zero frequency detuning between optical carrier and interband transition. Moreover, investigations of chirped pulse response might reveal significant contributions from frequency chirping as well as amplitude of the optical signal.

Notice that similar nonlinear coherent resonance behaviors have been widely discussed in atomic-like system based on Bloch equations [99, 100, 101, 102], where proper restrictive conditions need to be fulfilled to observe such strong oscillations. However, these coherent resonance behaviors are highly unlikely to appear in active semiconductor structures at room temperature and for high carrier density [103, 104]. Thus different decoherence effects like strong dephasing mechanisms, renormalization, homogenous and inhomogeneous broadening need to be considered.

3.4 Small-signal Harmonic Analysis

This section will discuss general approaches in small-signal harmonic analysis of the semiclassical two-level system for light matter interaction in a semiconductor medium. Namely, we will determine the sinusoidal steady state response of density matrix equations as well as approximations for these. For simplicity, we still use the simple exponential relaxation expression Eq. (3.15) as in the previous section.

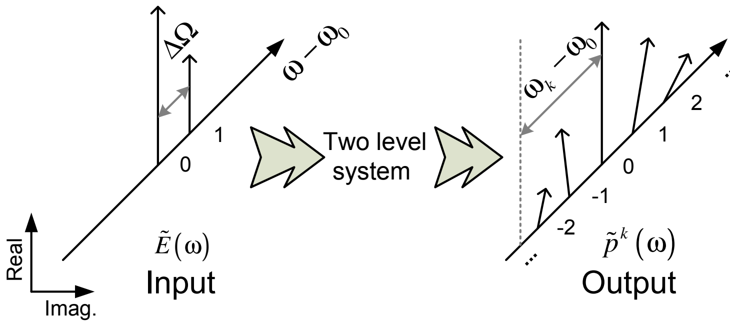

Figure 3.5: The small-signal response of polarization as computed by harmonic analysis in a two-level system. The input electric field is sinusoidally modulated at an arbitrary modulation frequency.

The basic idea of harmonic analysis is to compute the steady state responses, e.g., the one of polarization $\tilde{p}^k(\omega)$, to an sinusoidally driven electric field perturbation $E(t) = \frac{\hbar\gamma_2^k}{2d_k}\left(A_0 + A_1 e^{-i\Delta\Omega t}\right) e^{-i\omega_0 t} + c.c.$ at an arbitrary single modulation frequency $\Delta\Omega$ as illustrated in Figure 3.5. A_0 and A_1 are the corresponding pump and probe electric field envelope normalized by $\frac{\hbar\gamma_2^k}{2d_k}$. For simplicity, A_0 and A_1 are kept as real values.

Based on the perturbative principle of small-signal analysis, the starting point of the small signal analysis is a static situation with a CW electric field input. By simply keeping the time differential terms of density matrix equation as zero, a static solution can be solved for. Then the response to a perturbation can be obtained by performing Taylor expansion around the DC static solution. All the

harmonic terms can be rearranged in the general form as:

$$A_0 + A_1 e^{-i\Delta\Omega t} \Rightarrow \sum_{m=-M}^{M} p_{cv,m}^{k} e^{-im\Delta\Omega t} \tag{3.28}$$

$$A_0 + A_1 e^{-i\Delta\Omega t} \Rightarrow \sum_{m=-M}^{M} n_{\alpha,m}^{k} e^{-im\Delta\Omega t} \tag{3.29}$$

In general, the density matrix equations for a time-varying two-level system, Eq. (3.8) and (3.9), have responses at harmonics with different orders. The response will be determined by the modulation frequency $\Delta\Omega$, pump intensity $|A_0|^2$ as well as frequency detuning between the interband transition and optical carrier $\omega_k - \omega_0$. Detailed derivations of the general formalism for harmonic analysis can be found in Appendix B.1.

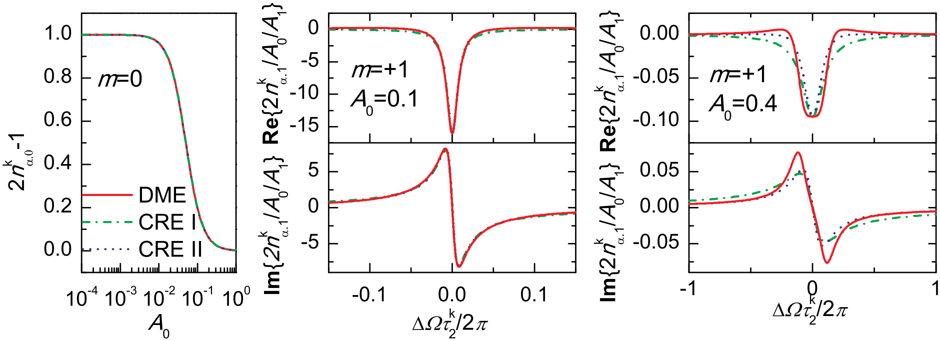

Figure 3.6: Harmonic responses of a two-level system regarding occupation probability $n_{\alpha,m}^{k}$ with different orders m based on different models. (left) the static population inversion with $m = 0$. The real and imaginary part of the first-order harmonic responses $m = +1$ with two different pump field amplitudes: (middle) $A_0 = 0.1$ and (right) $A_0 = 0.4$. A_0 and A_1 are the corresponding electric field amplitude of pump and probe. The models include density matrix equations (DME, solid lines), carrier rate equations with the adiabatic (CRE I, dash-dotted lines) and semi-adiabatic approximation (CRE II, dotted lines). The other relevant parameters are: $\gamma_2^k = 1/\tau_2^k = 1$, $\gamma_\alpha^k = 0.01$, $n_\alpha^{eq,k} = 1$ and $\omega_0 - \omega_k = 0$.

We start by discussing the case of zero frequency detuning between the interband transition and optical carrier $\omega_k - \omega_0 = 0$. Figure 3.6 shows a calculated harmonic response regarding occupation probability $n_{\alpha,m}$ based on density matrix equations

model (DME) and two types of carrier rate equations with the adiabatic and semi-adiabatic approximation (CRE I and II).

Figure 3.6(left) shows the depletion of population inversion $2n_{\alpha,0}-1$ as the pump electric field amplitude A_0 (pump intensity $\propto |A_0|^2$) increases. For this static term, the conditions for adiabatic and semi-adiabatic approximation are automatically satisfied. So all three models provide exactly the same static solution regarding occupation probabilities. The harmonic terms of occupation probabilities, which can also be called population pulsation terms fulfills: $n^k_{\alpha,m} = {n^k_{\alpha,-m}}^*$.

Figure 3.6(middle) and (right) show the first-order harmonic term of population inversion $2n^k_{\alpha,m}$, $(m = \pm 1)$ as a function of normalized modulation frequency $\Delta\Omega\tau^k_2$, which reflects the oscillations of the corresponding carriers. For a relatively small pump field amplitude $A_0 = 0.1$ (even through the static population inversion is close to complete depletion), all three models show similar carrier oscillations properties. In this case, the carrier relaxations rates γ^k_α determine the appearance as a Lorentzian oscillator. For larger pump field amplitude $A_0 = 0.4$ (which pushes the population inversion to deeper depletion), the situation becomes complex. Firstly, the magnitude of the harmonic amplitudes decreases as most of the carrier populations are depleted and not available for the oscillation. Secondly, while the adiabatic-approximated carrier rate equations still lead to a Lorentzian-oscillator appearance with a much wider bandwidth $\gamma >> \gamma^k_\alpha$, the other two models provide richer oscillation details, in particular at modulation frequencies higher than γ^k_α. It is a natural outcome as these three models have different validity and treatments regarding the modulation frequency and frequency detuning. Fortunately, the calculated results within the narrow bandwidth $\sim \gamma^k_\alpha$ are still fairly close to each other.

By expanding Eq. (3.14) into the form of (3.28), we have the general expression of atomic polarization for density matrix equations:

$$p^k_{cv,m} = \frac{\gamma^k_2}{2} L_k(\omega_0 + m\Delta\Omega) \times \left\{ \sum_{m_1} 2n^k_{\alpha,m_1} A_{m-m_1} - A_m \right\} \tag{3.30}$$

where $L_k(\omega_0 + m\Delta\Omega)$ is a Lorentzian function that depends on the modulation frequency and its corresponding orders. For the adiabatic approximation, the Lorentzian function has been approximated as a constant determined by the frequency optical carrier $L_k(\omega_0)$. The semi-adiabatic approximation has another ex-

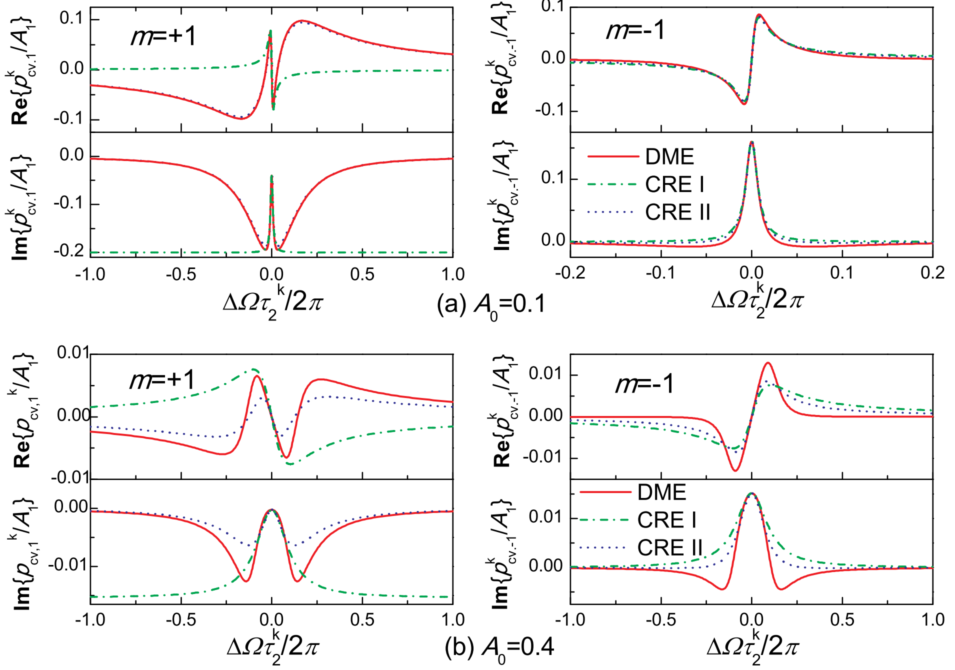

Figure 3.7: Harmonic responses of a two-level system regarding atomic polarization $p^k_{cv,m}$ based on different models for two different pump amplitudes (a) $A_0 = 0.1$ and (b) $A_0 = 0.4$. Two harmonic orders have been considered: (left) m=+1 (left) and (right) m=-1. A_0 and A_1 are the corresponding electric field amplitude of pump and probe. The equation models include density matrix equations (DME, solid lines), carrier rate equations with the adiabatic (CRE I, dash-dotted lines) and semi-adiabatic approximation (CRE II, dotted lines). The other relevant parameters are: $\gamma^k_2 = 1/\tau^k_2 = 1$, $\gamma^k_\alpha = 0.01$, $n^{eq,k}_\alpha = 1$ and $\omega_0 - \omega_k = 0$.

pression as,

$$p^k_{cv,m} = \frac{\gamma^k_2}{2} \sum_{m_1} 2L_k(\omega_0 + (m - m_1)\Delta\Omega) n^k_{\alpha,m} A_{m-m_1} - \frac{\gamma^k_2}{2} L_k(\omega_0 + m\Delta\Omega) A_m \quad (3.31)$$

Figure 3.7 shows the corresponding calculated harmonic responses regarding atomic polarization $p^k_{cv,m}$ as a function of normalized modulation frequency $\Delta\Omega\tau^k_2$. The atomic polarization is normalized by the probe field amplitude A_1. For the harmonic term with order of $(m = \pm 1)$, the polarizations of density matrix equations

have the form as

$$p^k_{cv,1} = L_k(\omega_0 + \Delta\Omega)\gamma^k_2 \left[2n^k_{\alpha,1}A_0 + (2n^k_{\alpha,0} - 1)A_1\right] \quad (3.32)$$

$$p^k_{cv,-1} = L_k(\omega_0 - \Delta\Omega)\gamma^k_2 2n^k_{\alpha,-1}A_0 \quad (3.33)$$

where the polarization terms $p^k_{cv,1}$ has a contribution corresponding to scattering from pump field induced by the carrier population pulsation as well as a contribution from the DC carrier population terms. The polarization term $p^k_{cv,-1}$ also has a contribution from pump field to build up a new field component at the conjugated frequency $-\Delta\Omega$. The adiabatic approximation by replacing the Lorentzian function with a constant value $L_k(\omega_0)$ simply omits the wide bandwidth properties $(\Delta\Omega \sim \gamma^k_2)$. Semi-adiabatic solutions are intermediate for these two approaches. For a relatively small pump field amplitude $A_0 = 0.1$, all three methods have similar responses in the narrow bandwidth $\Delta\Omega \sim \gamma^k_\alpha$. Both solutions from density matrix equations and semi-adiabatic approximation keep similar broadband spectral information $\Delta\Omega \sim \gamma^k_2$. For larger pump field amplitude $A_0 = 0.4$ (which pushes the population inversion to deeper depletion), the solutions obtained from these three models deviate from each other. Still the narrow bandwidth responses $(\Delta\Omega \sim \gamma^k_\alpha)$ are fairly close to each other.

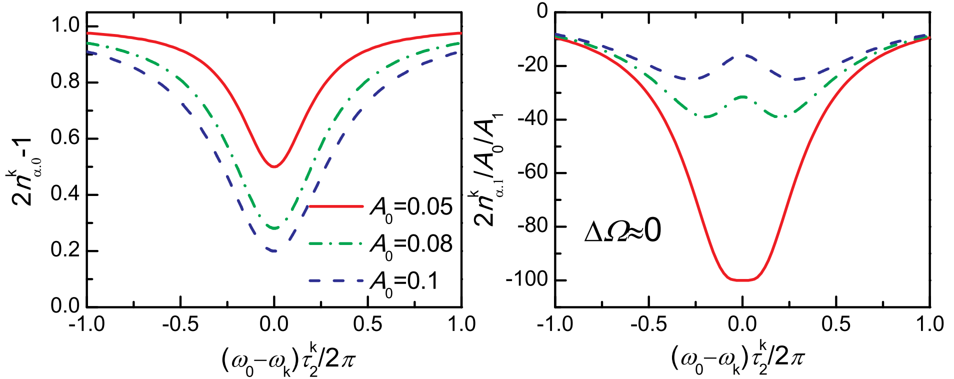

Figure 3.8: Impact of frequency detuning $(\omega_0 - \omega_k)$ on the low modulation frequency $(\Delta\Omega \approx 0)$ harmonic responses of a two-level system regarding occupation probabilities $n^k_{\alpha,m}$ for m=0 (left) and m=+1 (right). A_0 and A_1 are the corresponding electric field amplitude of pump and probe. The other relevant parameters include $\gamma^k_2 = 1/\tau^k_2 = 1$, $\gamma^k_\alpha = 0.01$ and $n^{eq,k}_\alpha = 1$.

For an inhomogeneously broadened set of two-level systems with a span of frequency detuning between the interband transition and optical carrier $\omega_k - \omega_0$, there is a more general question about how the inhomogeneous broadening changes the harmonic responses. Figure 3.8 shows corresponding harmonic responses regarding occupation probabilities as a function of $\omega_k - \omega_0$ at the limit of low modulation frequency $\Delta\Omega \approx 0$. At this low modulation frequency, density matrix equation and its approximations provide nearly identical solutions. For the DC part of the population inversion $2n^k_{\alpha,0} - 1$ shown in Figure 3.8(left), it is a typical saturation or bleaching appearance determined by:

$$2n^k_{\alpha,0} - 1 = \frac{2n^{k,eq}_{\alpha} - 1}{1 + \mathbf{Im}\{L^*_k(\omega_0)\}|A_0|^2 {\gamma^k_2}^2 / \gamma^k_\alpha} \tag{3.34}$$

As the interband transition ω_k is far from optical carrier frequency ω_0, the population inversion is less bleached. As the pump field A_0 (pump power $\propto |A_0|^2$) increases, the full-width of half maximum is *power broadened* (well known in two-level laser theory [90]) as:

$$2\gamma^k_2 \left(1 + \mathbf{Im}\{L^*_k(\omega_0)\}|A_0|^2 {\gamma^k_2}^2 / \gamma^k_\alpha\right) \tag{3.35}$$

The corresponding harmonic terms of population inversion $2n^k_{\alpha,1}$ shown in Figure 3.8(right), is given as:

$$\lim_{\Delta\Omega \to 0} 2n^k_{\alpha,1} = -\frac{(2n^k_{\alpha,0} - 1)A_0 A_1 {\gamma^k_2}^2}{2\left(-\gamma^k_\alpha + \mathbf{Im}\{L^*_k(\omega_0)\}A_0^2 {\gamma^k_2}^2\right)} \tag{3.36}$$

which has a denominator term depending on the frequency detuning and pump intensity. As the pump intensity increases, the magnitude of the relative response decreases as the population inversion $2n^k_{\alpha,0} - 1$ in the numerator decreases. Meanwhile, as the pump intensity increases and pushes the population inversion into deep depletion, the denominator starts to play the role and change the shape of the response. The maximum magnitude starts to shift to frequency detuning $|\omega_0 - \omega_k|$ with non-zero values. When the pumping intensity becoming stronger, the population pulsation at the transition levels with a frequency detuning $|\omega_0 - \omega_k| \sim \gamma^k_2$ off the optical carrier might still has a significant contribution.

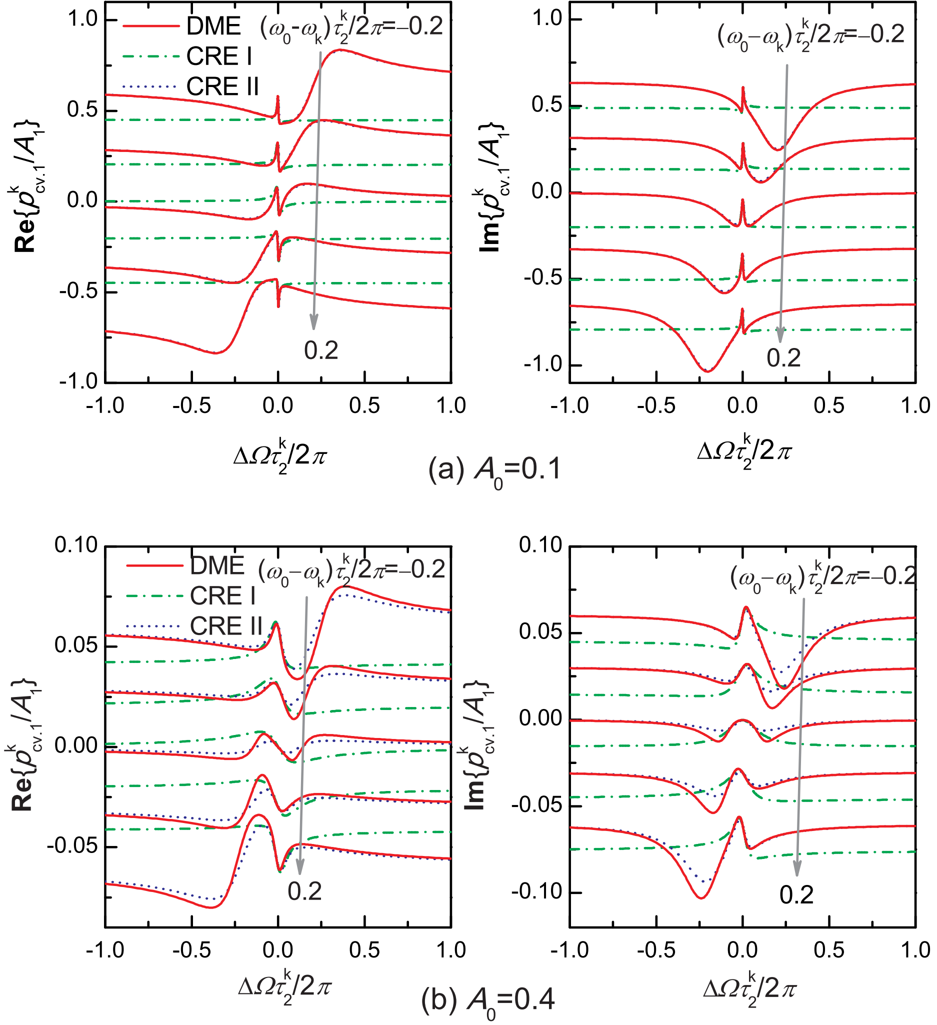

Figure 3.9: Impact of frequency detuning $(\omega_0 - \omega_k)$ *on harmonic responses of a two level system regarding atomic polarization* $p^k_{cv,m}$ *with m=+1 (the* **probe***) as a function modulation frequency* $\Delta\Omega$ *for two pump field amplitudes (a)* A_0*=0.1 (b)* $A_0 = 0.4$*. The models include density matrix equations (DME, solid lines), carrier rate equations with the adiabatic (CRE I, dash-dotted lines) and semi-adiabatic approximation (CRE II, dotted lines). In each subplot,* $(\omega_0 - \omega_k)/2\pi$ *changes from 0.2 (bottom) to -0.2 (top). The responses are stacked with constant offsets. The other relevant parameters are:* $\gamma_2^k = 1/\tau_2^k = 1$, $\gamma_\alpha^k = 0.01$ *and* $n_\alpha^{eq,k} = 1$.

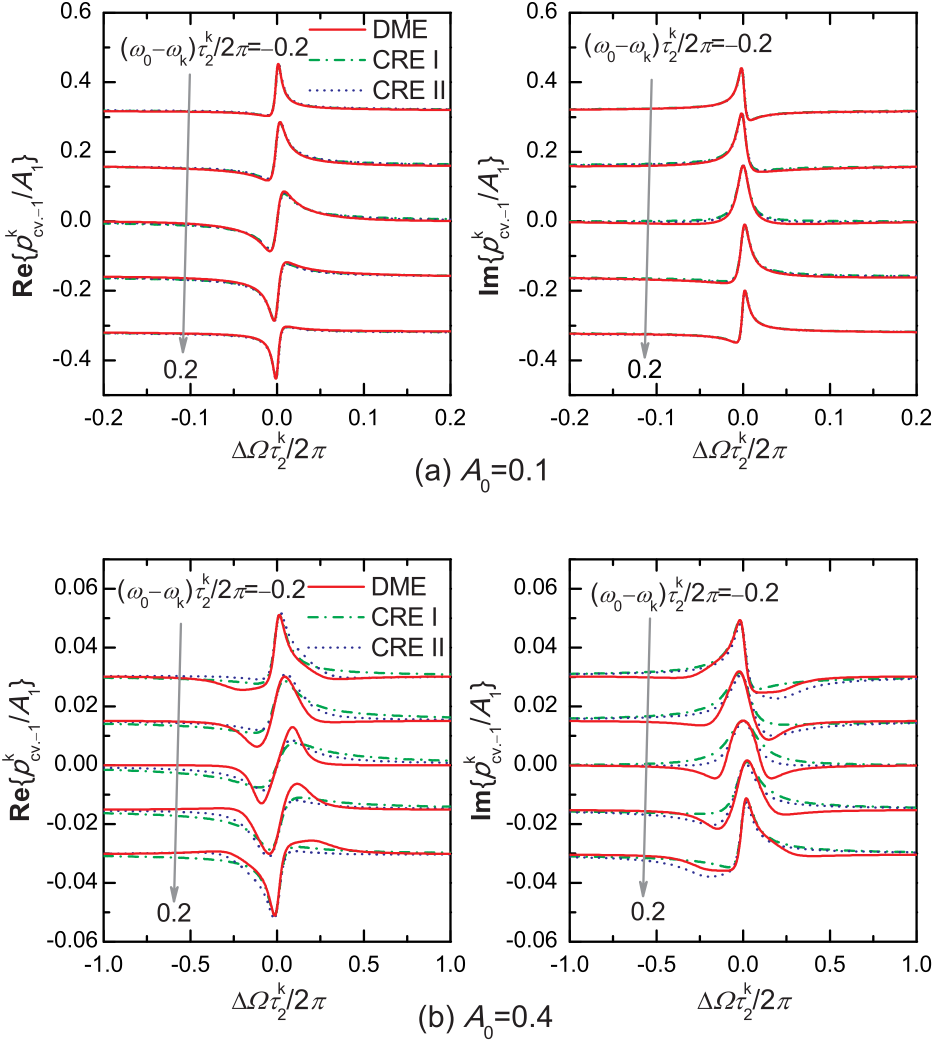

Figure 3.10: Impact of frequency detuning $(\omega_0 - \omega_k)$ on harmonic responses of a two level system regarding atomic polarization $p^k_{cv,m}$ with m=-1 (the ***conjugate****) as a function modulation frequency $\Delta\Omega$ for two types of pump field amplitude (a) A_0=0.1 (b) $A_0 = 0.4$. The models include density matrix equations (DME, solid lines), carrier rate equations with the adiabatic (CRE I, dash-dotted lines) and semi-adiabatic approximation (CRE II, dotted lines). In each subplot, $(\omega_0 - \omega_k)/2\pi$ changes from 0.2 (bottom) to -0.2 (top). The responses are stacked with constant offsets. The other relevant parameters are: $\gamma_2^k = 1/\tau_2^k = 1$, $\gamma_\alpha^k = 0.01$ and $n_\alpha^{eq,k} = 1$.*

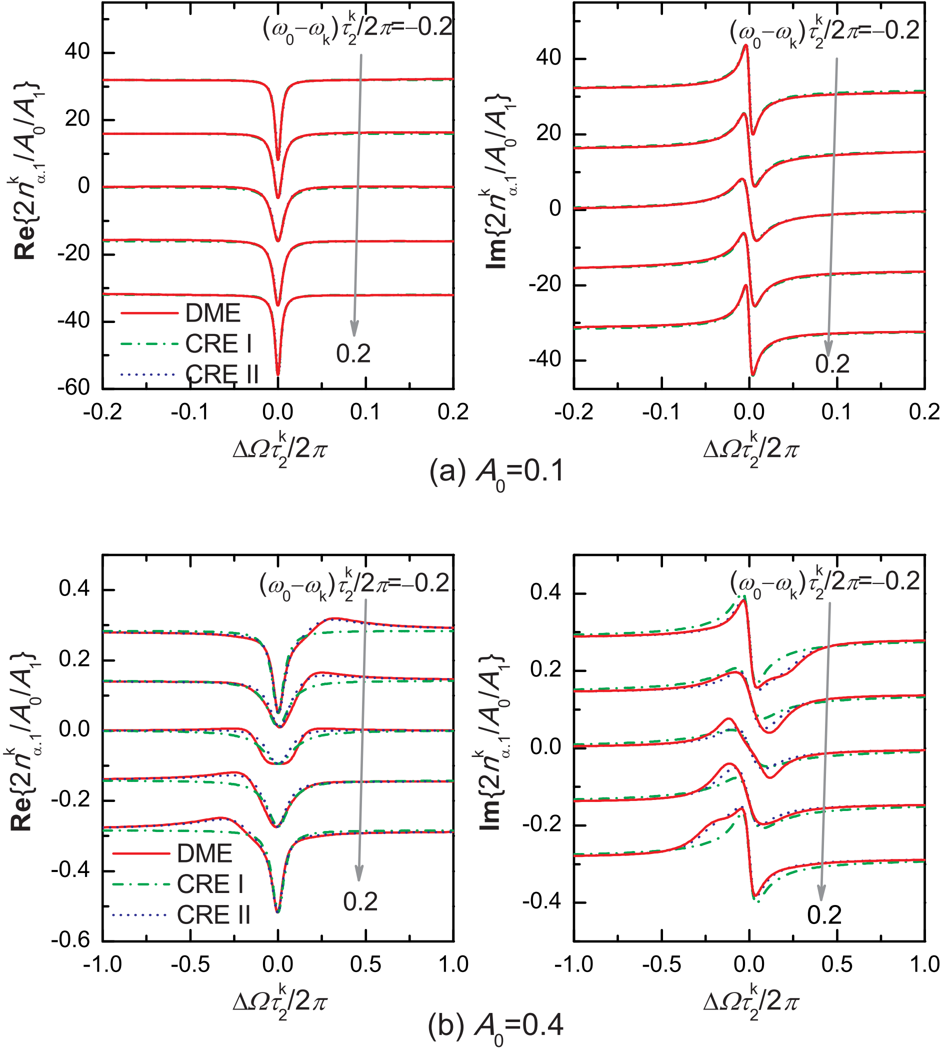

Figure 3.11: Impact of frequency detuning $(\omega_0 - \omega_k)$ on harmonic responses of a two level system regarding occupation factors, $n^k_{\alpha,m}$ with m=+1, as a function modulation frequency $\Delta\Omega$ for two types of pump field amplitude (a) A_0=0.1 (b) $A_0 = 0.4$. The models include density matrix equations (DME, solid lines), carrier rate equations with the adiabatic (CRE I, dash-dotted lines) and semi-adiabatic approximation (CRE II, dotted lines). In each subplot, $(\omega_0 - \omega_k)/2\pi$ changes from 0.2 (bottom) to -0.2 (top). The responses are stacked with constant offsets. The other relevant parameters are: $\gamma^k_2 = 1/\tau^k_2 = 1$, $\gamma^k_\alpha = 0.01$ and $n^{eq,k}_\alpha = 1$.

Figure 3.9, 3.10 and 3.11 illustrate the corresponding harmonic responses as a functions of modulation frequency $\Delta\Omega$ for a span of frequency detuning $\omega_0 - \omega_k$. Density matrix equations and carrier rate equations with two kinds of approximations have been investigated. In general, several issues can be highlighted:

- **All three models are capable to reproduce similar narrow-bandwidth ($\Delta\Omega \sim \gamma_\alpha^k$) behavior for a wide spread of frequency detuning values $\omega_0 - \omega_k$ even in the presence of a strong pump intensity;**
- **Density matrix equations provide richer dynamics over a wide-bandwidth ($\Delta\Omega \sim \gamma_2^k$). The harmonic response as a function of modulation frequency can be highly asymmetric for different frequency detuning values $\omega_0 - \omega_k$;**
- **Carrier rate equations with semi-adiabatic approximation give similar results as the ones of the density matrix equations up to a reasonable pump intensity with intermediate computation complexity;**
- **Carrier rate equations with adiabatic approximations provide a simple approach dedicated for narrow-bandwidth investigations with less computation complexity.**

The harmonic analysis presented here is a general fast mathematical tool to tackle some issues of the oscillation features presented in a set of coupled rate equations. Different solutions can be chosen to interpret the dynamics with different levels of approximations regarding the modulation bandwidth.

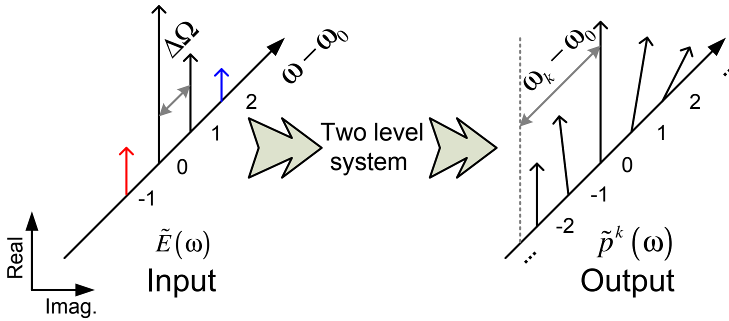

(a) Integer multiples of a fundamental modulation frequency as input

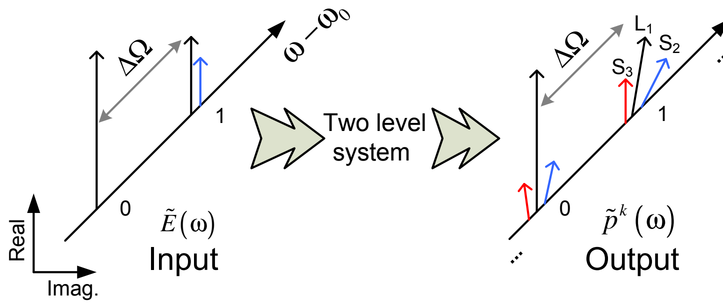

(b) Non-integer multiples of a fundamental modulation frequency as input

Figure 3.12: The small-signal response of polarization as computed by intermodulation analysis in a two-level system. The input electric field is sinusoidally modulated with multiple arbitrary modulation frequencies.

The basic harmonic analysis can be extended to other configurations by choosing different inputs as stimulus, such as intermodulation analysis with an electric field containing multiple modulation frequencies. As shown in Figure 3.12, the intermodulation analysis leads to two different categories depending on whether the modulation frequency differences are integer or non-integer multiple of a fundamental modulation frequency. In general, it is very similar to the harmonics analysis in the electronics technology [105, 106]. As the field of microwave photonics is getting mature, the corresponding analysis for photonic devices, in particular active semiconductor material and device response, in the presence of different millimeter wave signals will become increasingly interesting.

Chapter 4

Modeling of QD SOAs

The model of QD SOAs used in this thesis is normally referred to as Multi Population Rate Equation Model (MPREM), which is an rate equation approach including the inhomogeneous broadening effects by considering spectral subgroups of QDs [30, 31, 42, 43, 44]. In this approach QDs belonging to the same spectral subgroup are assumed identical. The inhomogeneous broadening is introduced by weighting the relevant quantities for each QD groups with a proper distribution function. The advantage of this approach is that only a relative small number of dots (depending on the spectral discretization) have to be considered. Similar treatment have also been used in a more sophisticated system based on semiconductor Maxwell-Bloch equation [46, 45]. Moreover, balanced scattering models are used to describe the ultrafast carrier intra-dot transitions between discrete QDs states with pairs of capture and escape processes. Phenomenological rates for these capture/escape processes depend on the carrier density and temperature via phonon and Auger assisted contributions [31, 23]. The typical characteristic times ranging from subpicoseconds to tens of picoseconds can be extracted from pump-probe type measurements [32, 33, 34, 35, 36] or more comprehensive carrier scattering calculation [26, 27, 28, 29].

As a simplification with adiabatic approximations, the rate equation approach might lose some details of the relaxation processes and nonequilibrium situations calculated by semiconductor Maxwell-Bloch equations in the more fundamental level studies [45, 46, 47, 48]. For example, the coherent effects, which is the temporal

dynamics resolved from femtoseconds to picoseconds, are of major consideration in modeling experiments with ultrafast pump and probe pulses [95, 107]. On the other hand, the rate equation approach, even neglecting inhomogeneous broadening, is more preferred in the investigations of optical signal processing in terms of the analytical sophistication. Therefore the purpose of implementing MPREM model is to bridge the gap between the fundamental physics study and device simulation for optical signal processing.

The first section describes the QD SOAs device structure for modeling. The second part presents the carrier dynamics model for QDs as well as a simple intensity propagation equation. The third section briefly discusses the numerical implementation. The typical parameter values can be found in Appendix E.

4.1 Device Structure

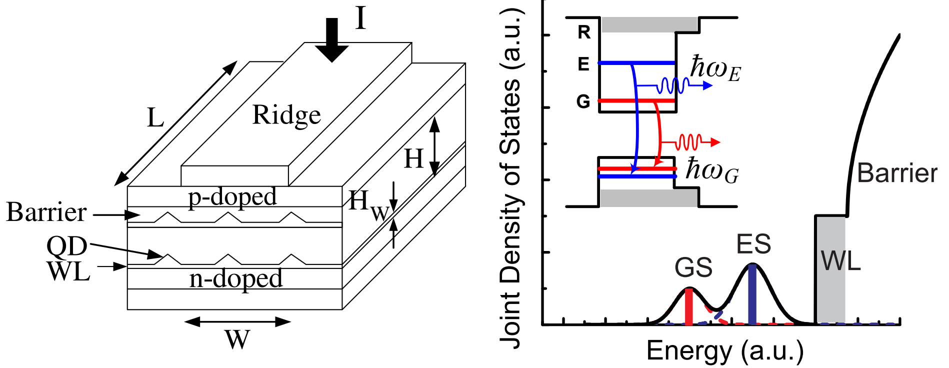

Figure 4.1: Schematic illustration of the structure and band diagram of QD SOAs.

Our numerical model has been developed to describe a QD SOAs with inhomogeneously broadened QDs layers as the active gain medium in a ridged optical waveguide as shown in Figure 4.1(left). The volume of the active region V_a has the form:

$$V_a = WHL \tag{4.1}$$

where L, W, H are the length, width and height of active region. This region contains a number of QD layers, n_l, each including a wetting layer (WL), which

is typical for samples based on the SK growth method. The WL is modeled as a narrow quantum well of width H_W and volume V_W:

$$V_W = WLH_W \tag{4.2}$$

The density of QDs per layer is denoted D_D and the volume of an average dot in the ensemble V_0. The QDs and WL are surrounded by a barrier material, which is assumed to separate the QD layers to the extent that they do not couple directly. Furthermore, tunneling between dots within the same layer is neglected.

Current I is supplied through the top and bottom metal contacts, and carriers enter the undoped active region by drift and diffusion through the p- and n-doped regions. In the numerical models, transport effects are neglected [1] and current is assumed to be injected directly into the barrier or WL in a uniform manner along the entire length of the device. Thus the uniform density of injected carriers in active region R_{inj} per unit time (with the unit of $\mathrm{m}^{-3} \cdot \mathrm{s}^{-1}$) has the form:

$$R_{inj} = I/(V_a q) = I/(WLHq) = D_c/(Hq), \quad D_c \equiv I/WL \tag{4.3}$$

Where D_c is denoted as current density with the unit of $\mathrm{A/m^2}$, q the magnitude of electronic charge.

Optical confinement is supplied by a separate confinement heterostructure (SCH). The dimensions of the typical waveguide used for SOAs are sufficiently small to allow the device remain single mode under all operating conditions. The overlap between the guided modes (optical mode volume can be approximated as $V_{mod} = WLH_{mod}$ with H_{mod} as a normalized mode height) and the active region, the confinement factor of active region Γ_A is defined by Eq. (A.7). Typical values of Γ_A is 0.2-0.4. The confinement factor of each WL layer Γ_{W0} can be calculated in a similar way. The overall confinement factor of WL layers Γ_W can be approximated as $\Gamma_W = \Gamma_{W0} n_l$. In the models reflections at the facets are in most cases neglected. The lasing condition is assumed to be not satisfied in this thesis.

In order to investigate the maximized carrier confinement effects in QDs, both electrons and holes are considered to be confined in the same materials. Our investigation is based on a simple QD electronic band structure [31] used for describing 1100nm inhomogeneously broadened InAs/GaAs QDs. Energy separations

[1] The carrier transport effect as well as electrical parasitics can be included following treatments used for quantum well lasers [108, 109].

and other relevant quantities in both conduction band and valence band can be calculated as in Appendix C.

As shown in Figure 4.1(right), we only consider the two lowest discrete states in the QDs: the ground (G) state (the lower one with degeneracy ε_G) and the excited (E) state (the upper one with degeneracy ε_E). An reservoir (R) including wetting layer (WL) and barrier (B) have continuous bands for both electron and holes. And we approximate the inhomogeneous broadening of quantum dots as a Gaussian distribution $\mathcal{G}_x$ with a spectral full width at half maximum (FWHM) γ_G (γ_E) centered at $\hbar\omega_G$ ($\hbar\omega_E$) for the ground (excited) states [2]:

$$\mathcal{G}_X(E_X^{tr}, \hbar\omega_X) = \frac{\sqrt{8\ln 2}}{\sqrt{2\pi}\gamma_X} \exp\left[-\frac{1}{2}\left(\frac{\sqrt{8\ln 2}(E_X^{tr}, \hbar\omega_X)}{\gamma_X}\right)^2\right], \qquad X = G, E \quad (4.4)$$

Here E_X^{tr} is the transition energy. We further divide the quantum dots into subgroups with a small spectral interval $2\delta_X$. The corresponding i^{th} dot subgroup density D_D^i is :

$$D_D^i = D_D \int_{E_X^{tr,i}-\delta_X}^{E_X^{tr,i}+\delta_X} \mathcal{G}_X(E_X^{tr}, \hbar\omega_X) dE_X^{tr}, \qquad X = G, E \quad (4.5)$$

4.2 Modeling of Carrier Dynamics of QDs

In the following, we outline the balanced scattering description of electron intersubband transition between discrete QD levels. Similar treatment can also be used for hole dynamics [110]. Due to the large effective mass and small energy level spacing in valence band, we treat it with local carrier density description that has been used for carrier dynamical description in the gain medium with continuum states [111]. The static [31] and dynamic [42] ASE noise properties are neglected.

4.2.1 Electron dynamics of QDs

A set of carrier rate equations for electron density of ground state N_G^i (given by occupation factor $f_{G,c}^i$ times density of states ρ_G^i) and the excited state N_E^i (given by

[2]This approximation follows [43]. The approximation in [31] is an inhomogeneous broadening function with respect to the conduction band energy

occupation factor $f^i_{E,c}$ times density of states ρ^i_E) corresponding to i^{th} dot subgroup (normalized to the single average dot volume V_0) is used:

$$\partial_t N^i_E = -R^{E,i}_{stim} - \frac{N^i_E}{\tau_{spon}} + \partial_t N^i_E\Big|_{RE} - \partial_t N^i_E\Big|_{EG} \quad (4.6)$$

$$\partial_t N^i_G = -R^{G,i}_{stim} - \frac{N^i_G}{\tau_{spon}} + \partial_t N^i_G\Big|_{RG} + \partial_t N^i_E\Big|_{EG} \quad (4.7)$$

where the first terms on the right hand side (RHS) of Eq. (4.6) and (4.7) refer to the stimulated emission/absorption which will be described in the latter section. The second terms refer to the spontaneous recombination [3] determined by a simple spontaneous recombination rate $1/\tau_{spon}$. The last two terms denote the carrier relaxations between discrete states G, E and reservoir R in the form of a balanced scattering description:

$$\partial_t N^i_E\Big|_{RE} = \rho^i_E \frac{f_W(1-f^i_{E,c})}{\tau^i_{RE}} - \rho^i_E \frac{f^i_{E,c}(1-f_W)}{\tau^i_{ER}} \quad (4.8)$$

$$\partial_t N^i_G\Big|_{RG} = \rho^i_G \frac{f_W(1-f^i_{G,c})}{\tau^i_{RG}} - \rho^i_G \frac{f^i_{G,c}(1-f_W)}{\tau^i_{GR}} \quad (4.9)$$

$$\partial_t N^i_E\Big|_{EG} = \rho^i_E \frac{f^i_{E,c}(1-f^i_{G,c})}{\tau^i_{EG}} - \rho^i_G \frac{f^i_{G,c}(1-f^i_{E,c})}{\tau^i_{GE}} \quad (4.10)$$

Here f_W are the occupation probabilities at the WL conduction band edge. $1/\tau^i_{XY}$ is the electron transition rate in QDs from state X to state Y, with X, Y = R, E, G. The rates for these capture/relaxation processes depends on the carrier density and temperature via phonon and Auger assisted contributions, for which we use a phenomenological model [31] as following, the downward electron transition rates are defined as

$$\begin{cases} 1/\tau^i_{RE} = Z^P_{RE} + Z^A_{RE} f_W, \\ 1/\tau^i_{RG} = Z^P_{RG} + Z^A_{RG} f_W, \\ 1/\tau^i_{EG} = Z^P_{EG} + Z^A_{EG} f_W, \end{cases} \quad (4.11)$$

where Z^P_{XY} denoting the pure phonon assisted capture rates and Z^A_{XY} denoting the Auger assisted contributions for the corresponding downward transitions between

[3] Strictly the spontaneous emission term is proportional to the production of occupation probabilities of conduction band (c) and valence band (v) as $f_c f_v \tau^{-1}_{spon}$.

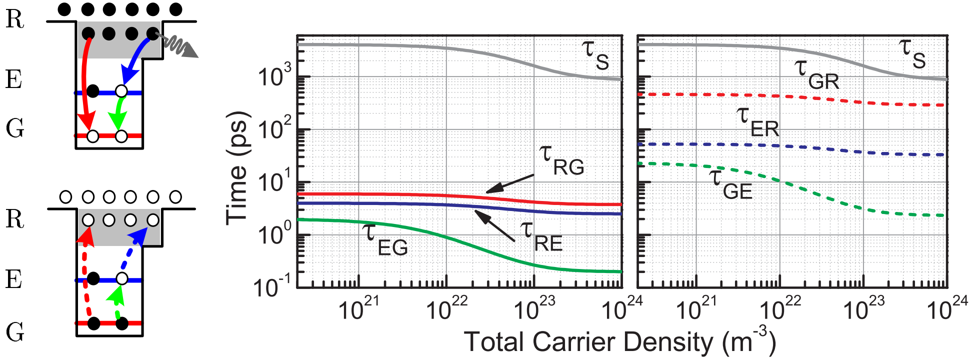

Figure 4.2: Typical characteristic time values for electron transitions in QDs for modeling. Effective carrier lifetime τ_s of reservoir is shown as reference. Parameter values are given in Appendix E.

upper (X) and lower (Y) states (X, Y = R, E or G). The corresponding upward transitions are defined as

$$\begin{cases} 1/\tau^i_{ER} = 1/\tau^i_{RE} \exp\left(-\Delta E^i_{RE}/k_B T\right) \\ 1/\tau^i_{GR} = 1/\tau^i_{RG} \exp\left(-\Delta E^i_{RG}/k_B T\right) \\ 1/\tau^i_{GE} = 1/\tau^i_{EG} \frac{\varepsilon_E}{\varepsilon_G} \exp\left(-\Delta E^i_{EG}/k_B T\right) \end{cases} \tag{4.12}$$

where ΔE^i_{XY} denoting the energy level deference between upper (X) and lower (Y) states (X, Y = R, E or G). k_B is the Boltzmann constant and T is the temperature. Typical time values are shown in Figure 4.2. In this thesis, the refilling of electron in ground states is assumed to be dominated by the carrier relaxation from excited states.

For simplicity, the WL and barrier are assumed to be in quasi-equilibrium at all times and thus no capture effects of carriers from the barrier into WL are included. The electron density of reservoir N_R including both WL N_W and barrier N_B, normalized to the active region volume V_a, is modeled by the following equation [4]:

$$\partial_t N_R = \frac{I}{V_a q} - \frac{N_R}{\tau_s} - \sum_i \xi^i \left\{ \partial_t N^i_E \Big|_{RE} + \partial_t N^i_G \Big|_{RG} \right\} \tag{4.13}$$

[4] The two photon absorption effects can be included following the treatment in [112].

here the last term on the RHS is the superposition of all the electron scatterings between the reservoir and discrete QD states. $\xi^i = \frac{V_0 D_D^i W L n_l}{V_a}$ as volume ratio weighted between i^{th} dot subgroup and the active region. D_D^i is the dot subgroup density. The first term on the RHS of Eq. (4.13) is the current injection. The second term refers to the reservoir carrier loss characterized by an effective carrier lifetime τ_s can be defined as:

$$\begin{cases} 1/\tau_s = \left(\frac{N_W}{\tau_W} + \frac{N_B}{\tau_B}\right) / \left(N_W + N_B\right), \\ 1/\tau_W = A_W + B_W N_W + C_W N_W^2, \\ 1/\tau_B = A_B + B_B N_B + C_B N_B^2, \end{cases} \tag{4.14}$$

here τ_B and τ_W is the carrier lifetime in the barrier and wetting layer, A_W, B_W and C_W (A_B, B_B and C_B) are the coefficient for the non-radiative, radiative and Auger recombination in the WL (barrier).

4.2.2 Hole dynamics in QDs

Meanwhile, the hole dynamics can be treated by introducing the concepts of local carrier density [111]:

$$\partial_t N_{E,v}^i = -\frac{N_{E,v}^i - N_{E,v}^{i,eq}}{\tau_{1h}} - R_{stim}^{E,i} \tag{4.15}$$

$$\partial_t N_{G,v}^i = -\frac{N_{G,v}^i - N_{G,v}^{i,eq}}{\tau_{1h}} - R_{stim}^{G,i} \tag{4.16}$$

where τ_{1h} is the valence band intradot relaxation time approaching to the quasi-equilibrium status $N_{X,v}^{i,eq}$, (X = G, E). For simplicity, τ_{1h} = 100 fs By assuming charge neutrality and quasi-equilibrium in the valence band (including all the discrete and continuum states), a common Fermi energy in the QD valence band can be calculated to estimate the occupation probabilities in the valence band following Eq. (3.16).

4.2.3 Stimulated emission/absorption

The corresponding stimulated emission terms $R_{stim}^{X,i}$, (X = G, E) induced by the photons at $\hbar\omega_p$ has the form:

$$R_{stim}^{X,i} = \frac{L}{\xi^i V_a} \sum_p g_X^{p,i} \frac{P_p}{\hbar\omega_p}, \qquad X = G, E \tag{4.17}$$

where $g_X^{p,i}$, (X = G, E) is the intensity modal gain of photons at energy $\hbar\omega_p$ contributed from E or G states of ith dot subgroup. P_p is optical power. Following the literature [113, 114], optical gain (absorption) coefficient σ_D of a single dot in units of [cross section area]×[energy] is defined as:

$$\sigma_D = \frac{\pi\hbar}{n_r\varepsilon_0 c\hbar\omega} \frac{q^2}{2m_0} \frac{2|M_c|^2}{m_0} |M_E|^2 \tag{4.18}$$

$$|M_E|^2 \equiv \gamma \int F_2(r)F_1(r)d^3r \tag{4.19}$$

where $|M_c|^2$ is the momentum matrix element, $|M_E|^2$ is the envelope matrix element, n_r is the refractive index, $\hbar\omega$ is the photon wavelength, ε_0 is the electric constant, c is the light speed in vacuum, q is the electric charge, m_0 is the free electron mass, γ is the polarization factor, $F_1(r)$ and $F_2(r)$ is the three-dimensional envelope functions for the upper and lower dot states. For simplicity, by using parameter values for InAs material: $\gamma = 1/3$, $\frac{2|M_c|^2}{m_0} = 21.1$ eV, $\hbar\omega = 1.1$ eV, and assuming complete envelope function overlapping, the calculated σ_D is at the scale of 2×10^{-20} m^2eV. It is expected as an overestimated value with a reasonable approximation scale fitting with experimental measurements [114].

The modal gain from the G or E states of ith dot population to photon population p, $g_G^{p,i}$ or $g_E^{p,i}$, is defined as:

$$g_X^{p,i} = \frac{\varepsilon_X D_D n_l \sigma_D}{H_{mod}} Q_X^{p,i}(f_{X,c}^i + f_{X,v}^i - 1), \qquad X = G, E \tag{4.20}$$

$$Q_X^{p,i} = \int_{\hbar\omega_p-\gamma_H}^{\hbar\omega_p+\gamma_H} \int_{E_X^{tr,i}-\delta_X}^{E_X^{tr,i}+\delta_X} \frac{\mathcal{G}_X(E^{tr},\hbar\omega_X)\mathcal{L}(\hbar\omega',E^{tr})}{2\gamma_H} dE^{tr} d(\hbar\omega'), \qquad X = G, E \tag{4.21}$$

here σ_D is the optical gain coefficient, D_D is the QD density per layer, n_l is the number of layers, $f_{X,c}^i$ and $f_{X,v}^i$ are the electron and hole occupation probability evaluated for the transition $E_X^{tr,i}$ of ith dot subgroup. H_{mod} is the effective width of

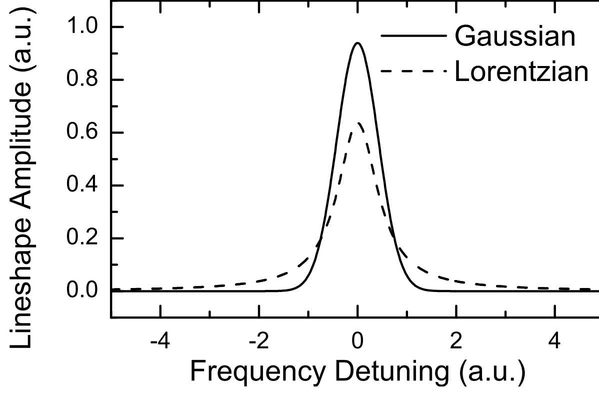

Figure 4.3: Different lineshapes for homogeneous broadening function. Both lineshapes have the same FWHM value and area under.

the optical mode. $Q_X^{p,i}$ donates the coupling between the ith dot subgroup and the photon population p. where $\mathcal{G}_X$ is the Gaussian inhomogeneous broadening function and $\mathcal{L}$ is the homogeneous broadening function, such as Gaussian or Lorentzian lineshapes as shown in Figure 4.3. We keep the assumption that the lineshape has the same FWHM value $2\gamma_H$ and area under. [5]

At the limit of monochromatic wave, a more strict form of spectral intensity modal gain is as following:

$$\begin{aligned} g_X(\omega_0) &= \frac{\varepsilon_X D_D n_l \sigma_D}{H_{mod}} \int_{-\infty}^{\infty} \mathcal{G}_X(E^{tr}, \hbar\omega_X)\mathcal{L}(\hbar\omega_0, E^{tr})[f_{X,c} + f_{X,v} - 1]dE^{tr} \\ &\approx \frac{\varepsilon_X D_D n_l \sigma_D}{H_{mod}} \\ &\quad \times \sum_i \left\{ \int_{E_X^{tr,i}-\delta_X}^{E_X^{tr,i}+\delta_X} \mathcal{G}_X(E^{tr}, \hbar\omega_X)\mathcal{L}(\hbar\omega_0, E^{tr})dE^{tr} \right\} [f_{X,c}^i + f_{X,v}^i - 1] \end{aligned} \tag{4.22}$$

The time-varying description of gain as well as the stimulated emission is a relatively complex quantity. Detailed discussion of different levels of approximations can be found in the previous chapter. Here we follows the adiabatic approximations where the population inversion factors are excluded from spectral integral of homogeneous

[5]This condition leads to undervalued gain based on the Lorentzian lineshape in comparison with the Gaussian lineshape. A variation of the corresponding FWHM values can be used to fix the difference in between. In practise, the Gaussian lineshape is favored for its fast decaying tails.

and inhomogeneous function. In comparison, Eq. (4.20) and (4.21) denotes an averaged intensity gain approximated for an optical signal with a finite narrow bandwidth (averaged over an optical bandwidth of $2\gamma_H$).

4.2.4 Propagation effect

Throughout this thesis, we use the simplest propagation equation for the optical power P_p to estimate the propagation effect [6] in the forward direction passing through the amplifier:

$$\partial_z P_p = \left[\sum_i (g_E^{p,i} + g_G^{p,i}) - \alpha_{int} \right] P_p \tag{4.23}$$

where α_{int} is the internal loss. In this way, only the effect of QDs gain dynamics are included. Extra propagation effects can be considered following Appendix A. The propagation equation can be solved approximately by spatially discretizing the amplifier along the propagation direction, where the carrier diffusion effect between the neighbouring spatial intervals are neglected.

4.3 Numerical Implementation

The models described in this chapter have been implemented in Matlab. The time domain problem is solved using standard ordinary differential equation (ODE) solvers. When carrier densities in QDs have various rapidly changing rates in the time range, the stiffness of the problem begins to influence the computation efficiency of numerical algorithms. We use the solver ODE23s with a flexible time step scheme, which is based on a modified Rosenbrock formula of order 2 [115], to most of our time domain problems (applications for optical signal processing) based on a flexible time step scheme. However, the heavy computational load due to the large number of rate equations (in most case even with a coarse spectral interval, $2\gamma_H$) is still unavoidable. Especially for the periodic signals, a steady state is achieved with a long time range (sufficiently longer than the largest exponential relaxation time) after the first incident pulse. Fourier signal analysis is also computationally

[6] In this thesis, we only consider one polarization mode, i.e., TE mode. The polarization-dependent loss or gain is neglected.

expensive for the steady state responses of the simple harmonic modulated signals at a low repetition rate.

In parallel, we manage to simplify part of the problems by transferring the time-domain problem into the frequency domain. We use a standard nonlinear equation solver (fsolve) [7] to solve the steady response to harmonic modulated signals based on the small-signal perturbation analysis. A semi-analytical approach for the first-order perturbation is presented in Appendix B.2. In this way, results based on the fine spectral interval can be resolved much more efficiently than the equivalent time-domain results. Most of the frequency domain results are presented in the following chapter as the basic properties of QD SOAs.

[7] A proper scaling is required to match the tolerance of errors of all the carrier rate equations.

Chapter 5

Basic Properties of QD SOAs

5.1 Linear Gain and Linewidth Enhancement Factor

Using the static solutions of our QDs carrier dynamics model, we analyze the linear gain and refractive index properties in QD medium. The linear intensity gain/absorption calculated from Eq. (4.22) is proportional to the imaginary part of the linear susceptibility $\mathbf{Im}\{\chi^1\}$ (as in Eq. (A.12)). To be consistent with the optical signal processing results in the latter chapters, we still calculate the averaged intensity gain defined in Eq. (4.20). We introduce a quantity referred to as modal gain change $\Delta g_X(\omega)$ as:

$$\Delta g_X(\omega) \quad = \quad \frac{\varepsilon_X D_D n_l \sigma_D}{H_{mod}} \sum_i Q_X^{p,i} \left[f_{X,c}^i + f_{X,v}^i \right] \qquad X = G, E \tag{5.1}$$

For the real part of the first-order susceptibility $\mathbf{Re}\{\chi^1\}$, the effective index change $\Delta n_X(\omega)$ contributed by intensity gain change $\Delta g_X(\omega)$ can be calculated by using Kramers-Kronig transform:

$$\Delta n_X(\omega) = -\frac{c}{\pi} \mathcal{P} \int_0^\infty d\omega' \frac{\Delta g_X(\omega)}{\omega'^2 - \omega^2} \tag{5.2}$$

The Kramer-Kronig transform can be calculated based on the numerical evaluation of principal integral by extracting the divergent term into the logarithm term [116]. Limited by the finite available optical frequency range ($0 \leq \omega_a < \omega \leq \omega_b$, ω_a and ω_b are the lower and upper frequency limit), we can approximate the exact result through the truncated Kramer-Kronig transform by assuming negligible

variation outside the optical frequency range [117]:

$$
\begin{aligned}
\Delta n(\omega) &\approx -\frac{c}{\pi}\mathcal{P}\int_{\omega_a}^{\omega_b} d\omega' \frac{\Delta g(\omega')}{\omega'^2-\omega^2} \\
&= -\frac{c}{\pi}\mathcal{P}\int_{\omega_a}^{\omega_b} d\omega' \left(\frac{\Delta g(\omega')}{\omega'-\omega} - \frac{\Delta g(\omega')}{\omega'+\omega}\right)\frac{1}{2\omega} \\
&= -\frac{c}{2\pi\omega}\mathcal{P}\int_{\omega_a}^{\omega_b} d\omega' \frac{\Delta g(\omega')}{\omega'-\omega} + \frac{c}{2\pi\omega}\int_{\omega_a}^{\omega_b} d\omega' \frac{\Delta g(\omega')}{\omega'+\omega} \\
&= -\frac{c}{2\pi\omega}\int_{\omega_a}^{\omega_b} d\omega' \frac{\Delta g(\omega')-\Delta g(\omega)}{\omega'-\omega} - \frac{c\Delta g(\omega)}{2\pi\omega}\ln\left(\frac{\omega_b-\omega}{\omega-\omega_a}\right) \\
&\quad + \frac{c}{2\pi\omega}\int_{\omega_a}^{\omega_b} d\omega' \frac{\Delta g(\omega')}{\omega'+\omega}
\end{aligned}
\tag{5.3}
$$

where the first term around the frequency $\omega' \to \omega$ can be approximated as the first-order derivative:

$$
\lim_{\omega'\to\omega} \frac{\Delta g(\omega')-\Delta g(\omega)}{\omega'-\omega} = \frac{\partial \Delta g(\omega)}{\partial \omega}
$$

The accuracy depends on the spectral resolution of the intensity gain change (number of QD subgroups) as well as the step size of the numerical scheme used for integration (for example, based on Simpson's rule).

To quantify the carrier-induced refractive index change, we also use the linewidth enhancement factor (α-factor) defined in Eq. (A.12) as the ratio between the carrier-density induced change of the real and imaginary part of the susceptibility, i.e., corresponding to the changes of the refractive index Δn and gain Δg:

$$
\alpha = -2k_0 \frac{\partial \Delta n(\omega)/\partial N}{\partial \Delta g(\omega)/\partial N} \tag{5.4}
$$

Here, k_0 is the propagation constant in vacuum. N is the quasi-equilibrium definition of carrier density.

For quantum dot semiconductor lasers, a number of experimental works [118, 119, 120, 121] have reported a great variety of values for the α-factor ranging from zero to large values as high as 60. Meanwhile theoretical investigations indicate two optical transition mechanisms governing the linewidth enhancement factor, see in Figure 5.1(a). One is the interband transition [122, 123], where the generated or recombined elecron-hole pairs induce the gain and refractive index change. Detailed modelings considering valence-band mixing effects [124] and coulomb interactions

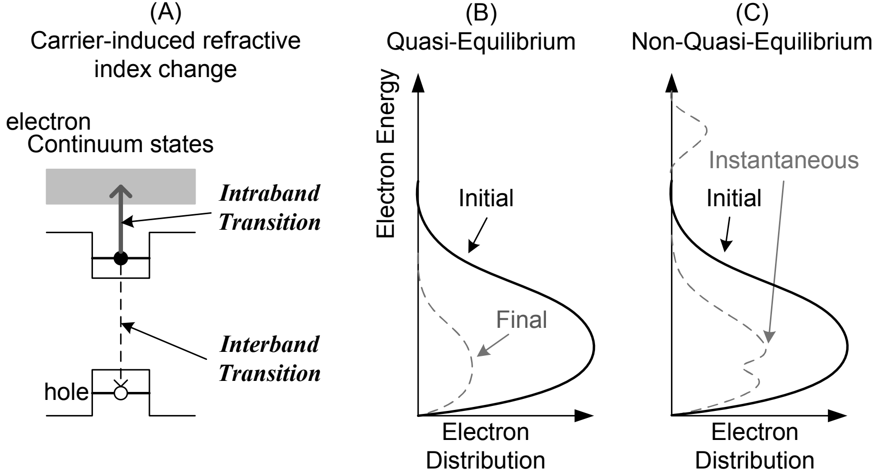

Figure 5.1: Schematic diagram of carrier-induced refractive index change. (a) The band structure of QDs with interband and intraband transitions. Schematic illustration of bulk-like electron (electron-hole pair) distribution under the assumption of (b) quasi-equilibrium Fermi distribution and (c) non-quasi-equilibrium distribution.

[125] predict a small or even negative α-factor. Another is the intraband free-carrier absorption (plasma effect), where an electron or hole, absorbing a photon and transiting to a higher-lying continuum state, gives rise to the gain and refractive index change [126, 127, 128].

Moreover, conventional linewidth enhancement factor as defined in Eq. (5.4) is evaluated with the carrier density change under the quasi-equilibrium (Fermi) distribution, see Figure 5.1(b). Although an instantaneous linewidth enhancement factor has been justified in the transient response regime (as phase change divided by the gain change) [128], the understanding of the carrier dynamical contributions under non-quasi-equilibrium condition as shown in Figure 5.1(c) are still more or less kept in a black-box status. In particular, different experimental α-factor measurement approaches reveal different carrier dynamical contributions, which require the corresponding definitions on a case-by-case basis.

Notice that the gain and refractive index changes considered in our model are from interband transitions in QDs, WL and barrier under the *quasi-equilibrium* condition. The calculated values are determined by the density of states, the inho-

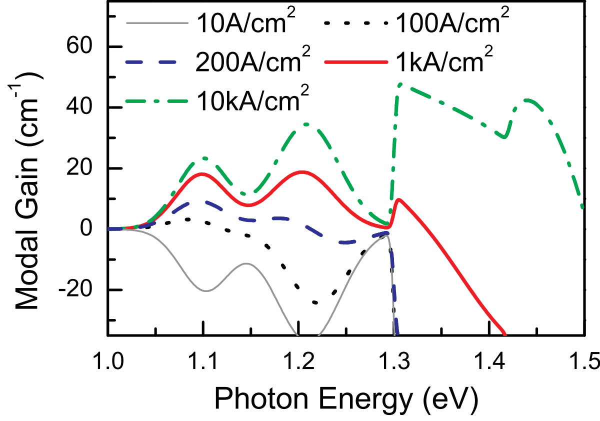

Figure 5.2: Modal gain spectra of QD SOAs for different current injection levels. The homogeneous broadening is described by a Gaussian lineshape. The spectral interval for each dot subgroup is $\gamma_H/10$.

mogeneous and homogeneous lineshape function and the carrier occupation. The plasma effects are neglected in our results.

The evaluation of the intensity modal gain is determined from the static solutions of corresponding carrier rate equations. The gain spectra for different current injections are shown in Figure 5.2. As the current density increases, the QD states are gradually filled with carriers and the corresponding gain maximum are reached. As the current density further increases, the carriers starts to fill up the reservoir states and provide extra gains at higher photon energies corresponding to the conventional spectral gain appearance of quantum well and bulk material.

The use of a Gaussian lineshape for homogeneous broadening requires Kramers-Kronig transform to retrieve the effective index change. In this case we choose $\gamma_H/10$ as the spectral interval for the QD subgroups to calculate the static solutions of the occupation factors for all the discrete states in QDs as well as the continuum states of the reservoir. Figure 5.3 shows the corresponding effective index change at a low current density. At this low current density, most of the effective index change is contributed from the interband transitions in the QD discrete states as well as the WL. We also calculated the corresponding contributions from different states. Here the corresponding carrier density variation is induced by a small change (1%) of the injection current density. The calculated linewidth enhancement factor around ω_G

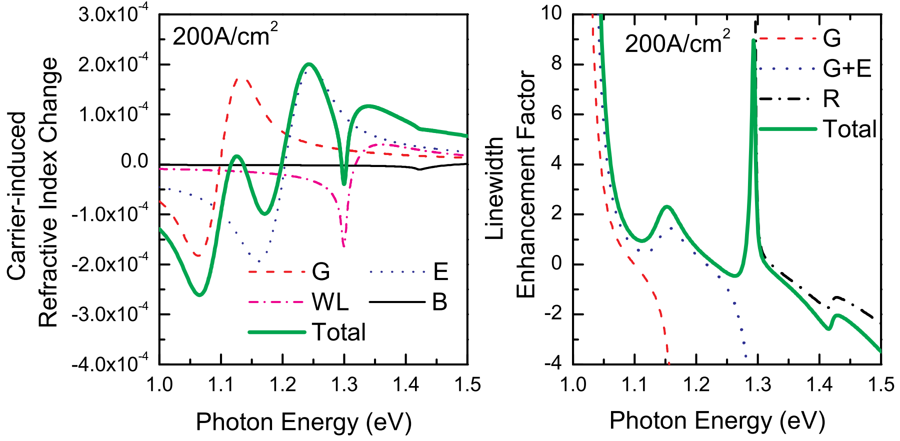

Figure 5.3: Calculated carrier-induced refractive index change (left) and corresponding linewidth enhancement factor (right) in QD SOAs as a function of the photon energy. Contributions from different transition states (E, G, R ≡ WL + B) are indicated. Current injection density is 200 A/cm^2. The homogeneous broadening is described by a Gaussian lineshape. The spectral interval for dot subgroup is $\gamma_H/10$. The variation of carrier density for evaluating the linewidth enhancement factor is induced by changing 1% of the injection current density.

is very small and close to zero, which is determined by the index change induced by ground states. However, the other index change contributions especially from excited states as well as WL, do play a role to alter the corresponding linewidth enhancement factor values. For the low current density situation, the linewidth enhancement factor can be still well approximated by the contributions only from discrete QD states.

As shown in Figure 5.4, the effective index change induced from the reservoir is enhanced significantly as we increase the current density to 1 kA/cm^2 or even higher 10 kA/cm^2. Therefore the large linewidth enhancement factor can not be simply approximated by the contributions from the discrete QD states only. In general, as the current density is strong enough to nearly fill up all the available QD states, the space for corresponding gain and refractive index change at QD states is limited by the finite QD density of states. Although the tails of the effective index change from the reservoir states are relatively small, it keeps increasing as there are far more density of states in reservoir to fill up. In this way, the linewidth enhancement

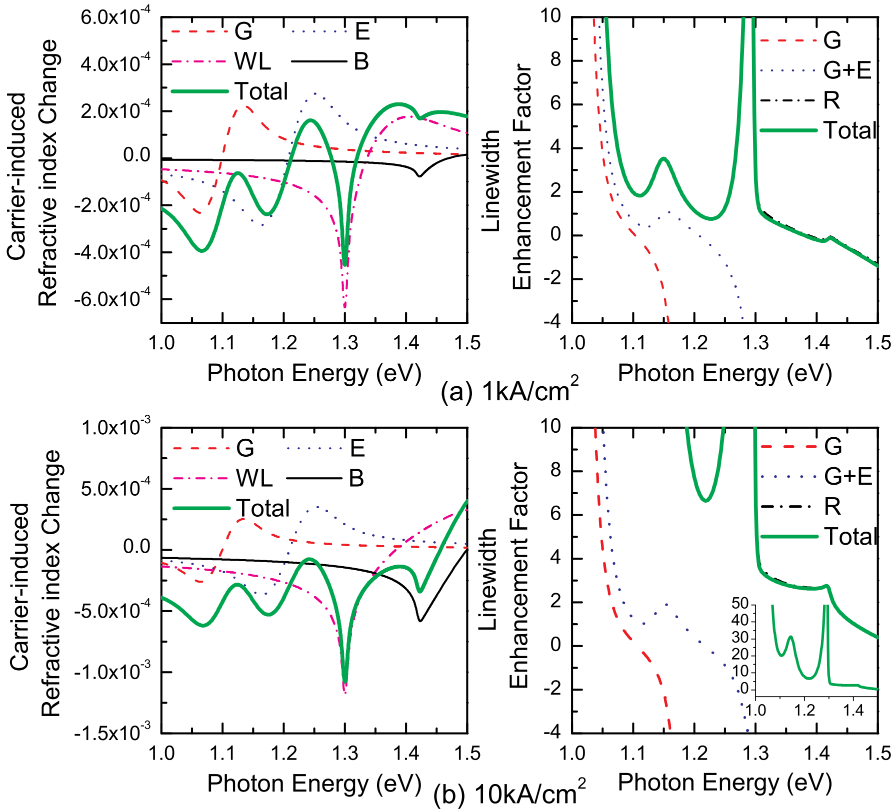

Figure 5.4: Calculated carrier-induced refractive index change and corresponding linewidth enhancement factor in QD SOAs as a function of the photon energy for two current injection densities of (a) 1 kA/cm^2 and 10 kA/cm^2. Contributions from different transition states (E, G, R ≡ WL + B) are indicated. The homogeneous broadening is described by a Gaussian lineshape. The spectral interval for dot subgroup is $\gamma_H/10$. The variation of carrier density for evaluation the linewidth enhancement factor is induced by changing 1% of the injection current density.

factor as a function of injection current density change depends heavily on how the reservoir is structured. This is similar to the discussion in [129] when the QD SOAs are at high current injection with maximal gain. There, the differential refractive index is dominated by the plasma effects while the contributions from the QDs are negligible and the contributions from reservoir are relatively low.

In Figure 5.5, the modal gain and corresponding linewidth enhancement factor

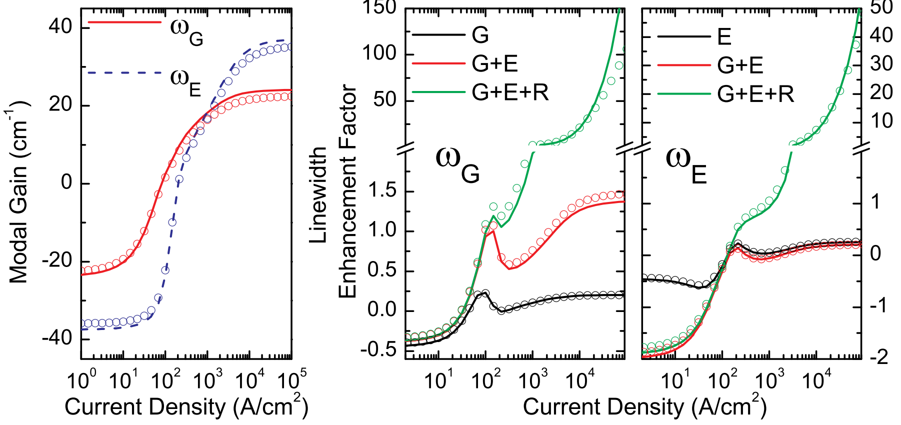

Figure 5.5: Modal gain and corresponding linewidth enhancement factor in QD SOAs as a function of the injection current density. The properties are calculated for ω_E and ω_G corresponding to the peak spectra gain of QD states E and G. Contributions from different transition states E,G and R are included. The solid lines are results based on Gaussian homogeneous lineshape. The circles are results based on Lorentzian homogeneous lineshape. The spectral interval for the dot subgroups is $\gamma_H/10$. The variation of carrier density for evaluation the linewidth enhancement factor is induced by changing 1% of the injection current density.

for ω_E and ω_G are calculated as a function of injection current density. The typical transparency current density is around 100 $\mathrm{A/cm^2}$. As the injection current density increases, the gains gradually reach their maximum values and the corresponding differential gains decrease. The linewidth enhancement factor estimated with different contributions can be significantly different from each other. If only considering the carrier-induced index change from ground states or excited states individually, the typical values of linewidth enhancement factor is ranging between -0.5 and 0.5. As the contribution from both QD states are considered, the α-factor at ω_G increases up to 1.5 in high current density regime. The α-factor for ω_E decreases down to -2 in low current density regime. This reflects the different impact of the asymmetric spectral effective index change. Qualitatively our results with contributions from QDs agree well with the calculations in [122]. As the contribution from the reservoir is added, the linewidth enhancement factor has a significant increase to tens or even higher. Instead of Gaussian linshape, the usage of Lorentzian lineshape for homo-

geneous broadening function leads to similar results. In this case, the properties are determined by how the carriers fill up the available states (sequentially from G, E, WL to B) in QD SOAs. At the high current density, the α-factor at ω_G is higher than the one at ω_E because the ground state levels are more completely occupied than the excited states.

The discussion in this section indicates the possibility to estimate the refractive index dynamics (phase dynamics) with our QDs carrier dynamics model presented in this thesis. However, extra efforts are still needed to quantify our present understanding, i.e., inclusion of the plasma effects, calculation of a more detailed/realistic QD band structure and implementation of a universal numerical scheme for Kramers-Kronig transform. More fundamentally, we need to understand the dominating carrier dynamical contributions behind different experimental approaches, instead of blindly implementing the conventional α-factor definition without justifications. In the rest of the thesis, our discussion is limited to gain dynamics with the assumption of zero linewidth enhancement factor.

5.2 CW Gain Saturation

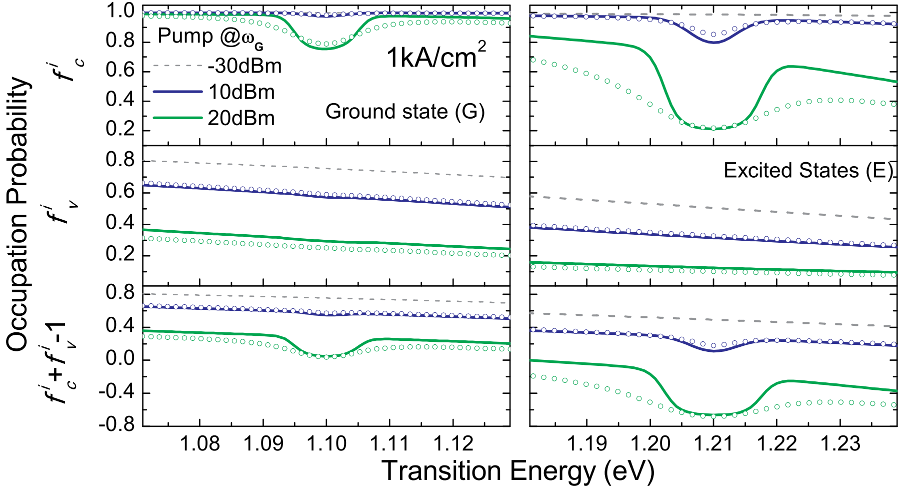

Figure 5.6: Carrier occupation factors corresponding to the ground states (left) and excited state (right) in response to CW pump @ω_G at a low injection current density (1 kA/cm^2) for different homogeneous lineshapes. The solid lines are results based on Gaussian homogeneous lineshape. The circles are results based on Lorentzian homogeneous lineshape. The FWHM values of homogeneous broadening are fixed. The spectral interval for dot subgroup is $\gamma_H/10$.

In this section we will discuss the CW gain saturation properties of QD SOAs without propagation effects. In general, as we increase the CW pump power, carriers in the corresponding dot subgroups will be depleted based on the magnitude of stimulated emission determined by homogenous broadening lineshape.

Figure 5.6 illustrates the case with pump @ω_G at low current density 1 kA/cm^2. In the unsaturated regime at this current density, the QD states in the conduction band are close to being completely filled, while the corresponding valence band states are partly filled due to the large effective hole mass. As the pump power @ω_G increases, the carriers in the ground states of the dot subgroups within the homogeneous broadening range are depleted due to stimulated emission as shown in Figure 5.6(left). Spectral holes, in particular in the conduction band, are developed due to the relatively slow electron scattering rates to refill the carrier depletion induced by the stimulated emission. Spectral holes for the valance band are barely

visible, because the valence band intradot relaxations are still strong enough to keep the valence band distribution close to the quasi-equilibrium situation with a reduced common Fermi energy. As a consequence, the ground state population inversion factors of all QD subgroups have a corresponding reduction contributed from valence band. The appearance of the calculated spectral holes strongly depends on the choice of homogenous lineshapes even with the same FWHM value. The use of Lorentzian lineshape, which has very slow decaying tail, leads to carrier depletions in QD subgroups over a much wider spectral range than the ones with Gaussian lineshape.

Moreover, an important signature of the unique QDs carrier dynamics between discrete states is the *satellite* spectral holes with transition energy corresponding to the higher QD discrete states as show in Figure 5.6(right). The conventional bulk semiconductor material which has a continuum of states, allows fast carrier-carrier scattering within the continuum band for carriers to reach the quasi-equilibrium distribution. In comparison, for spatially separated self-assembled QDs such direct carrier-carrier scattering between spectrally adjacent dot subgroup is greatly decreased. Instead, the carriers in each QDs are balanced via the common continuum reservoir states through intradot carrier capture/relaxations in between different levels at different rates. Here, the electron refilling of the ground states have been assumed dominated by the fast carrier scattering from the excited states of the same dot (subgroup), while the refilling of the excited states from the reservoir is considerably slower. Thus the depletion of electrons at the ground states imprint a correlated spectral hole at the excited states of the same dot subgroups, which is synonymous to the existence of an injection bottleneck due to long capture time or short escape time [130]. The hole dynamics approximated by the simple continuum-type model keeps the quasi-equilibrium appearance.

Figure 5.7(left) shows the calculated modal gain in the presence of a CW pump beam @ω_G at low current density (1 kA/cm^2). The difference of choosing Gaussian or Lorentzian homogeneous lineshape (with the same FWHM value) has been illustrated. In the unsaturated regime, the modal gain for the pump beam based on Lorentzian lineshape is comparably smaller than the Gaussian lineshape. As the pump power increases, both of them have similar saturation tendency with a saturation power around 10 dBm.

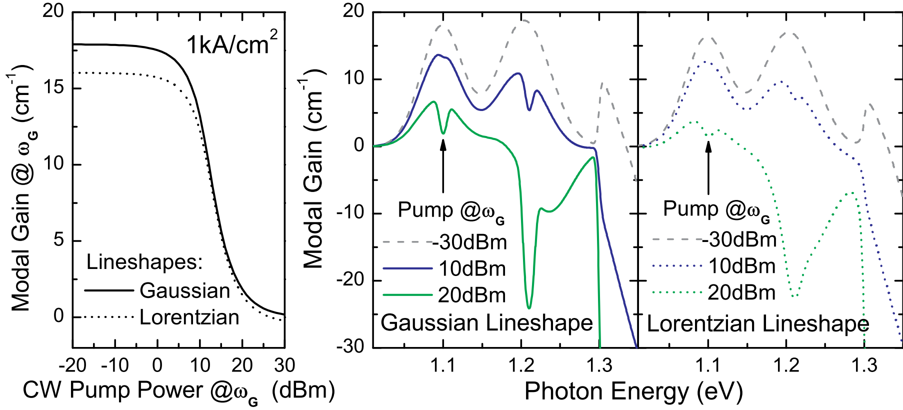

Figure 5.7: Gain saturation in response to the CW pump @ω_G at a low injection current density (1 kA/cm^2) for different lineshapes. (left) Saturation of the intensity modal gain corresponding to the optical pump. (right) The corresponding spectral gain with Gaussian or Lorentzian lineshapes for homogeneous broadening function. The FWHM values of homogeneous broadening are fixed to $2\gamma_H$. The spectral interval for dot subgroup is $\gamma_H/10$.

Meanwhile, we use another weak optical CW beam to probe the spectral gain with the assumption of no wave mixing between the two beams, the change of occupation probabilities also leads to a spectral gain change for the probe beam as shown in Figure 5.7(right). Additional to the spectral hole corresponding to the ground states transition, an extra spectral hole corresponding to the excited states transition of the same dot subgroups is developed. The spectral gain with Gaussian lineshape develops a narrow spectral hole. The spectral hole estimated with Lorentzian lineshape is much more smeared-out. Moreover, in the presence of a strong pump beam (20 dBm), severe depletion of total carrier density in the conduction and valence band leads to the significant drop of the overall spectral gain and dominates the gain saturation mechanism.

As suggested by different literatures [30, 31, 131], the use of a stronger current density will improve the gain saturation performance regarding the saturation power. We calculate the case in the presence of the CW pump beam @ω_G at a higher current density of 10 kA/cm^2 as shown in Figure 5.8. In the unsaturated regime at this current density, the occupation probabilities in the valence band for

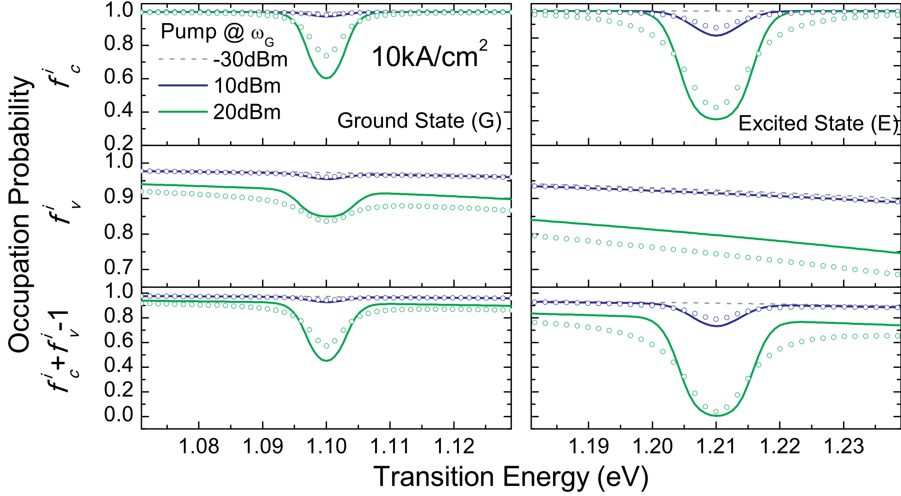

Figure 5.8: Carrier occupation factor corresponding to the ground states (left) and excited state (right) in response to the CW pump @ω_G at a high injection current density (10 kA/cm^2) for different lineshapes. The solid lines are results based on Gaussian homogeneous lineshape. The circles are results based on loretzian homogeneous lineshape. The FWHM values of homogeneous broadening are fixed. The spectral interval for dot subgroup is $\gamma_H/10$.

all the dot subgroups are improved and the population inversion factors are much closer to 1. In comparison to the situation with 1 kA/cm^2, when the pump power increases, the decrease of the overall occupation probabilities in both conduction and valence band for all the dot subgroups is limited. It is simply due to the fact that more current injected carriers are available in the reservoir to refill the QD states and the depletion of total carrier density is greatly relieved. In this way, the stimulated emissions result in clearer spectral holes of population inversion factors. Here, electron recovery of the ground and excited states (electron intra-dot relaxations) in each QDs determines the spectral hole appearance. It is also easier to interpret the power-broadened FWHM of the spectral hole based on simple expressions similar to Eq. (3.34).

Figure 5.9 shows the corresponding modal gain for the case with 10 kA/cm^2. The unsaturated modal gain is increased as the population inversion factor is closer to 1. The saturation power has been increased to around 20 dBm. As the modal gain for

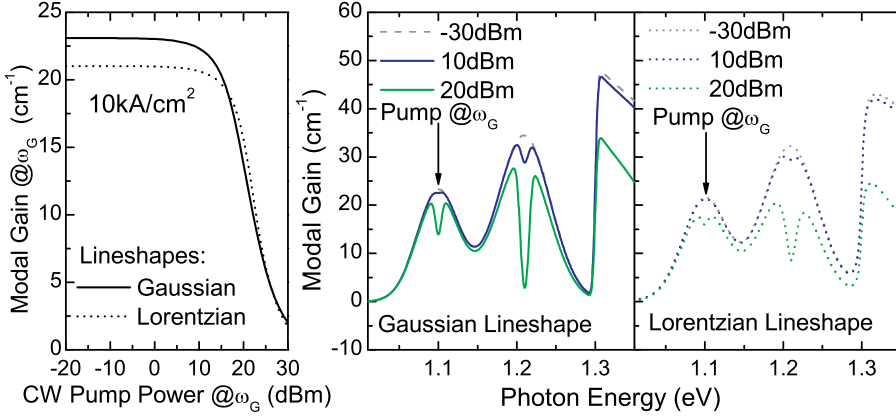

Figure 5.9: Gain saturation in response to the CW pump @ω_G at a high injection current density (10 kA/cm^2) for different lineshapes. (left) Saturation of the modal gain corresponding to the optical pump. (right) The corresponding spectral gain with Gaussian or Lorentzian lineshapes for homogeneous broadening function. The FWHM values of homogeneous broadening are fixed. The spectral interval for dot subgroup is $\gamma_H/10$.

the pump beam based on Lorentzian lineshape involves inversion contributions from more dot subgroups, it has a slightly higher saturation power than the Gaussian lineshape. At such high current density, the spectral gain is more featured with spectral hole burning rather than the overall decline of spectral gain levels.

Figure 5.10 shows the calculated modal gain and saturation power corresponding to the CW pump @ω_G and @ω_E as a function of the current density based on Gaussian homogenous lineshape. As the injection current density increases, the saturation power increases and gradually reaches its maximum around 20dBm [1]. This maximum saturation power for pump @ω_G is higher than that for pump @ω_E due to the fact that ground state is assumed to have an ultrafast carrier relaxation contribution from excited states.

[1]Notice that the high saturation powers are also obtained in the low-confinement bulk or QW SOAs [132]. Quantum dots inherently benefit from the low confinement regarding high saturation power.

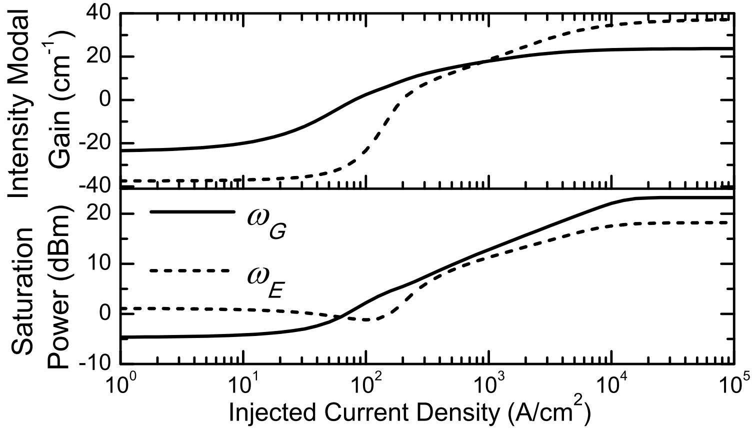

Figure 5.10: Modal gain and saturation power corresponding to the CW pump @ω_E and ω_G as a function of the injection current density. Gaussian homogeneous broadening lineshape is used. The spectral interval for dot subgroup is $\gamma_H/10$.

5.3 Small-Signal Harmonic Medium Responses

This section describes the harmonic analysis for QD SOAs without propagation effects. The principle is based on the harmonic analysis described in section 3.4. Calculations are based on the detailed derivations found in Appendix B.2. This investigation is inspired by a similar work in a 2-level QD-WL system [133].

For a weakly harmonically modulated signal with optical frequency of ω_p and modulation frequency Ω, we have:

$$P_p(t) = P_{pump} + (\Delta P e^{-i\Omega t} + c.c.)/2 \tag{5.5}$$

where P_{pump} is the power of optical carrier as a pump, ΔP is the corresponding perturbation. We assume that the modulated occupation probabilities $f_\alpha^i(t)$ of the corresponding states in a QD subgroup, with $(\alpha = c, v)$ for conduction and valence band, have the form:

$$f_\alpha^i(t) = f_{\alpha 0}^i + (\Delta f_\alpha^i e^{-i\Omega t} + c.c.)/2, \qquad (\alpha = c, v) \tag{5.6}$$

here $f_{\alpha 0}^i$ is the static part of the occupation probabilities and Δf_α^i is the harmonic terms of the corresponding occupation probabilities.

By substituting Eq. (5.5) and (5.6) into (4.23) and only keeping the first-order perturbation terms, the propagation equation for the modulation envelope can be derived:

$$\begin{cases} \partial_z P_{pump} = (g_{incoh} - \alpha_{int}) P_{pump}, \\ \partial_z \Delta P = (g_{incoh} - \alpha_{int}) \Delta P + g_{coh} \Delta P \end{cases} \tag{5.7}$$

Here we have introduced:

$$\begin{aligned} g_{incoh} &= \frac{\varepsilon_X D_D n_l \sigma_D}{H_{mod}} \sum_i \left[Q_X^{p,i} \left(f_{c0}^i + f_{v0}^i - 1 \right) \right], \\ g_{coh} &= \frac{\varepsilon_X D_D n_l \sigma_D}{H_{mod}} \sum_i \left[Q_X^{p,i} \left(\Delta f_c^i + \Delta f_v^i \right) \eta_p \right] \end{aligned} \tag{5.8}$$

where the term $\left(f_{c0}^i + f_{v0}^i - 1\right)$ is the static population inversion factor contributing to the incoherent gain g_{incoh}. The second term $\left(\Delta f_c^i + \Delta f_v^i\right)\eta_p$ is effective coherent population probabilities contributing to the coherent gain g_{coh}. The coherent gain is also referred to as the slowly varying envelope of dynamic gain grating. $\eta_p = \frac{P_{pump}}{\Delta P}$

is the power ratio of DC and AC part denoting the corresponding normalization factor.

The static population inversion factor as well as the corresponding incoherent spectral gain are same to quantities discussed in the previous section regarding CW gain saturation. In the following sections, we will mainly discuss the coherent contributions. Here we only focus on the Gaussian homogenous broadening lineshape. In terms of the modulation frequency, we start with a low modulation frequency $\Omega/2\pi$=1 MHz, which is much lower than the inverse of carrier lifetime. Then we extended the discussion to a broad modulation frequency range. The spectral interval for dot subgroup is $\gamma_H/10$.

5.3.1 Oscillations of carrier populations at a low modulation frequency

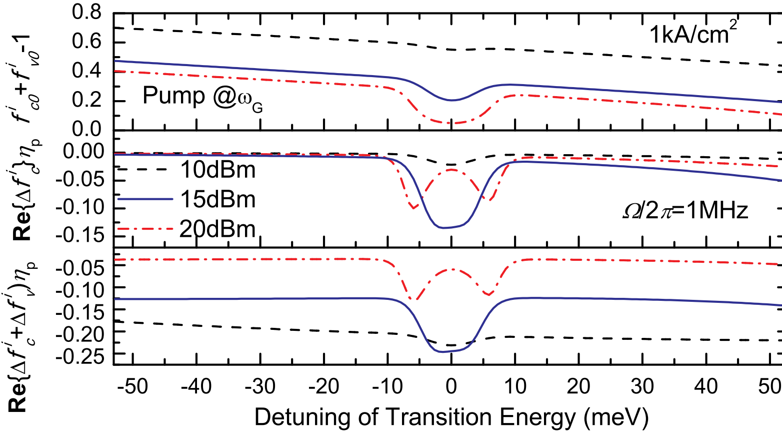

Figure 5.11: Spectral distribution for ground state incoherent and coherent population properbilities of the inhomogeneously broadened dots (subgroups) in the presence of different pump powers @ω_G. The detuning of transition energy is relative to $\hbar\omega_G$. Injection current is 1 kA/cm^2. The results are calculated at low modulation frequency limit $\Omega/2\pi$=1 MHz. η_p is the normalization factor. Gaussian homogeneous broadening lineshape is used. The spectral interval for dot subgroup is $\gamma_H/10$.

An example of the calculated population probabilities of different dot subgroups in the presence of different pump power @ω_G is shown in Figure 5.11. The results are

calculated at a low modulation frequency $\Omega/2\pi$=1 MHz. The incoherent occupation probabilities are shown for reference. For the given current injection, the variation of population probabilities with frequency detuning relative to the photon energy of the pump is similar to the discussion related to Eq. (3.36) in the two-level system. As the pump power increases, the spectral hole appearance of $\mathbf{Re}\{\Delta f_c^i + \Delta f_v^i\}\eta_p$ is power broadened. As the pump power is further increased to deplete the carriers, the maximum magnitude starts to shift to the dot subgroups with non-zero frequency detuning. Different from the two-level system results shown in Figure 3.8, the quantum dots have complex responses with different carrier dynamical contributions from both the conduction and valence band. For the given current density, the spectral hole feature is contributed mostly by the conduction band contribution, while the quasi-equilibrium feature with a common Fermi energy perturbation is mostly from the valence band.

5.3.2 Oscillations of carrier populations over a broad modulation frequency range

The oscillations of QDs carrier populations as a function of the modulation frequency show rich details induced by the carrier dynamical processes. In order to facilitate the understanding of the application results in Chapter 7, we choose three different current densities to illustrate the carrier oscillation in the absorption regime (1 A/cm^2), gain regime with low saturation power (1 kA/cm^2) and gain regime with high saturation power (10 kA/cm^2). We calculate the real and imaginary parts of coherent carrier oscillations including the conduction and valence band contributions in the presence of a 10 dBm pump power @ω_G. What has been shown in Figure 5.12 are the ground state carrier oscillations in the dot subgroup with ground state transition energy equal to $\hbar\omega_G$.

In principle, at the low modulation frequencies, the imaginary parts of coherent population occupations are approaching to zero. As modulation frequencies increases, the imaginary parts peak at several characteristic modulation frequencies determined by the corresponding dominating carrier dynamical processes. The real parts have their maximum magnitudes at the low frequency limit, which are positive in the absorption regime and negative in the gain regime, indicating whether the carrier oscillations are *in phase* or *in antiphase* with the intensity modulated signal.

As the modulation frequency increases, the real parts gradually decrease to zero. The non-zero imaginary parts give rise to the changes of relative phases between the carrier oscillations and intensity modulated signals.

For the hole dynamics, it is relative simple to distinguish the characteristic modulation frequencies determined by the total carrier density pulsation peaked around Ω_1 at the scale of hundreds of MHz and the intradot valence band relaxation (100 fs) peaked around $\Omega_3 = 10/2\pi$ THz. Depending on the details of the electron dynamical processes, the intermediate characteristic modulation frequencies Ω_2 are between 10-100 GHz. At high current density, the electrons also have a characteristic modulation frequency close to Ω_3 which is determined by the ultrafast carrier relaxation between the ground and excited states. As the effective mass, band structures and dynamical contributions for electrons and holes are different from each other, the corresponding electron and hole responses are not necessary *in phase* with each other. The dominating dynamical processes are determined by the relative magnitude ratio between electron and hole responses.

Figure 5.12(a) shows that electron responses make a large contribution to the overall responses in the absorption regime. Notice that the saturation power in the absorption regime is far below 10 dBm. Here, the fast electron responses around 10 GHz are mainly induced by the upward electron transitions in the deep saturation regime. In the gain regime with low saturation power as shown in Figure 5.12(b), the hole responses at low frequencies dominate the overall appearance. As the injection current increases as seen in Figure 5.12(c), the electron responses are enhanced and surpass the hole responses. Hereby, the dominating total carrier density pulsation can be relieved. And the fast electron responses are determined by the downward electron transitions.

We also calculate similar results in the presence of a 10dBm pump power $@\omega_E$. Figure 5.13 shows the calculated results of the excited state carrier oscillations for the dot subgroup resonant with ω_E. In this case, we can observe similar qualitative behaviors as the ones of the ground states. In comparison with the ones of the ground states, the electron responses of the excited states make a larger contribution to the overall responses, especially for the modulation frequencies between 10-100 GHz. The missing of ultrafast responses around THz range corresponds to the fact that the ultrafast carrier relaxation between the ground and excited states

have limited impact to the electron recovery at excited states. It is clear that the details of the band structure, pump power intensity, carrier dynamical processes will significantly modify the quantitative appearance of the results.

Additional to the image of carrier oscillations in an individual dot (subgroup), our model also allows us to have a deeper view of the carrier oscillations in the inhomogeneously broadened QDs (dot subgroups). Here we show a set of examples of the electron occupation factors in the inhomogeneously broadened dot subgroups as a function of modulation frequency, in particular, when the pump power increases and drives the QDs into the deep saturation regime. We choose the situation in the gain regime with low saturation power 1 kA/cm^2. The pump frequency is set at ω_G. The modulation frequency is varying from 1 MHz to 10 THz.

Figure 5.14 shows the three-dimensional plot of the real and imaginary part of electron occupation factors as a function of transition energy and modulation frequency for 10 dBm pump power. Most of the variations are centered around the pump frequency ω_G within the homogeneous broadening range, where the carrier oscillations are directly induced by stimulated emission. The imaginary parts peak at the modulation frequencies around 100 GHz, also indicated in Figure 5.12(b). Due to no direct electron transfer between adjacent dot subgroups, the electrons in the dot subgroups outside of homogeneous broadening range are barely oscillated. The only exceptions are the variations at low modulation frequencies around 100 MHz, which are induced from total carrier density pulsation in the reservoir. Following the discussion of carrier oscillations at the low modulation frequency in previous section, the spectral appearance changes a lot as the pump power increases.

Figure 5.15 and 5.16 show the calculated results for 15dBm and 20dBm pump power, respectively. The variations of occupation factors regarding the transition energy tend to be broadened and then split. Such changes take place for a broad modulation frequency range up to 100 GHz or even higher. The summation of all these microscopic occupation factors contribute to the gain described by Eq. (5.8).

It is clear that a proper spectral interval is required to model the influence of the inhomogeneous and homogeneous broadening. As a consequence, it also indicates the possible problem of calculation accuracy in gain dynamics by choosing a coarse spectral interval for QD subgroups, e.g., 6.6 meV used in our time-domain calculation. This question arises immediately after the recently implementation

of harmonic-analysis code. There is much more work to be done concerning this issues. Fortunately, our preliminary calculations indicate that the quantitatively difference is still reasonable. The qualitative behaviors especially concerning the phase properties discussed in the later parts of the thesis are fairly close to the ones with a fine spectral interval.

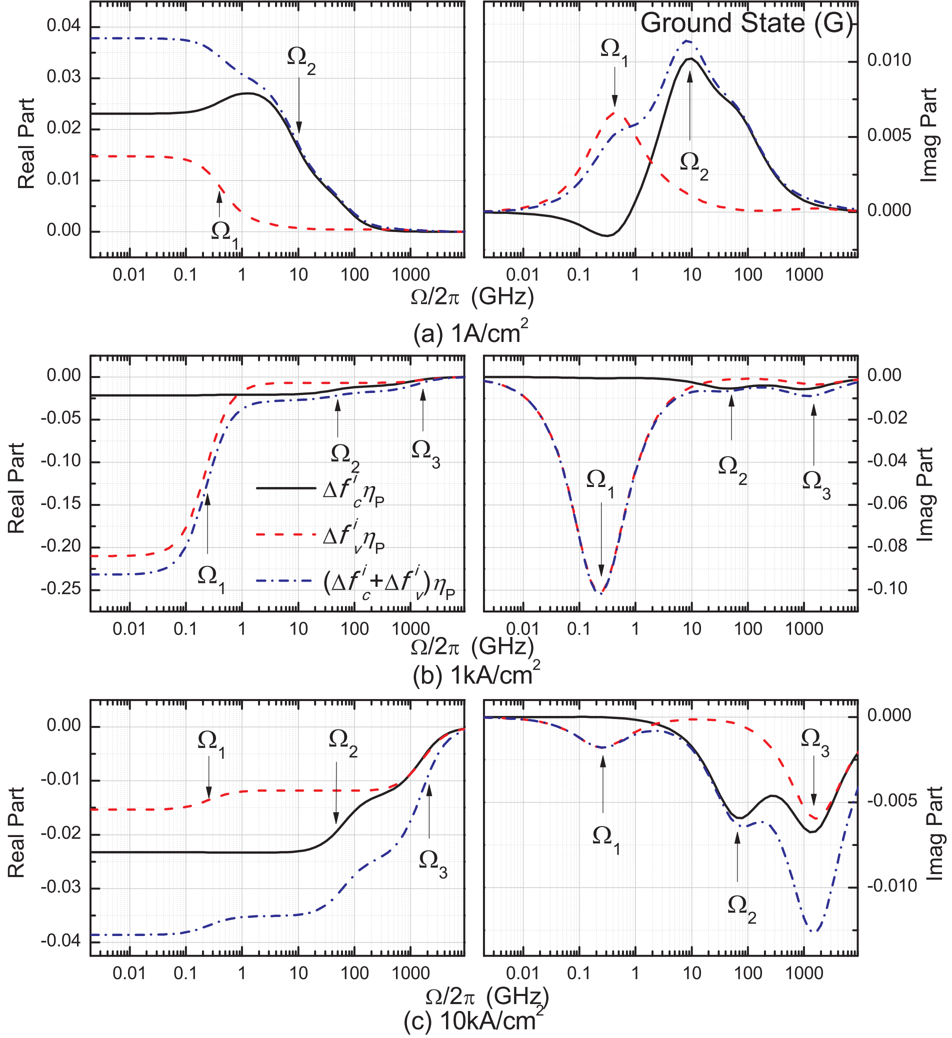

Figure 5.12: Occupation factors for dot subgroup resonant with ω_G as a function of modulation frequency Ω. The pump power @ω_G is 10 dBm. Three current densities (a) 1 A/cm^2, (b) 1 kA/cm^2 and (c) 10 kA/cm^2 are investigated. The contributions from electron Δf_c^i and holes Δf_v^i are indicated. η_p is the normalization factor. Ω_1, Ω_2 and Ω_3 are three characteristic modulation frequencies. The spectral interval for dot subgroup is $\gamma_H/10$.

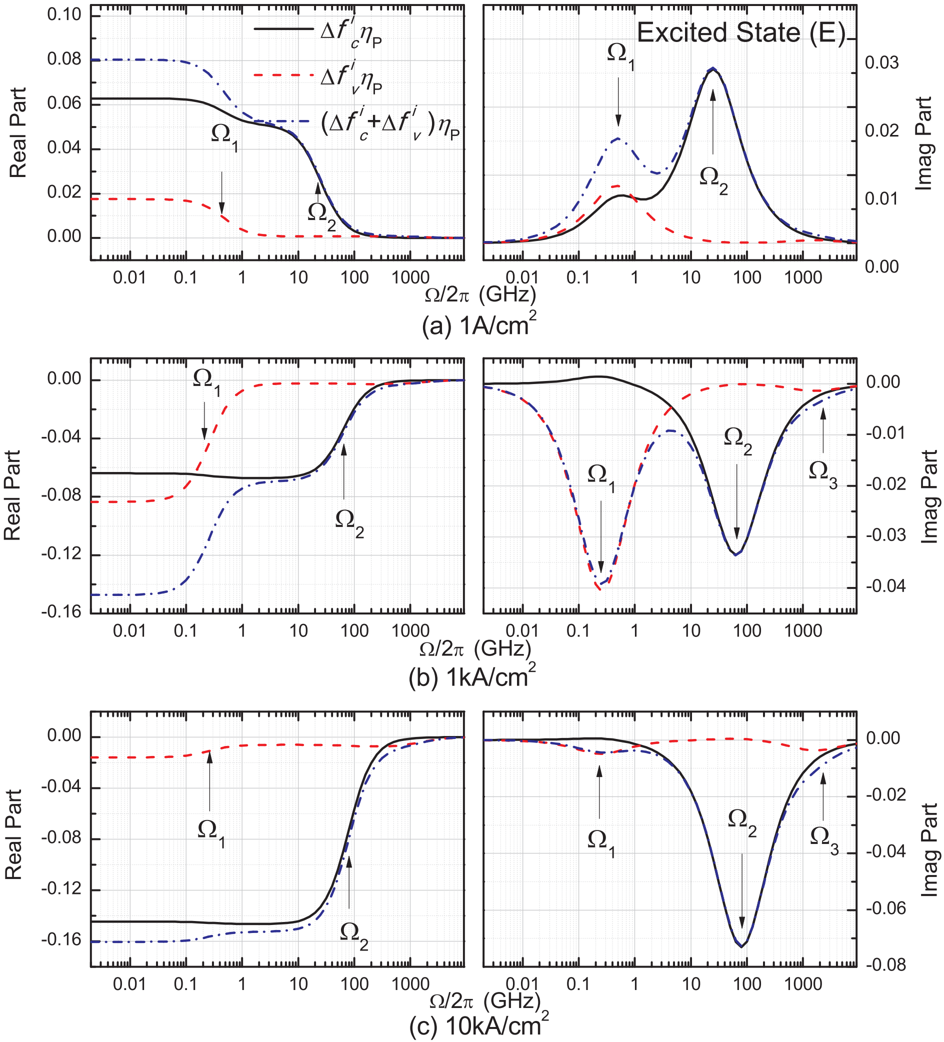

Figure 5.13: Occupation factors for dot subgroup resonant with ω_E as a function of modulation frequency Ω. The pump power @ω_E is 10 dBm. Three current densities (a) 1 A/cm^2, (b) 1 kA/cm^2 and (c) 10 kA/cm^2 are investigated. The contributions from electron Δf_c^i and holes Δf_v^i are indicated. η_p is the normalization factor. Ω_1, Ω_2 and Ω_3 are three characteristic modulation frequencies. The spectral interval for dot subgroup is $\gamma_H/10$.

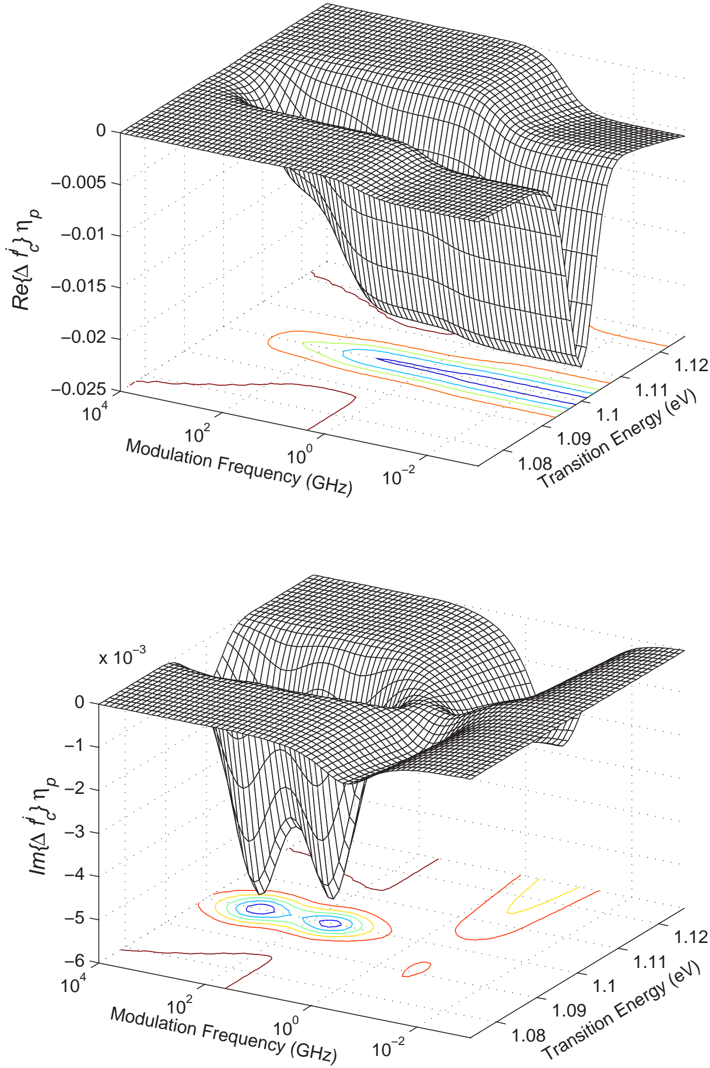

Figure 5.14: Variation of ground state electron coherent populations occupations Δf_c^i of the inhomogeneously broadened dots (subgroups) as a function of modulation frequency and transition energy in the presence of 10 dBm pump power @ω_G. Injection current is 1 kA/cm^2. The real (upper) and imaginary (lower) part of $\Delta f_c^i \eta_p$ are calculated for modulation range from 1 MHz to 10 THz. Gaussian homogeneous broadening lineshape is used. The spectral interval for dot subgroup is $\gamma_H/10$.

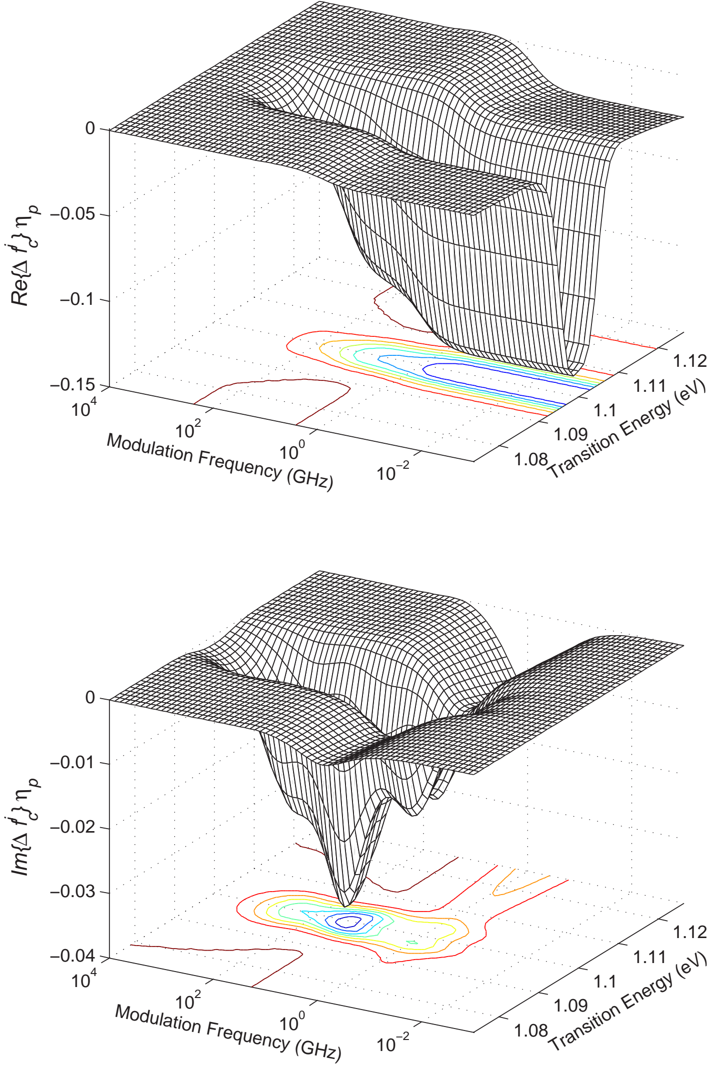

Figure 5.15: Variation of ground state electron coherent populations occupations Δf_c^i of the inhomogeneously broadened dots (subgroups) as a function of modulation frequency and transition energy in the presence of 15 dBm pump power $@\omega_G$. Injection current is 1 kA/cm^2. The real (upper) and imaginary (lower) part of $\Delta f_c^i \eta_p$ are calculated for modulation range from 1 MHz to 10 THz. Gaussian homogeneous broadening lineshape is used. The spectral interval for dot subgroup is $\gamma_H/10$.

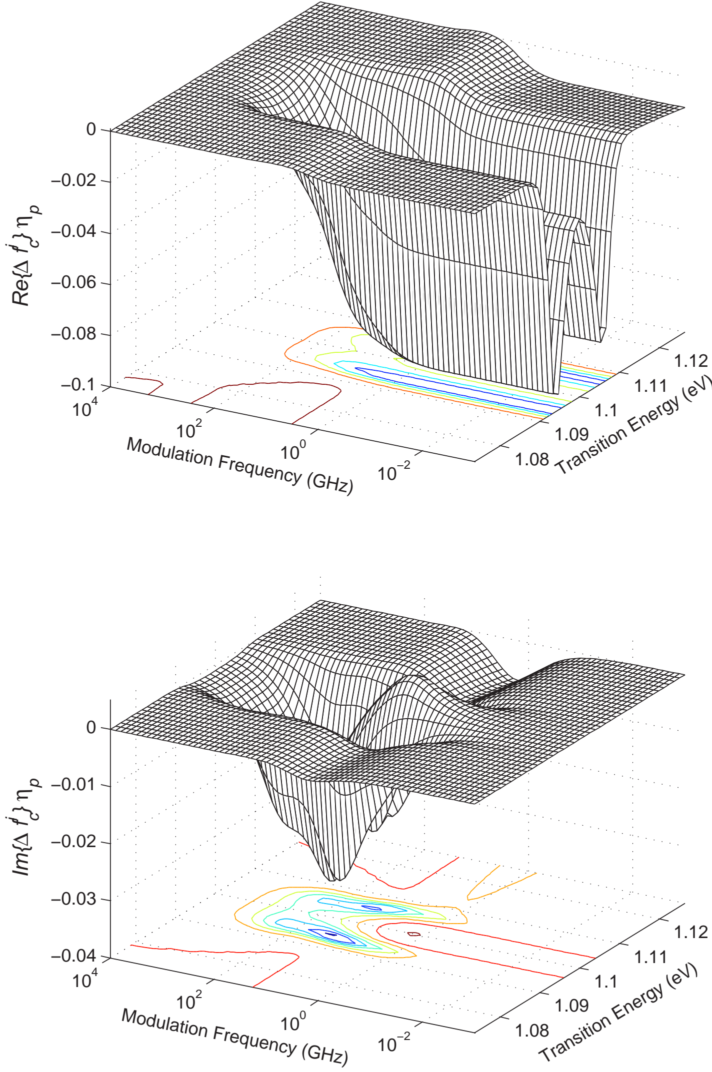

Figure 5.16: Variation of ground state electron coherent populations occupations Δf_c^i of the inhomogeneously broadened dots (subgroups) as a function of modulation frequency and transition energy in the presence of 20 dBm pump power @ω_G. Injection current is 1 kA/cm^2. The real (upper) and imaginary (lower) part of $\Delta f_c^i \eta_p$ are calculated for modulation range from 1MHz to 10THz. Gaussian homogeneous broadening lineshape is used. The spectral interval for dot subgroup is $\gamma_H/10$.

5.3.3 Oscillations of gain at a low modulation frequency

After the simulation of the microscopic occupation factors of all the dot subgroups, it is straightforward to calculate the coherent gain g_{coh} based on Eq. (5.8). At a low modulation frequency 1 MHz, we can evaluate the magnitude of coherent gain as a function of pump power, which is similar to the discussion in [133]. We define the modulation response (in units of cm^{-1}/W) as the magnitude of coherent gain divided by the pump power. The gain contributions from electron and hole are separated to identify whether the slow hole dynamics (total carrier density pulsation) dominates.

Figure 5.17 shows the ground state coherent gains and corresponding modulation responses as a function of pump power at ω_G for three different current densities. In general, when the pump power increases, the coherent gains first increase, peak around the saturation power and then decrease. It indicates that the maximum coherent gain takes place when the modal gain/absorption is nearly bleached by half. The electron and hole gain contributions peak at different pump powers as the corresponding saturation mechanisms are different. The modulation responses provide another kind of measurements which have been widely used for semiconductor lasers [98]. At the low pump power (in the the unsaturated situation), the modulation responses is a constant. As the pump power increases, this unsaturated modulation responses will be changed by the stimulated emission/absorption and decrease to zero at high pump power limit. Two types of modulation responses as a function of pump power are observed. One is a monotonically decreasing curve and another has an extra resonant-type increase. The exact physical origins (dynamical contributions) are not clear but might be analyzed in the future by the decomposition method used in [133]. In the absorption regime (1 A/cm^2), the coherent gains are dominated by the electron contributions peaked around -5 dBm. In the gain regime with low saturation power (1 kA/cm^2), the coherent gains are dominated by the hole contributions peaked around 10 dBm. By increasing the current density, the hole contributions have been surpassed by the electron contributions.

Meanwhile, we also calculate the excited state coherent gains as a function of pump power at ω_E in the same conditions as shown in Figure 5.18. The excited state coherent gains show the similar behaviors as the ones of ground states. Two differences need to be highlighted. Firstly, the portion of the electron contributions

to the excited state coherent gain is larger especially in the gain regime, where the slow hole dynamics are greatly suppressed. Secondly, the excited state coherent gains peak at a relatively low pump power (as the saturation powers of excited states are lower). These features make the excited states (the relatively slow recovered upper states) more attractive to realistic applications.

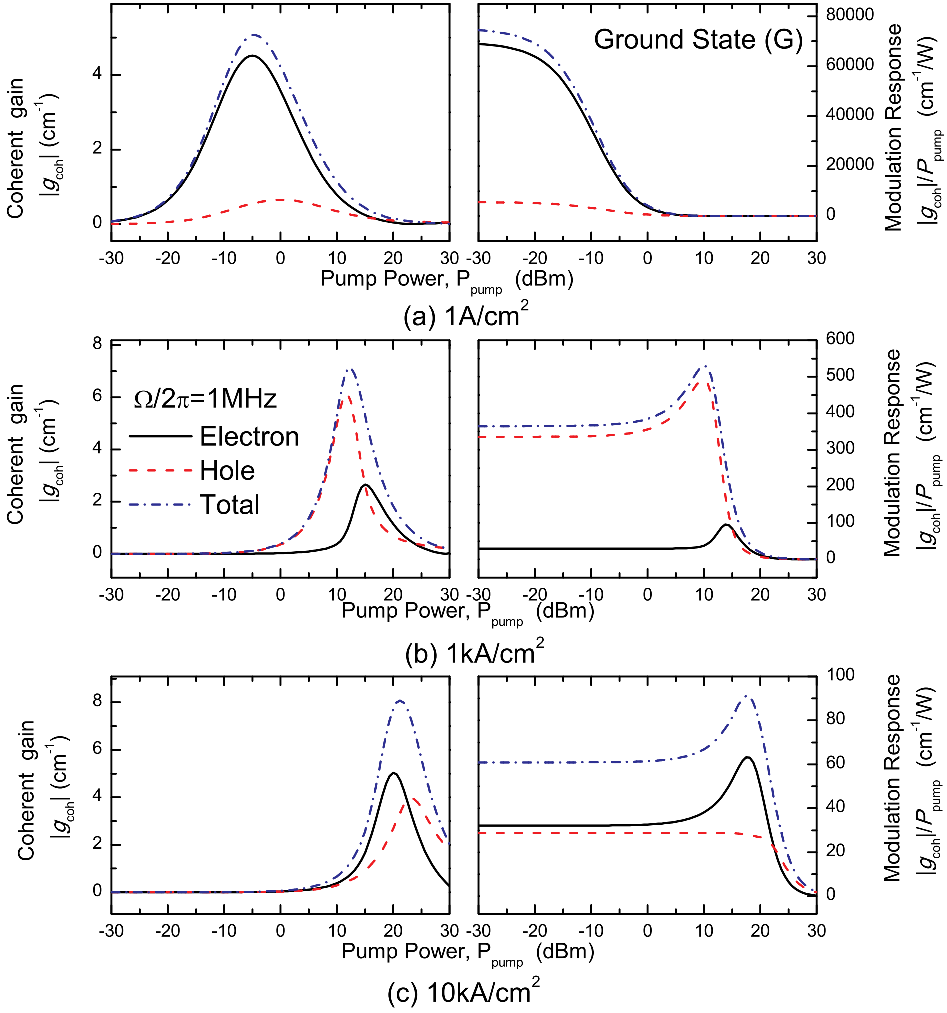

Figure 5.17: Magnitude of the coherent gain $|g_{coh}|$ and modulation response $|g_{coh}|/P_{pump}$ as a function of pump power @ω_G corresponding to QD ground states. Three different current density (a) 1 A/cm^2, (b) 1 kA/cm^2 and (c) 10 kA/cm^2 are considered. The results are at a low modulation frequency $\Omega/2\pi$=1 MHz. Gaussian homogeneous broadening lineshape is used. The spectral interval for dot subgroup is $\gamma_H/10$.

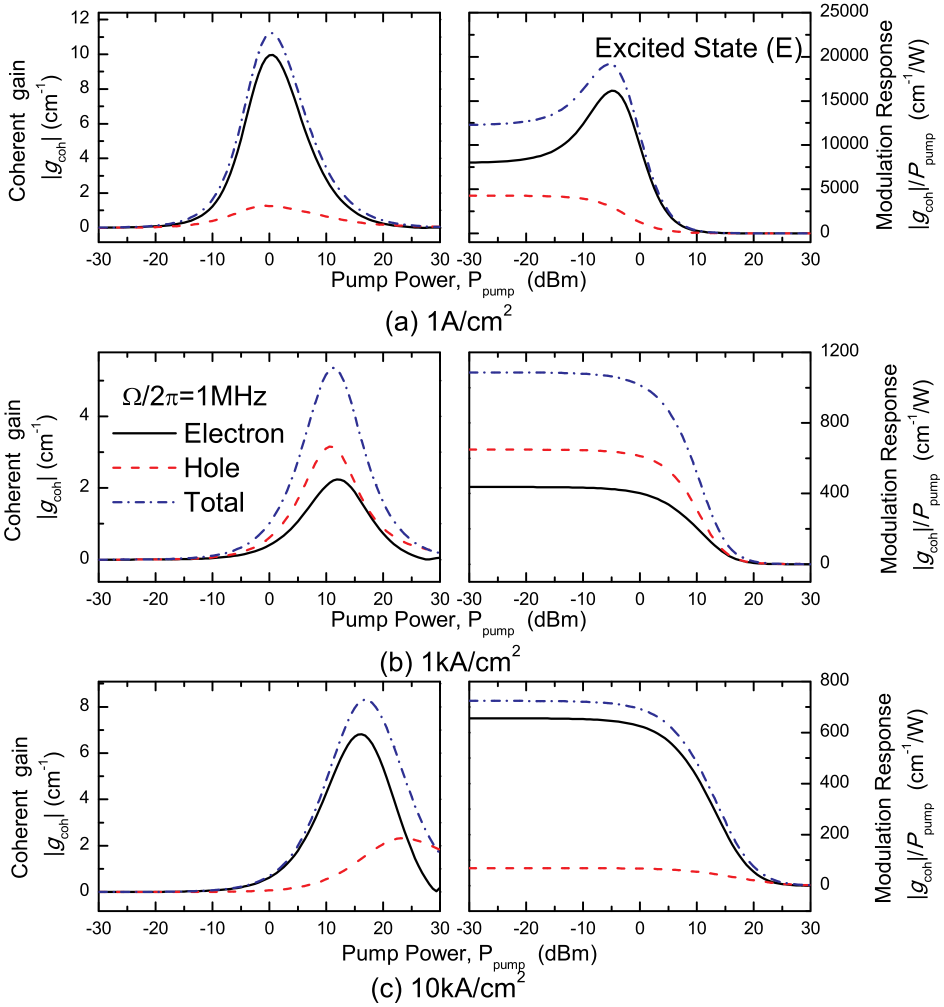

Figure 5.18: Magnitude of the coherent gain $|g_{coh}|$ and modulation response $|g_{coh}|/P_{pump}$ as a function of pump power @ω_E corresponding to QD excited states. Three different current densities (a) 1 A/cm^2, (b) 1 kA/cm^2 and (c) 10 kA/cm^2 are considered. The results are shown for a low modulation frequency $\Omega/2\pi$=1 MHz. Gaussian homogeneous broadening lineshape is used. The spectral interval for dot subgroup is $\gamma_H/10$.

5.3.4 Oscillations of gain over a broad modulation frequency range

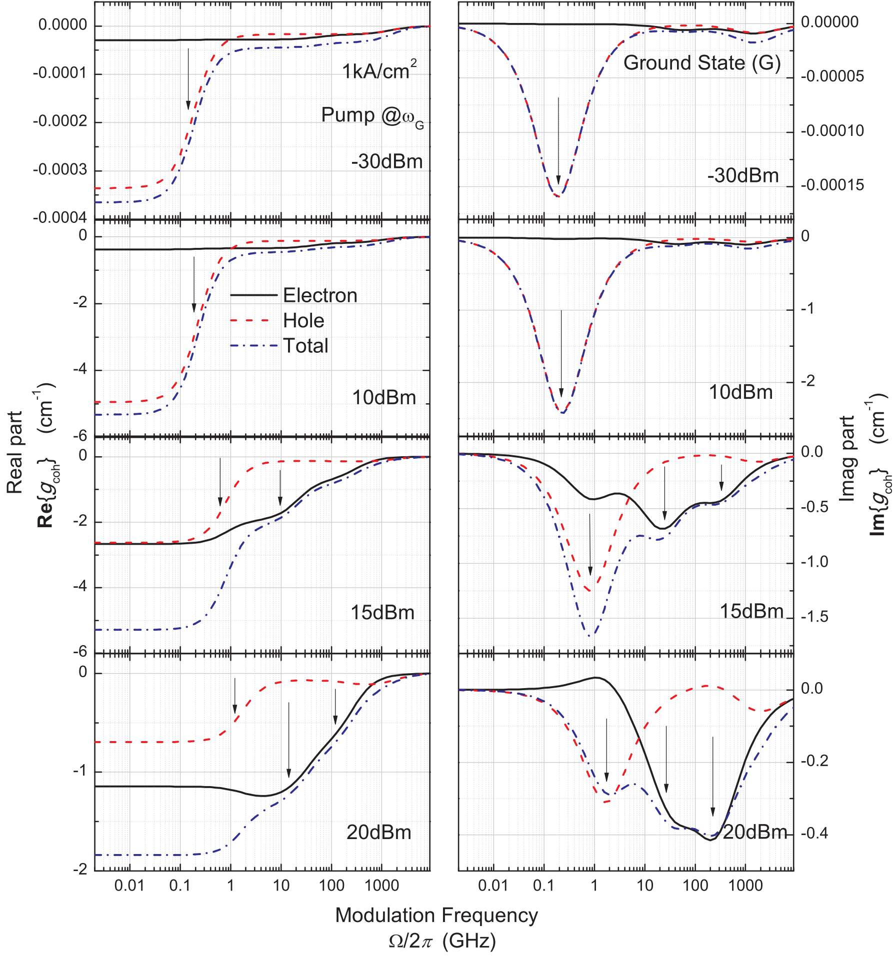

Figure 5.19: Variation of real and imaginary part of ground state coherent gain g_{coh} with modulation frequency Ω for different pump powers $@\omega_G$. The injection current density is $1kA/cm^2$. Gaussian homogeneous broadening lineshape is used. The spectral interval for dot subgroup is $\gamma_H/10$.

The estimation of electron and hole contributions to coherent gain at low modulation frequencies is not good enough to demonstrate the performance over a broad

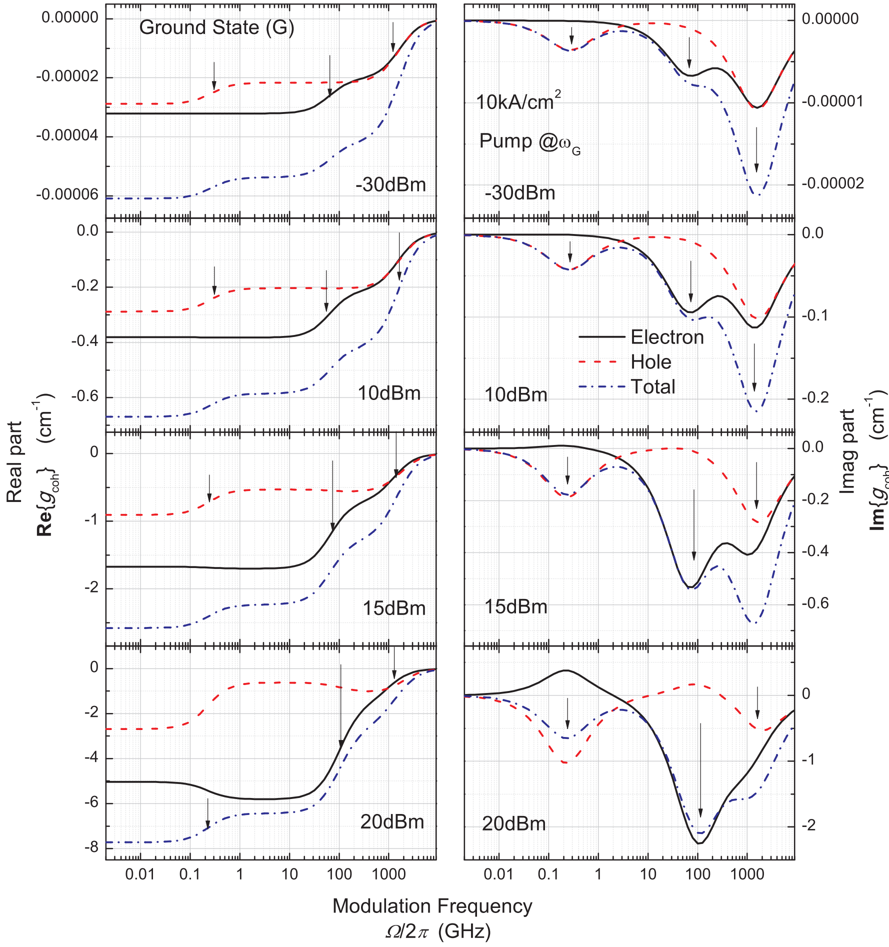

Figure 5.20: Variation of real and imaginary part of ground state coherent gain g_{coh} with modulation frequency Ω for different pump powers $@\omega_G$. The injection current density is 10 kA/cm^2. Gaussian homogeneous broadening lineshape is used. The spectral interval for dot subgroup is $\gamma_H/10$.

modulation frequency range. Here, we calculated the variation of real and image part of ground state coherent gain with modulation frequency for different pump powers at ω_G. In general, the increase of the pump power leads to the pump resonant with the ground state transitions. Figure 5.19 illustrated the results in the gain regime with low saturation power (1 kA/cm^2). The magnitude of coherent

gain at the low pump power -30 dBm (far from the saturation situation) is very small and dominated by slow hole contributions. When the pump power increases to 10 dBm (close to the saturation power), the coherent gain increases but with the spectral appearance similar to the unsaturated situation. When the pump power further increases and drives the devices into deeper gain saturation, extra resonant components start to appear at the high modulation frequencies from ten to several hundreds gigahertz. Such fast electron contributions can be identified by the peak characteristic frequencies of the imaginary parts. The hole contributions have been suppressed.

Figure 5.20 illustrates the results in the gain regime with high saturation power (10 kA/cm^2). Additional to the enhancement induced by large current injection, similar enhancement of the electron contributions by increasing pump power can be observed. In this case, a relatively high pump power (due to the high saturation power) is required to enhance the resonant components around 100 GHz. The corresponding variations of real and imaginary parts with modulation frequencies lead to rich dispersion properties, which can be used for nonlinear optical applications.

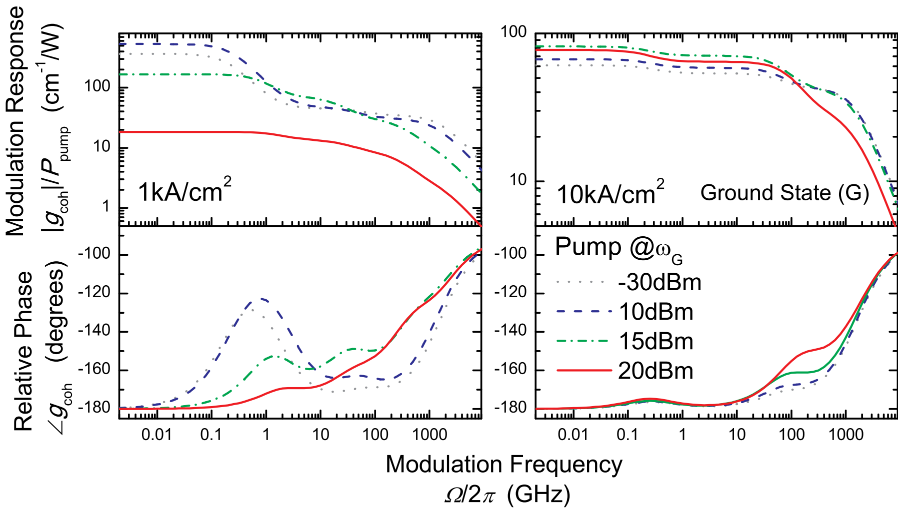

Figure 5.21: Illustration of ground states modulation response and relative phase as a function of modulation frequency induced by CW pump power @ω_G at low and high current density: (left)1 kA/cm^2, (right)10 kA/cm^2. Gaussian homogeneous broadening lineshape is used. The spectral interval for dot subgroup is $\gamma_H/10$.

Alternatively, we can illustrate the real and imaginary part of coherent gain g_{coh} in terms of the modulation response $|g_{coh}|/P_{pump}$ and the relative phase $\angle g_{coh}$. In this way, Figure 5.21 shows the same results in Figure 5.19 and 5.20. For the low current density (1 kA/cm^2) shown in Figure 5.21(left), the modulation response in the unsaturated situation has a relative large decrease around 1GHz. As the pump power increases, the bandwidth of modulation response expends over 100GHz. But the magnitude of the decrease in modulation responses is more than one order. The relative phase has a significant change between -180 degree (*in antiphase* at low modulation frequencies) to nearly -90 degree (*out of phase*, at high modulation frequencies). By increasing the pump power, the change of the relative phase at low modulation frequencies are mostly induced by suppressing the hole dynamical contributions. The change of the relative phase at high modulation frequencies are due to the enhancement of electron dynamical contributions.

In contrast, for the hight current density (10 kA/cm^2) shown in Figure 5.21(right), the bandwidth of the unsaturated modulation response has already reached over 100 GHz. When pump power increases, the magnitude of the changes in modulation responses is very small. As the high current injection has suppressed the hole dynamical contributions a lot, the relative phase changes at low modulation frequencies are barely observed. The relative phase changes at high modulation frequencies are induced by the corresponding enhancement of electron dynamical contributions.

Moreover, the propagation equation for the intensity envelope as in Eq. (5.7) indicates that the magnitude ratio between g_{coh} and $g_{incoh} - \alpha_{int}$ is also important to the overall device output. Nevertheless, by enhancing the coherent gain and meanwhile suppressing the incoherent gain due to gain saturation, the relative phase is highly likely preserved and observable from the device output.

5.3.5 Summary

An efficient semi-analytical approach is employed to investigate the small-signal medium response of inhomogeneously broadened QDs in the presence of an intensity modulated optical signal.

Hereby, the coherent population oscillations of QDs can be described on a microscopic footing. Distinct oscillation contributions from the electrons and holes are

shown to be determined by the corresponding carrier dynamical processes. The electron intra-dot relaxation contributes to the corresponding coherent gain responses, also referred to as the dynamic gain grating, ranging from 10 to 100 GHz or higher. The variations of the modulation response and relative phase, (or the real and imaginary part of dynamic gain grating), strongly depend on the input power and injection current density. The high-speed performance can be enhanced by increasing the input power or the injection current density, which is one of the interesting properties for nonlinear optical applications.

In practice, experiments with QD SOAs operation regime around 3-dB gain saturation level might reveal some of our theoretical predictions in terms of dynamic contributions. In particular, high-quality QD SOAs with a small internal loss, reasonable device gain, low saturation power are mostly desirable. The detailed models are fairly flexible to be justified for experiments facts.

Chapter 6

Coherent Population Oscillations in Semiconductor Optical Waveguide

This chapter presents a theoretical analysis of slow and fast light effects in semiconductor optical amplifiers (SOAs) based on coherent population oscillations (CPO) and the influence of optical filtering. Optical filtering prior to detection is shown to enable a significant increase of the controllable phase shift experienced by an intensity modulated signal traversing the waveguide. The theoretical model based on a wave mixing description of carrier dynamics in SOAs [64] accounts for the recent experimental results [73] and is used to analyze and interpret the dependence on material and device parameters. Furthermore analytical approximations are derived using a perturbation approach and are used to gain a better physical understanding of the underlying phenomena, in particular the refractive index dynamics.

6.1 Introduction of Optical Filtering Schemes

In the practically important case where the input optical signal is a double-sideband signal generated by sinusoidal modulation of a laser beam, it can be shown that the refractive index dynamics plays no role in the observed phase shift [52]. The change in group velocity is in this case only controlled by the gain or absorption dynamics.

Instead, using a single sideband excitation, in the form of a single sideband modulation or a modulated probe beam slightly detuned form a strong pump beam, as the input optical signal, has been proposed as a way of increasing the phase shift by benefiting from refractive index dynamics [134, 135]. However, FWM leads to the generation of a conjugate sideband, which to a large extent cancels the refractive index dynamics effects after photodetection. We proposed enhancing the phase shift and bandwidth by employing optical filtering before photodetection [136] and a maximum phase shift of 150 degrees at 19 GHz modulation frequency is achieved in a bulk SOA [73], corresponding to a several-fold increase of the absolute phase shift as well as achievable bandwidth. In [137] electrical filtering was employed after photodetection in order to suppress higher harmonics. In contrast, we are here filtering in the optical domain directly, thereby selectively suppressing beating components, and this is shown to lead to the observation of both phase delay (slow light) and phase advance (fast light) in the same device.

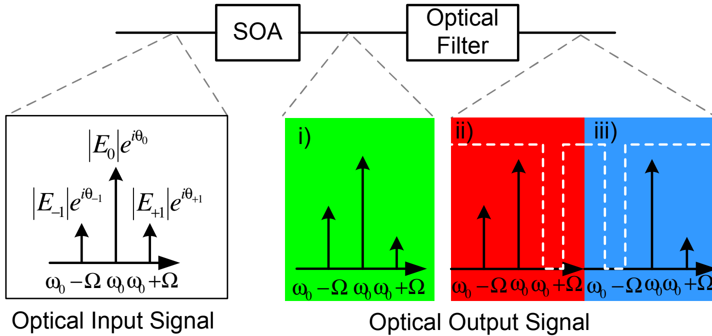

Figure 6.1: Optical signal processor based on SOA and pre-detection optical filtering for microwave phase shifter. Optical output signal with i) no sideband removed; ii) with blue-shifted sideband removed; iii) with red-shifted sideband removed.

Figure 6.1 shows the optical filtering schemes we introduced to the microwave phase shifter based on SOA. In general, the phase and amplitude of the electric fields of the optical signal are altered by an active semiconductor waveguide device, for example an SOA, via different wave mixing processes. By controlling the operation conditions of the photonic components, for example the input power to the SOA or its bias current, the microwave phase shift can be controlled. In ad-

dition to the SOA, optical filtering is included as part of optical signal processing. By employing an optical notch filter, one of the sidebands can be blocked and the other transmitted. When the bandwidth of the notch filter is much narrower than the modulation frequency, it can be approximated as an ideal filter suppressing all power in the sideband and the corresponding beating terms in the photodetector. We have investigated three cases: (Case-i) passing both sidebands, corresponding to the standard case considered so far without optical filtering, (Case-ii) suppressing the blue and passing the red-shifted sideband and (Case-iii) suppressing the red and passing the blue-shifted sideband.

6.2 Modeling of Microwave Phase shifter

6.2.1 Microwave modulated optical signal

A weakly sinusoidal intensity modulated (IM) signal with electric field of the general form

$$\begin{aligned} E(t,z) &= \frac{\sqrt{2}}{2}\left[E_0(z) + E_{-1}(z)\,e^{i\Omega t} + E_{+1}(z)\,e^{-i\Omega t}\right]e^{-i(\omega_0 t - k_0 z)} + c.c. \\ &= \frac{\sqrt{2}}{2}\left[|E_0(z)|\,e^{i\theta_0} + |E_{-1}(z)|\,e^{i\Omega t + i\theta_{-1}}\right. \\ &\quad \left. + |E_{+1}(z)|\,e^{-i\Omega t + i\theta_{+1}}\right]e^{-i(\omega_0 t - k_0 z)} + c.c. \end{aligned} \tag{6.1}$$

is assumed. Here ω_0 is the frequency of the optical carrier, k_0 is the propagation constant of the carrier and Ω is the modulation frequency. E_0, E_{-1}, E_{+1} are the corresponding complex amplitudes of the carrier, red-shifted sideband and blue-shifted sideband. θ_0, θ_{-1}, θ_{+1} are the corresponding optical spectral phases. For simplicity, the higher order sidebands are neglected. When $\theta_{-1} - \theta_0 = -(\theta_{+1} - \theta_0)$ and $E_{-1} = |E_{+1}|$, the optical signal is a pure amplitude modulated signal. When $\theta_{-1} - \theta_0 = \pi - (\theta_{+1} - \theta_0)$ and $|E_{-1}|/|E_0| = |E_{+1}|/|E_0| << 1$, the optical signal can be approximated as a phase modulated signal. In practice, the output optical field after a general Mach-Zehnder electro-optical modulator contains amplitude modulation (AM) and phase modulation (PM) [138] and the spectral phase difference is different from the pure AM signal.

6.2.2 Frequency domain modeling of SOA and semi-analytical solution

We theoretically analyze the slow and fast light effects in SOA structures due to CPO effects by using a wave mixing description [52, 66]. Wave mixing in active semiconductor waveguide has contributions from carrier density depletion, carrier heating (CH), spectral hole burning (SHB) as well as two-photon absorption (TPA) and Kerr effects [95]. For the modulation frequency range investigated in this paper with a magnitude on the order of $\sim 1/\tau_s$ (the inverse of carrier lifetime), i.e., up to some tens of GHz, the dominating mechanism mediating the wave mixing is pulsation of carrier density [139, 64]. The ultra fast effects are therefore neglected, which is a reasonable approximation in the regime of moderate input optical power. Based on the weak modulation assumption, the wave mixing problem in this paper can be approximated and simplified as interactions between three optical waves [139, 64]. Gain saturation due to ASE is neglected, which is reasonable unless the input power is very low.

The propagation equations for the electric fields are:

$$\begin{cases} \frac{\partial E_0}{\partial z} = \gamma_0 E_0 \\ \frac{\partial E_{-1}}{\partial z} = \gamma_0 E_{-1} + \xi_{-1}\left(\left|E_0\right|^2 E_{-1} + E_0^2 E_{+1}^* e^{i\Delta kz}\right) \\ \frac{\partial E_{+1}}{\partial z} = \gamma_0 E_{+1} + \xi_{+1}\left(\left|E_0\right|^2 E_{+1} + E_0^2 E_{-1}^* e^{i\Delta kz}\right) \end{cases} \tag{6.2}$$

with

$$\begin{aligned} \gamma_0 &= \frac{1}{2}\left[g_{sat}\left(1-i\alpha\right) - a_{\text{int}}\right], \qquad g_{sat} = \frac{\Gamma g_0}{1+S}, \\ S &= \frac{\left|E_0\right|^2 + \left|E_{-1}\right|^2 + \left|E_{+1}\right|^2}{P_{sat}}, \\ \xi_{\pm 1} &= -\frac{1}{2}\frac{g_{sat}}{P_{sat}}\frac{1-i\alpha}{1+S\mp i\Omega\tau_s}, \end{aligned} \tag{6.3}$$

Here, γ_0 corresponds to the first-order susceptibility with saturated modal gain g_{sat}, linewidth enhancement factor α and internal waveguide loss α_{int}. Γg_0 is the unsaturated modal gain, S is the normalized CW optical power and P_{sat} is saturation power. $\xi_{\pm 1}$ corresponds to the complex third-order susceptibility at the sidebands. τ_s is the carrier lifetime. Δk is the phase mismatching factor induced by

background material dispersion and waveguide dispersion. The phase matching condition $\Delta k = 0$ is fulfilled to a good approximation at the low detuning frequencies considered here [64].

Eq. (6.2) is nonlinear and can be solved numerically to directly provide the output signal from the SOA. However, in order to highlight the physical effects of the microwave phase shifting, and especially the effect of the filter, we derive a more transparent semi-analytical solution, which is subsequently considered in the perturbation treatment. The amplitudes E_{-1}, E_{+1} are assumed to be small and only first-order terms are included, consistently with the assumption of small-signal modulation. Similarly, gain saturation is governed by the carrier (pump) signal, corresponding to $S \approx |E_0|^2/P_{sat}$. By assuming, without loss of generality, the input electric field $E_0(0)$ to be real and defining the input conditions as:

$$\begin{cases} u\left(0\right) = E_{+1}(0) + E_{-1}^{*}(0) \\ v\left(0\right) = E_{+1}(0) - E_{-1}^{*}(0) \end{cases} \tag{6.4}$$

then a general analytical solution to Eq. 6.2 can be obtained for an SOA with given device length L (details in Appendix D):

$$\begin{cases} E_0\left(L\right) = E_0\left(0\right) e^{F(L)} \\ E_{+1}\left(L\right) = \tilde{E}_{+1}\left(L\right) e^{F(L)} \\ \qquad = e^{F(L)} \left\{ \frac{1}{2} v\left(0\right) + \frac{1}{2} u\left(0\right) \left[e^{H(L)} + i\alpha \left(1 - e^{H(L)}\right) \right] \right\} \\ E_{-1}^{*}\left(L\right) = \tilde{E}_{-1}^{*}\left(L\right) e^{F(L)^{*}} \\ \qquad = e^{F(L)^{*}} \left\{ -\frac{1}{2} v\left(0\right) + \frac{1}{2} u\left(0\right) \left[e^{H(L)} - i\alpha \left(1 - e^{H(L)}\right) \right] \right\} \end{cases} \tag{6.5}$$

The common complex amplification factor $F(L)$ is:

$$F\left(L\right) = \int_{0}^{L} \gamma_0 dz = \int_{S(0)}^{S(L)} \frac{\gamma_0}{\left(\gamma_0 + \gamma_0^{*}\right) S'} dS' \tag{6.6}$$

And the gain grating related complex amplification factor $H(L)$ is:

$$
\begin{aligned}
H(L) &\equiv \gamma_1 + i\beta_1 \\
&= P_{sat}\int_0^L \left(\xi_{+1}+\xi_{-1}^*\right) S dz = P_{sat}\int_{S(0)}^{S(L)} \frac{\left(\xi_{+1}+\xi_{-1}^*\right) S'}{\left(\gamma_0+\gamma_0^*\right) S'} dS' \\
&= -\int_{S(0)}^{S(L)} \frac{g_{sat}}{g_{sat}-a_{\text{int}}} \frac{1+S'}{\left(1+S'\right)^2+\left(\Omega\tau_s\right)^2} dS' \\
&\quad -i\int_{S(0)}^{S(L)} \frac{g_{sat}}{g_{sat}-a_{\text{int}}} \frac{\Omega\tau_s}{\left(1+S'\right)^2+\left(\Omega\tau_s\right)^2} dS'
\end{aligned}
\tag{6.7}
$$

Here γ_1 and β_1 indicate the real and imaginary part of $H(L)$, respectively. The integrals are determined by the input and output optical power S of the SOA, which can be calculated by solving the CW optical power propagation equation for the SOA numerically [52, 66]. Based on the wave mixing description and linear treatment shown in Eq. (6.5), $F(L)$ can be considered as a complex amplification to the CW signal due to the first-order susceptibility and $H(L)$ can be considered as the spatial integral of the spatially varying gain grating due to third-order susceptibility, which is implicitly determined by the spatial variation of the CW optical power S as well as the carrier lifetime τ_s along the waveguide. The refractive index grating is quantified by a non-zero linewidth enhancement factor α.

For a given SOA, the values of functions $F(L)$ and $H(L)$ can be modified by changing the unsaturated modal gain (electrical bias or current control), input CW optical power (optical intensity control) and modulation frequency (frequency detuning). In the following sections, numerical results refer to the model based on Eq. (6.2) and semi-analytical results refer to the model based on Eq. (6.5).

6.2.3 Photodetection and optical filtering

Due to the frequency beating between the optical waves in the photodetector, the photocurrent at modulation frequency Ω is proportional to the corresponding complex AC term P_{AC} of EE^*. For the microwave signal, a time delay Δt will introduce a phase change to $|P_{AC}|/2e^{-i\Omega(t-\Delta t)} + c.c.$ which is positive for a time delay and negative for a time advance.

The absolute microwave phase is determined by $\arg\{P_{AC}\}$, which can be tuned through different control schemes. The microwave phase shift

$$\Delta\phi = \arg\{P_{AC}\} - \arg\{P_{AC}\}\,|_{reference}$$

is stated relative to a reference situation, e.g., corresponding to $|H(L)| \approx 0$. In the following we separately write down the expressions for the AC power for the different cases of optical filtering.

i) Without optical filtering before photodetection

Without the notch filter both sidebands and the carrier are detected. The resulting AC power is:

$$\begin{aligned} P_{AC}(L) &= E_0^*(L)E_{+1}(L) + E_0(L)E_{-1}^*(L) \\ &= \frac{|E_0(L)|^2}{E_0(0)} u(0)\, e^{H(L)} \end{aligned} \tag{6.8}$$

The microwave phase shift induced by the SOA is determined by:

$$\begin{aligned} \Delta\phi &= \arg\left\{u(0)\, e^{H(L)}\right\} - \arg\left\{u(0)\, e^{H(L)}\right\}\Big|_{|H(L)|\approx 0} \\ &\approx \arg\left\{u(0)\, e^{H(L)} \cdot u(0)^*\right\} \end{aligned} \tag{6.9}$$

ii) Red-shifted sideband

With the notch filter blocking the blue-shifted sideband before photodetection only the red shifted sideband and the carrier are detected. The resulting AC power is:

$$\begin{aligned} P_{AC}(L) &= E_0(L)\, E_{-1}^*(L) \\ &= \frac{|E_0(L)|^2}{E_0(0)} \left\{-\frac{1}{2}v(0) + \frac{1}{2}u(0)\left[e^{H(L)} - i\alpha\left(1 - e^{H(L)}\right)\right]\right\} \end{aligned} \tag{6.10}$$

The microwave phase shift induced by the SOA is determined by:

$$\begin{aligned} \Delta\phi_{-1} &= \arg\left\{-\frac{1}{2}v(0) + \frac{1}{2}u(0)\left[e^{H(L)} - i\alpha\left(1 - e^{H(L)}\right)\right]\right\} \\ &\quad - \arg\left\{-\frac{1}{2}v(0) + \frac{1}{2}u(0)\left[e^{H(L)} - i\alpha\left(1 - e^{H(L)}\right)\right]\right\}\Bigg|_{|H(L)|\approx 0} \\ &\approx \arg\left\{\left\{-\frac{1}{2}v(0) + \frac{1}{2}u(0)\left[e^{H(L)} - i\alpha\left(1 - e^{H(L)}\right)\right]\right\} \cdot \left[-\frac{1}{2}v(0) + \frac{1}{2}u(0)\right]^*\right\} \end{aligned} \tag{6.11}$$

iii) Blue-shifted sideband

With the notch filter blocking the red-shifted sideband before photodetection only the blue-shifted sideband and the carrier are detected. The resulting AC power is:

$$\begin{aligned} P_{AC}(L) &= E_0^*(L)\, E_{+1}(L) \\ &= \frac{|E_0(L)|^2}{E_0(0)} \left\{ \frac{1}{2} v(0) + \frac{1}{2} u(0) \left[e^{H(L)} + i\alpha \left(1 - e^{H(L)} \right) \right] \right\} \end{aligned} \tag{6.12}$$

The microwave phase shift induced by SOA is determined by:

$$\begin{aligned} \Delta\phi_{+1} &= \arg\left\{ \frac{1}{2} v(0) + \frac{1}{2} u(0) \left[e^{H(L)} + i\alpha \left(1 - e^{H(L)} \right) \right] \right\} \\ &\quad - \arg\left\{ \frac{1}{2} v(0) + \frac{1}{2} u(0) \left[e^{H(L)} + i\alpha \left(1 - e^{H(L)} \right) \right] \right\} \bigg|_{|H(L)| \approx 0} \\ &\approx \arg\left\{ \left\{ \frac{1}{2} v(0) + \frac{1}{2} u(0) \left[e^{H(L)} + i\alpha \left(1 - e^{H(L)} \right) \right] \right\} \cdot \left[\frac{1}{2} v(0) + \frac{1}{2} u(0) \right]^* \right\} \end{aligned} \tag{6.13}$$

Thus based on the semi-analytical solution and different optical filtering schemes, the corresponding phase shift and AC power depends differently on the complex amplification $H(L)$, the linewidth enhancement factor α as well as the input optical signal $u(0)$, $v(0)$. In particular, for the usual case where both sidebands are detected, the phase shift does not depend on the α-factor, i.e., the dynamics of the refractive index does not influence the phase of the envelope. This is in agreement with [52] where it was shown also that this case can be analyzed by considering the dynamical effects of gain saturation. The effect of gain saturation also explains the time shifting of ultrashort pulses [63] in the limit where material dispersion can be neglected.

6.3 Phase Shifting Results

6.3.1 Comparison to experimental results

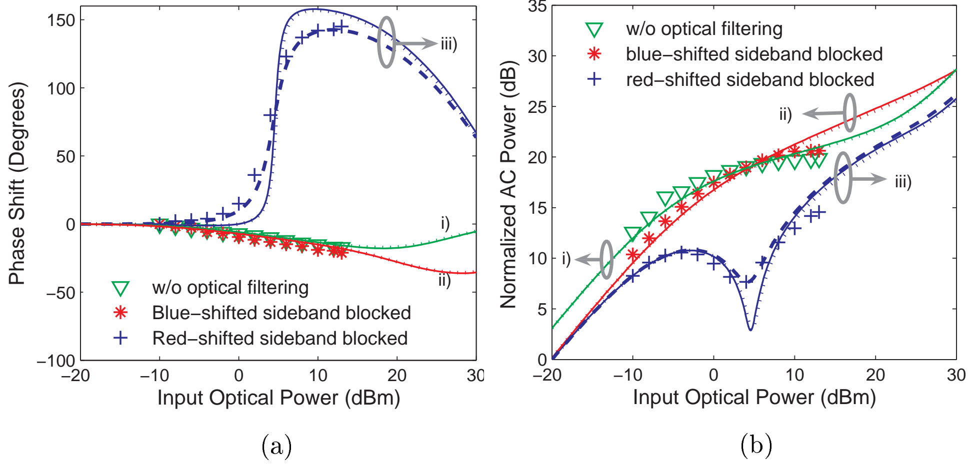

Figure 6.2: (a) Phase shifts and (b) AC power change vs.the input optical power in an SOA with different optical filtering schemes. The marks are experimental data taken on a bulk SOA at a modulation frequency of 19 GHz. The lines show the theoretical results for a pure AM input signal. The dotted lines are numerical results; the solid lines are semi-analytical results. The dashed line is a numerical result for an IM input signal with $\theta_{+1} - \theta_0 = \theta_{-1} - \theta_0 = 0.1$ *rad. Main model parameters:* P_{sat}*=10 dBm,* τ_s*=100 ps,* $\Gamma g_0 L$*=5.75,* α*=6 and* $\alpha_{int}L$*=2.75.*

In Figure 6.2 we compare experimental results from [73] with the results of our theoretical model. The experiments were carried out using a bulk SOA and a Fiber Bragg Grating (FBG) notch filter with 0.1nm bandwidth. Experimental (markers) and theoretical results (lines) are shown for the phase shift and the AC power change at a modulation frequency of 19 GHz as a function of input optical power for a fixed SOA injection current. The phase is measured relative to the values at the minimum input optical power. The AC power in the calculations is normalized to agree with the experimental value at the minimum input optical power when blocking red-shifted sideband. As seen in the figure the theoretical results agree very well with the experimental data for both phase shift and AC power. Both the numerical solution (solid line) and the semi-analytical calculation (dotted lines) are

presented. The small difference between numerical and semi-analytical results for a pure AM input signal indicates that the semi-analytical solution provides a very good approximation for the phase shift. In addition, Figure 6.2 shows modeling results for an IM input signal with a small spectral phase difference between different frequency components (dashed lines), corresponding to a realistic non-ideal modulator with a small chirp similar to the one used in the experiment. The inclusion of the small chirp provides a better quantitative agreement with experimental data. As shown in Figure 6.2(a), comparing with the conventional case without optical filtering, blocking the red-shifted or blue-shifted sideband leads to positive and negative phase changes, corresponding to the slow light and fast light, respectively. Especially when the red-shifted sideband is blocked, about 150 degrees phase delay is achieved, which corresponds to a ten-fold increase of the maximum phase shift obtained in the absence of optical filtering.

6.3.2 Parameter dependence

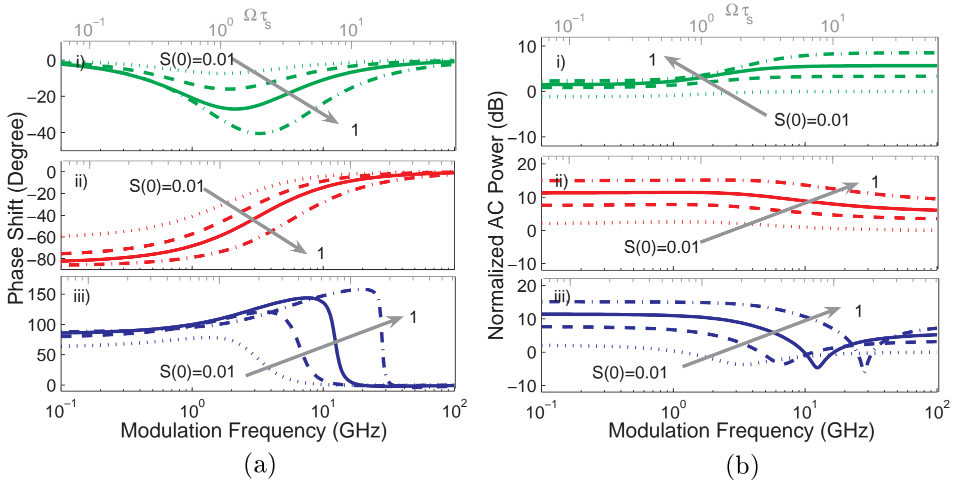

Figure 6.3: (a) Phase shifts and (b) AC power change vs. modulation frequency in an SOA with different optical filtering schemes. The numerical results are for a pure AM signal at different normalized input optical power S(0): 0.01 (dotted line), 0.03 (dashed line), 0.1 (solid line) and 1 (dash-dotted line). Main model parameters: P_{sat}*=10 dBm,* τ_s*=100 ps,* $\Gamma g_0 L$*=5.75,* α*=6 and* $\alpha_{int}L$*=2.75. Phase shift and AC power are relative to the value with minimum input power at maximum modulation frequency* ($|H(L)| \approx 0$).

As discussed previously the microwave phase shift in the SOA plus filter is influenced by several parameters. In this subsection, we numerically investigate the influence of the modulation frequency (carrier lifetime), linewidth enhancement factor, modal gain (internal loss) and waveguide length.

As shown in Figure 6.3, the phase shift for a pure AM signal as a function of modulation frequency indicates that the modulation response regarding the phase shift can be enhanced by optical filtering. Here the situation of minimum input power at maximum modulation frequency, $|H(L)| \approx 0$, is chosen as the reference for phase shift and AC power. Especially when the red-shifted sideband is blocked, 100 degree variable phase delay can be achieved for 20 dB optical power change over a large bandwidth 20 GHz. The sharp increase of the phase shift also corresponds to a dip in AC power. The result as a function of$\Omega\tau_s$ indicates that the modulation frequency can also be enhanced with a scale given by $1/\tau_s$. With the assumption of a constant carrier lifetime in the device, it qualitatively explains the experimentally measured phase shift and relative AC power as a function of modulation frequency in [73].

The phase shift results for a pure AM signal at a modulation frequency of 10 GHz as a function of the linewidth enhancement factor are shown in Figure 6.4. When the α-factor is zero, the employment of optical filtering has no influence on the phase shift as the refractive index dynamics is negligible. All the cases hence give the same phase shift as seen in the Figure 6.4. When the α-factor increases, the constant phase advance value for the conventional case without optical filtering indicates the refractive index dynamics effects are cancelled after photodetection. While the red-shifted sideband is blocked, the contribution from the refractive index dynamics turns the phase advance into a large delay. Moreover, comparing the results in Figure 6.4, the gain grating and refractive index grating for the given modulation frequency are stronger in an SOA with the shorter carrier lifetime τ_s=50 ps than the one with τ_s=100 ps. This also reveals that the magnitude of gain and refractive index grating depends on the product of modulation frequency and carrier lifetime shown in Figure 6.3. For bulk or QW semiconductor material with moderate α-factor, the refractive index dynamics for a given input power is strong. Although the α-factor of QDs is still debated in Section 5.1, for QD semiconductor material with a small α-factor the refractive index varies less but this might be compensated

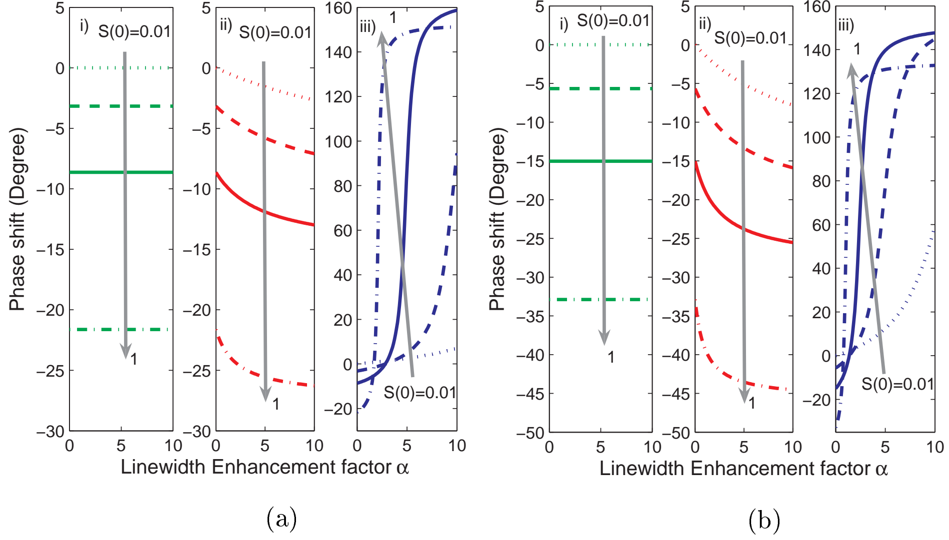

Figure 6.4: Phase shifts vs. linewidth enhancement factor α in an SOA with different optical filtering schemes for (a) τ_s=100 ps and (b) τ_s=50 ps. The numerical results are for a pure AM input signal at a modulation frequency of 10GHz with different normalized input power S(0): 0.01(dotted line), 0.03 (dashed line), 0.1 (solid line) and 1 (dash-dotted line). Main model parameters: P_{sat}=10 dBm, $\Gamma g_0 L$=5.75 and $\alpha_{int}L$=2.75. Phase shift is relative to the value at minimum input optical power with zero value of α.

by a short carrier lifetime. Or vice versa, our optical filtering scheme might be used to experimentally distinguish whether the QD SOAs in reality has a zero or bulk-like α-factor.

The phase shift results for a pure AM signal at a modulation frequency 10 GHz as a function of modal gain for a 500 μm long active semiconductor waveguide are shown in Figure 6.5. Here we estimated the phase shifting in the absorption/gain regime with the assumption of constant carrier lifetime and saturation power, Although the absolute scaling of the phase shift will be different for the realistic varying values of carrier lifetime and saturation power for different electrical bias/current control, the results qualitatively indicate the properties of phase delay/advance by electrical bias/current control. By tuning the SOA from the gain regime into absorption regime, the sign of the phase shift changes from negative (fast light) to

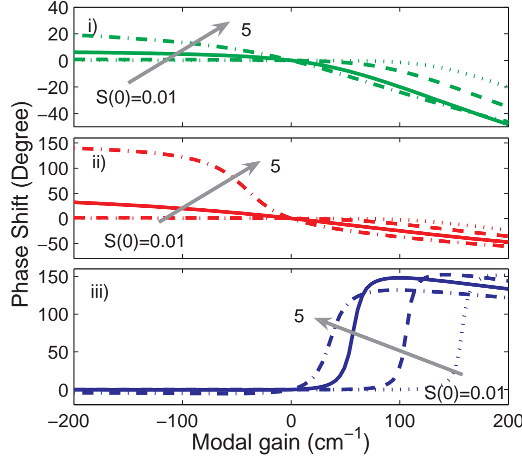

Figure 6.5: Phase shift vs. modal gain in an SOA with different optical filtering schemes. The numerical results for a pure AM input signal at a modulation frequency 10 GHz with different normalized optical power S(0): 0.01 (dotted line), 0.1 (dashed line), 1(solid line) and 5 (dash-dotted line). Main model parameters: τ_s*=100 ps,* $\alpha = 6$*, L=500* μ*m.* α_{int}*=55 cm*$^{-1}$*. Phase shift is relative to the value at zero modal gain.*

positive (slow light) without optical filtering [70]. By blocking the blue-shifted sideband, we observe a large phase delay in the absorption regime and a phase advance in the gain regime. By blocking the red-shifted sideband, we observe a large phase delay in the gain regime and phase advance in the absorption regime. This flipping of the sign of corresponding phase shift can be interpreted by the perturbation treatment in the next section. The internal loss also influences the final phase shift as discussed in [66].

The phase shifts for a pure AM signal at a modulation frequency of 10 GHz as a function of the waveguide length of an SOA for different input optical power levels are presented in Figure 6.6(left). For the conventional case without optical filtering, a long SOA device is expected to show larger device gain (unless limited by ASE) and thus enhance the variable phase shift range [66]. As shown in Figure 6.6, for example, for the given input optical power range, 32 degree phase advance can be achieved through a 1000 μm long device comparing with 22 degree phase advance through a 500 μm long SOA. However, by blocking the red-shifted sideband a much

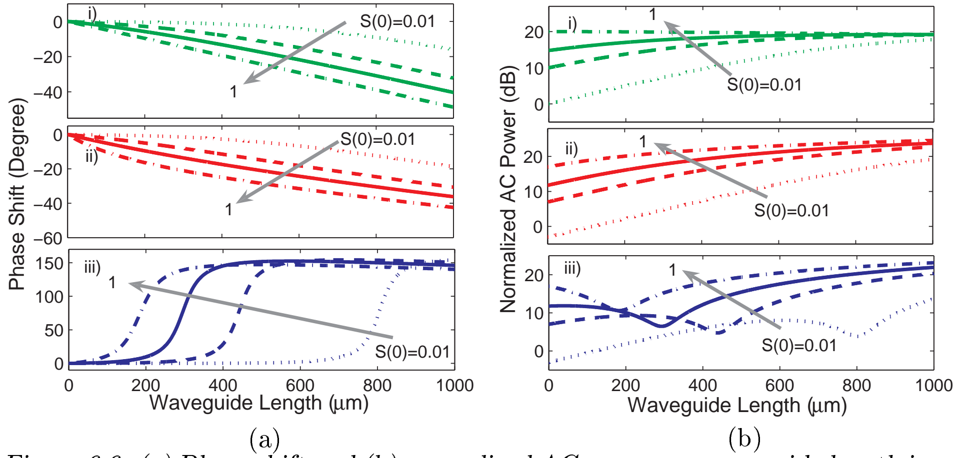

Figure 6.6: (a) Phase shift and (b) normalized AC power vs. waveguide length in an SOA with different optical filtering schemes. The numerical results for a pure AM input signal at a modulation frequency 10 GHz with different normalized optical power S(0): 0.01 (dotted line), 0.1 (dashed line), 0.3(solid line) and 1 (dash-dotted line). Main model parameters: τ_s*=100 ps,* $\alpha = 6$*,* Γg_0*=115 cm*$^{-1}$*,* α_{int}*=55 cm*$^{-1}$*. Phase shift and AC power is relative to the value with minimum input power.*

larger effect is obtained, about 150 degree phase delay can be achieved in an SOA with the length of 200-600 μm, corresponding to the moderate small signal device gain of 5-15 dB. It indicates that the corresponding spatial integral of the refractive index grating (quantified by the large value of the α-factor) over this length is significant enough to achieve a large variable phase change range. However, as shown in Figure 6.6(right) the corresponding AC power has a notch-like variation accompanying the large phase shift. We should also emphasize that our present model does not include ASE noise, which is expected to limit the gain and phase shift for long devices [69].

6.4 Perturbation Analysis and Discussion

In order to gain a better understanding of the physical effects resulting in the large impact of optical filtering on the microwave phase shift, e.g., the large phase change shown in Figure 6.2 by tuning input optical power, it is helpful to further simplify the model. Therefore we investigate the filter-assisted phase shift by perturbation

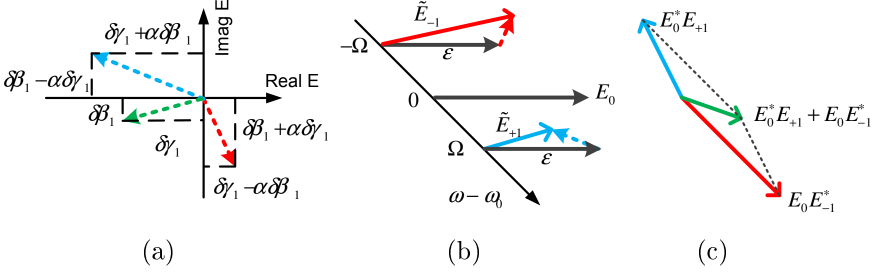

(a) (b) (c)

Figure 6.7: Illustration of the relative amplitude and phase changes of the complex electric field. (a) Perturbations induced by gain grating and refractive index grating. (b) Electric field components including perturbation. (c) Resulting beating terms after a certain propagation distance.

analysis. For simplicity, we assume that the input optical signal satisfies $|u(0)| = u(0) = \varepsilon$ and $|v(0)| = 0$ as an pure AM signal with amplitude ε normalized to the carrier. Internal loss is also neglected.

6.4.1 Perturbation without spatial variation

Firstly, the enhancement of the phase shift by the optical filtering can be qualitatively understood from a perturbation treatment of the FWM in the limit of relatively small propagation length δL [73]. This is equivalent to investigating the role of the gain grating and the refractive index grating as material response without spatial variation along the propagation coordinate.

We may obtain the electric fields after the amplification and interaction in the SOA based on Eq. (6.5):

$$\begin{cases} \tilde{E}_{+1}(\delta L) = \varepsilon\left(1 + \delta\gamma_1 + \alpha\delta\beta_1 + i\delta\beta_1 - i\alpha\delta\gamma_1\right) \\ \tilde{E}^*_{-1}(\delta L) = \varepsilon\left(1 + \delta\gamma_1 - \alpha\delta\beta_1 + i\delta\beta_1 + i\alpha\delta\gamma_1\right) \end{cases} \tag{6.14}$$

Where

$$\begin{cases} \delta\gamma_1 = -g_{sat}\frac{(1+S)S}{(1+S)^2+(\Omega\tau_s)^2}\delta L \\ \delta\beta_1 = -g_{sat}\frac{\Omega\tau_s S}{(1+S)^2+(\Omega\tau_s)^2}\delta L \end{cases} \tag{6.15}$$

The changes in the complex field components are illustrated in a phasor diagram in Figure 6.7. It is seen that both $\delta\gamma_1$ and $\delta\beta_1$ are negative for an SOA with positive

gain. The perturbations with α-factor, which indicate the sign of the corresponding phase changes, can be sketched in Figure 6.7(a) and (b).

When both sidebands are detected after the SOA, the phase shift becomes $\delta\phi = \arg\{1+\delta\gamma_1+i\delta\beta_1\}$ indicating that the influence from the refractive index dynamics is canceled. When employing an optical filter to block the red-shifted sideband before detection, the phase shift, $\delta\phi_{+1} = \arg\{1 + \delta\gamma_1 + \alpha\delta\beta_1 + i(\delta\beta_1 - \alpha\delta\gamma_1)\}$, includes a contribution $-\alpha\delta\gamma_1$, corresponding to an additional delay (positive phase shift) for positive α-factor. If the blue-shifted sideband is blocked before detection, the phase shift $\delta\phi_{-1} = \arg\{1 + \delta\gamma_1 - \alpha\delta\beta_1 + i(\delta\beta_1 + \alpha\delta\gamma_1)\}$ instead contains a term $\alpha\delta\gamma_1$, corresponding to an additional advance (negative phase shift). When the semiconductor waveguide devices are biased in the absorption regime, the sign of the corresponding phase shift will be flipped as in Figure 6.5.

6.4.2 Perturbation including propagation effects

Notice that treatments in previous section only qualitatively explains the sign of phase shifting. For an SOA device with given length L, the vision of perturbation analysis should be extended to take into account propagation effects as shown in Figure 6.7(c). The optical pump power levels at the input and output of SOA satisfy the relation:

$$S\left(L\right) = S\left(0\right)T_{sat} \tag{6.16}$$

Here $T_{sat} = F(L) + F(L)^*$ is the saturated value of the transmission.

For a small perturbation of input power δ_S the output power satisfies the relation:

$$\begin{aligned} S\left(L\right) + \delta S_{out} &= \left(S\left(0\right) + \delta S\right)\left(T_{sat} + \frac{\partial T_{sat}}{\partial S}\delta S\right) \\ &\approx S(0)T_{sat} + \delta S\left(T_{sat} + S\left(0\right)\frac{\partial T_{sat}}{\partial S}\right) \end{aligned} \tag{6.17}$$

where δS_{out} is the resulting perturbation of the output power. The corresponding differential change of $H(L)$ is:

$$\delta H\left(L\right) \equiv \delta\gamma_1\left(L\right) + i\delta\beta_1\left(L\right) = H\left(L\right)|_{S(0)+\delta S} - H\left(L\right)|_{S(0)} \tag{6.18}$$

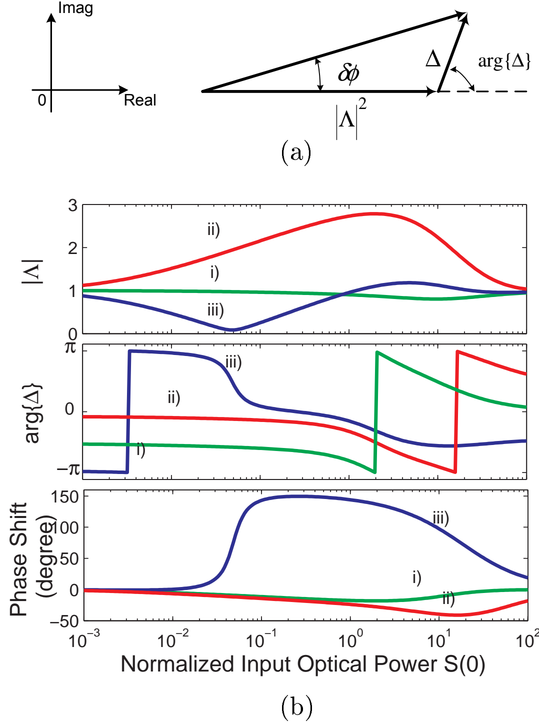

Figure 6.8: (a) Illustration of the perturbation approach including propagation effects in an SOA. (b) Numerical example with different optical filtering schemes for a pure AM input signal as a function of normalized input optical power S(0). ($\Gamma g_0 L = 5.75$, $\alpha_{int} L = 0$, $\alpha = 6$ and $\Omega\tau_s = 12$)

where

$$\begin{cases} \frac{\delta\gamma_1(L)}{\delta S} = P_{sat}\left[\frac{1+S(0)}{(1+S(0))^2+(\Omega\tau_s)^2} - \frac{1+S(L)}{(1+S(L))^2+(\Omega\tau_s)^2}\left(T_{sat} + S\left(0\right)\frac{\partial T_{sat}}{\partial S}\right)\right] \\ \frac{\delta\beta_1(L)}{\delta S} = P_{sat}\left[\frac{\Omega\tau_s}{(1+S(0))^2+(\Omega\tau_s)^2} - \frac{\Omega\tau_s}{(1+S(L))^2+(\Omega\tau_s)^2}\left(T_{sat} + S\left(0\right)\frac{\partial T_{sat}}{\partial S}\right)\right] \end{cases} \tag{6.19}$$

The electric fields after the amplification and interaction in the SOA are based on Eq. (6.5):

$$\begin{cases} \tilde{E}_{+1}\left(L, \delta S\right) = \varepsilon\left[e^{H(L)} + i\alpha\left(1 - e^{H(L)}\right) + e^{H(L)}\left(e^{\delta H(L)} - 1\right)\left(1 - i\alpha\right)\right] \\ \tilde{E}^*_{-1}\left(L, \delta S\right) = \varepsilon\left[e^{H(L)} - i\alpha\left(1 - e^{H(L)}\right) + e^{H(L)}\left(e^{\delta H(L)} - 1\right)\left(1 + i\alpha\right)\right] \end{cases} \tag{6.20}$$

The perturbations $e^{H(L)}(e^{\delta H(L)} - 1)(1 \pm i\alpha)$ induced by the gain grating and the refractive index grating can alter the amplitude and phase of the corresponding electric fields destructively (or constructively) when the perturbations are in antiphase (or in phase) compared with the complex amplification terms $e^{H(L)} \mp i\alpha(1 - e^{H(L)})$. As the destructive addition turns to the constructive one, the perturbations thus lead to a dip of the related AC power, as seen in Figure 6.2.

Using Eq. (6.9), (6.11) and (6.13) for the different cases of filtering, the corresponding differential phase change $\delta\phi$ with respect to the intensity can be expressed as:

$$\delta\phi = \arg\left\{|\Lambda|^2 + \Delta\right\} \tag{6.21}$$

i) Without optical filtering before photodetection

$$\begin{cases} |\Lambda|^2 = \left|e^{H(L)}\right|^2 \\ \Delta = \left(e^{\delta H(L)} - 1\right) \cdot \left|e^{H(L)}\right|^2 \end{cases} \tag{6.22}$$

ii) Red-shifted sideband

$$\begin{cases} |\Lambda|^2 = \left|e^{H(L)} - i\alpha\left(1 - e^{H(L)}\right)\right|^2 \\ \Delta = \left(e^{\delta H(L)} - 1\right)(1 + i\alpha) \cdot e^{H(L)} \cdot \left[e^{H(L)} - i\alpha\left(1 - e^{H(L)}\right)\right]^* \end{cases} \tag{6.23}$$

iii) Blue-shifted sideband

$$\begin{cases} |\Lambda|^2 = \left|e^{H(L)} + i\alpha\left(1 - e^{H(L)}\right)\right|^2 \\ \Delta = \left(e^{\delta H(L)} - 1\right)(1 - i\alpha) \cdot e^{H(L)} \cdot \left[e^{H(L)} + i\alpha\left(1 - e^{H(L)}\right)\right]^* \end{cases} \tag{6.24}$$

Here, $|\Lambda|$ indicates the absolute value of the complex amplification without perturbation and Δ is the perturbation term.

For a pure AM input signal, $|\Lambda|$ is correlated to the modulation index and AC power of the output optical signal into the photodetector. To the first order in δS

we have:

$$\begin{aligned} &\left(e^{\delta H(L)}-1\right)(1 \pm i\alpha) \\ &\approx \left(\delta\gamma_1(L) \mp \alpha\delta\beta_1(L) + i\delta\beta_1(L) \pm i\alpha\delta\gamma_1(L)\right) \end{aligned} \tag{6.25}$$

Here we illustrate the perturbation results including propagation effects based on Eq. (6.21) as a phasor diagram in Figure 6.8(a). The value of $\arg\{\Delta\}$ determines the sign of $\delta\phi$: A value between 0 and π for $\arg\{\Delta\}$ introduces a positive differential phase change $\delta\phi$ (phase delay); a value between $-\pi$ and 0 for $\arg\{\Delta\}$ introduces a negative differential phase change $\delta\phi$ (phase advance). For a perturbation with unit amplitude $|\Delta|$, a larger differential phase change $\delta\phi$ is expected with a smaller $|\Lambda|$ value. By employing optical filtering, both Δ and $|\Lambda|$ are significantly influenced by α-factor as well as $\delta\gamma_1(L)$, $\delta\beta_1(L)$ and $H(L)$.

In Figure 6.8(b), a numerical example of Eq. (6.21) in an SOA is used to illustrate the complex situation, whereas only the electric field of blue-shifted sideband evolves from destructively to constructively. When the red-shifted sideband is blocked, the large phase change can thus be achieved around the dip of $|\Lambda|$. This also reveals the correlation between the large phase change and the dip in AC power seen in the numerical and experimental results as shown in Figure 6.2.

When the device length is approaching zero, corresponding to $|H(L)| \approx 0$ and $|\Lambda| \approx 1$, this perturbation analysis is consistent with the simple interpretation of phase delay and advance without spatial variation in previous section. The perturbation analysis used here may also be used to analyze the role of the phase difference between different frequency components of the input optical signal, which will become increasingly important in practice. Such a phase difference may appear due to chirp in the modulator or dispersion in the optical path before the SOA. As far as modeling in the regime of weak modulation is concerned, a change of the phase difference does not change the gain grating or refractive index grating in the SOA from the case of pure AM signal, as seen in Eq. (6.7). However, the amplitude and phase of the electric fields are influenced by such a change of phase difference, based on Eq. (6.5), and thus the final filter-assisted phase delay or advance can be modified.

6.5 Summary

We have theoretically investigated the physical effects of CPO that contribute to microwave phase shifts in semiconductor optical waveguides, in particular analyzing the influence of optical filtering.

The semi-analytical solution accounts for the evolution of the electric fields with complex amplification factors, which are spatial integrals of spatially varying gain and refractive index gratings. When optical filtering is included to selectively suppress a sideband of the optical signal before photodetection, the refractive index grating becomes important and leads to the observation of both phase delay and phase advance.

In the small signal regime, the strength of the gain grating is influenced by the input optical power (optical intensity control), modulation frequency/carrier lifetime (frequency detuning), modal gain/internal loss (electrical bias/current control). The strength of the refractive index grating is quantified by the α-factor, which means that the influence of optical filtering can be increased significantly in QW and bulk devices, while QD devices with low α-factor are expected to show a smaller influence from filtering. Or vice versa, our optical filtering scheme can be implemented as a standard experimental approach to distinguish whether or not QD SOAs has a non-zero bulk-like α-factor. In return, such experimental results will be valuable inputs for the debates in Section 5.1.

A large phase shift is achievable at higher modulation frequency with a moderate small signal device gain when properly exploiting optical filtering. Furthermore, the effects of phase difference between different frequency components of the input optical signal on the measured microwave phase shift adds the potential to further influence the filter-assisted phase shifts.

The phase shifting effect induced by optical filtering is qualitatively explained by a simple perturbation approach. This approximate approach provides a simple physical explanation of the large difference, seen in both experiments and numerical simulations, between filtering the red and the blue modulation sideband.

Chapter 7

Microwave Phase Shifting based on QD SOAs

In addition to the general discussion of slow and fast light in semiconductor waveguide in Chapter 6, this chapter presents two proposals to realize the microwave phase shifting based on the understanding of harmonic responses of QD SOAs. As already discussed in Chapter 5, our small-signal harmonic analysis reveals that ultrafast carrier dynamics of QDs leads to the coherent gain responses with rich dispersion details over a wide modulation frequency range. These unique properties are attractive to alleviate the limits of the achievable phase shifting and bandwidth induced by the slow total carrier density pulsation in SOAs. Here, the theoretical investigations are based on time-domain implementation of our MPREM model presented in Chapter 4. Gaussian homogeneous broadening lineshape is used. Standard Fourier signal analysis are used to retrieve the first-order harmonic responses. The treatment focuses on the gain dynamics only, equivalent to the situation with zero linewidth enhancement factor. The parameters are given in Appendix F.

For the proposal with one optical carrier as input, the configuration is same to the conventional scheme used for the investigation of coherent population oscillations effects in Chapter 6. For the proposal with additional optical carriers as input, the configuration is equivalent to the investigations of the cross gain modulation effects, which was reported in a distributed feedback (DFB) Laser [140].

7.1 Coherent Population Oscillations Effects

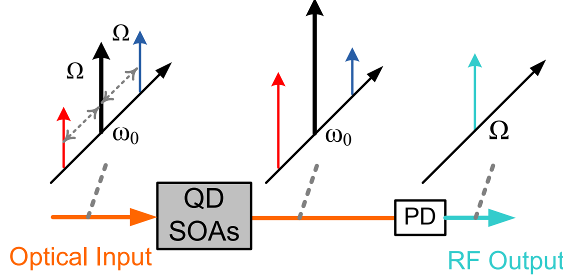

Figure 7.1: Schematic configuration of microwave phase shifter based on coherent population oscillations (CPO) effects in QD SOAs.

Figure 7.1 shows the conventional scheme to achieve slow/fast light based on CPO effects for sinusoidally modulation optical signals as discussed in Chapter 6. Since the refractive index change imposed on a probe component by wave mixing with a pump is anti-symmetric with respect to the detuning frequency between pump and probe, the effect of such anti-symmetric phase change cancels out for a conventional double sideband signal with a central carrier (pump) and two modulation sidebands (probes) [141]. Hereby, only dynamic gain gratings in QD SOAs contribute to the phase shifting. In this section, our QD SOAs model is referred to as the full model. The semi-analytical solutions of the wave-mixing model in Chapter 6 are referred to as the (carrier density pulsation) CDP model.

In general, we have fast light (negative phase shifts) in the gain regime with respect to the speed of light with no CPO effects, i.e., for very low input power. In order to compare the phase shifts obtained at different optical transitions (ω_G and ω_E), we start with a reference current density (1 kA/cm^2), at which the modal gains for the compared optical transitions are similar as shown in Figure 5.10.

Figure 7.2 shows the simulated phase shift and RF optical gain as a function of modulation frequency at different optical transitions corresponding to ground state (ω_G) and excited state (ω_E) for different input pump powers. For the G transition, shown in Figure 7.2(left), a maximum phase shift of around -34 degree is observed at a peak modulation frequency around 300 MHz by increasing the input power by 20 dB, and this phase shift is accompanied by a steep RF optical gain variation.

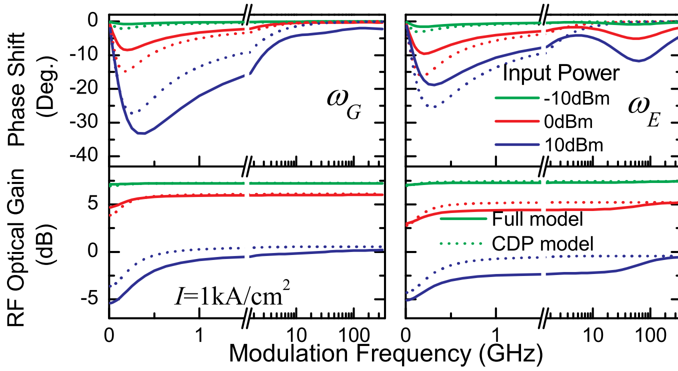

Figure 7.2: Phase shift and RF optical gain as a function of modulation frequency at optical transitions corresponding to ground (left) and excited (right) states of QD SOAs for different input pump powers under moderate injection current (fast light in gain regime). Solid curves are based on the full model. Dotted curves are based on the CDP model used in chapter 6. The injected current density is 1 kA/cm^2.

As the modulation frequency is increased, the phase shifts decreases. These results agree well with experimental observations [142] and are explained by the slow CDP model discussed in Chapter 6. As such, the frequency is limited by the carrier recovery rate, τ_s^{-1}. Dotted curves in Figure 7.2 are thus reference curves calculated with the assumptions of constant carrier lifetime and CW saturation power.

As we consider the case of the E transition, shown in Figure 7.2(right), we observe the appearance of phase shift maxima at two separate frequencies: a value of -18 degree peaked around 300 MHz and a value of -12 degree peaked at a much higher frequency of around 70 GHz. Because of the different saturation powers for G and E transitions, even with similar modal gain, the magnitude of the two phase shifts differs considerably. The high-frequency peak corresponds to the inverse of a combination of downward electron transition times, which is determined by the slowest process on the order of several picoseconds. Detailed discussion of the coherent gain contributions are presented in Chapter 5. This effect is obviously not taken into account in the CDP model in Chapter 6 due to the exclusion of ultrafast dynamics. As a comparison, the intraband scattering dominated SHB (CH) dynamics in bulk or QW occurs on a time scale of about 50 fs (500 fs) and the corresponding phase shift would be appearing in the THz frequency range and

correspond to a very small phase shift amplitude. In QDs, the intra-dot scattering dominated downward electron transition rates, especially for excited state, are two to three orders faster than the CDP process, and one to two orders slower than the SHB (or CH) process in bulk or QW media. We observe also that the two phase shift peaks correspond to the two different plateau-levels of RF optical gain seen in the lower plot of Figure 7.2. The high-frequency peak corresponds to the resonant response determined by the ultrafast electron intra-dot dynamics as shown in Figure 5.12(b) and 5.13(b).

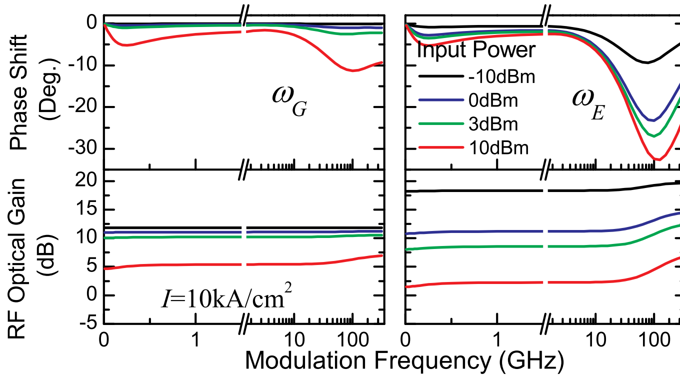

Figure 7.3: Phase shift and RF optical gain as a function of modulation frequency at optical transitions corresponding to ground (left) and excited (right) states of QD SOAs for different input pump powers under strong injection current (fast light in gain regime). The injected current density is 10 kA/cm^2.

As we increase the injection current to 10 kA/cm^2, this downward electron transition dynamics in QDs is further enhanced and dominates over the CDP mechanism [131]. The second phase shift peak is enhanced (to around -11 degree for ω_G and -22 degree for ω_E) and shifted towards 100 GHz, or even higher frequencies, as shown in Figure 7.3. The plateaus of constant RF optical gain are also extended to higher frequencies. As discussed in the Chapter 5, the *ultrafast* carrier dynamical contribution, i.e., the relaxations between the ground and excited states τ_{EG}^{-1}, do not imply the large coherent gain response change in the target frequency range of 10-100 GHz, see Figure 5.12(c). Instead, the relatively *slow* carrier dynamical processes for excited states result in a larger change see 5.13(b). In reality, the ultrafast carrier dynamics in QD SOAs might strongly depend on the bias control

condition and signal power as well as dot shape and fabrication process via the intra-dot scattering times, see e.g. [26], which provides potential for controlling the second peak modulation frequency.

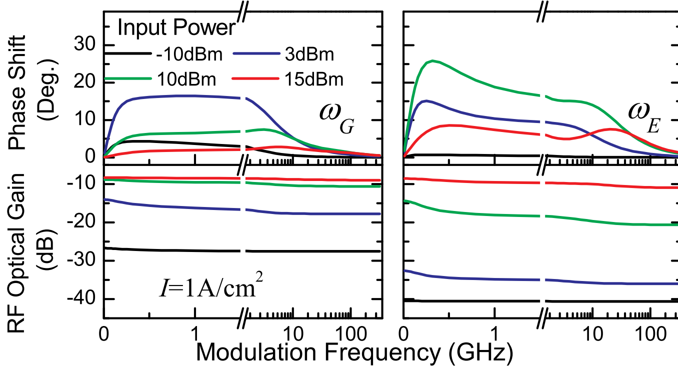

Figure 7.4: Phase shift and RF optical gain as a function of modulation frequency at optical transitions corresponding to ground (left) and excited (right) states of QD SOAs for different input pump powers under a weak injection current (slow light in absorption regime). The injected current density is 1 A/cm^2.

Furthermore, as shown in Figure 7.4, similar effects on slow light in the absorption regime (under a weak forward bias) can also be observed whereas the additional phase shift peak and flat plateaus of RF optical gains appearing at high modulation frequencies originate from upward electron transitions see Figure 5.12(c) and see Figure 5.13(c). As we assumed the electron upward transitions to be dominated by thermal excitation, the height of the energy barriers relative to the kinetic energy are important in determining the characteristic modulation frequencies and the phase shift.

In summary, we have numerically demonstrated that a tunable RF phase shifter based on CPO effects (dynamic gain grating) can be achieved at modulation frequencies, i.e., 30-100 GHz, much higher than the inverse of the carrier lifetime. This effect is explained as a result of nonequilibrium effects in QDs and highlights the importance of the intra-dot electron scattering processes, which is consistent with the results discussed in chapter 5. The magnitude of tunable phase shift can be further enhanced by the idea of cascading [72] and optical filtering discussed in chapter 6.

7.2 Cross Gain Modulation Effects

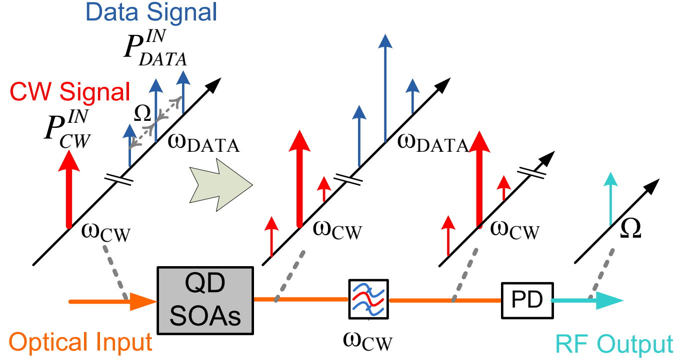

Figure 7.5: Configuration of wavelength up-conversion based on cross gain modulation in QD SOAs. PD: photodetector.

Here, we also proposed a novel dual-wavelength-configured phase shifter based on dynamic gain gratings induced by high speed XGM in QD SOAs as shown in Figure 7.5. It is similar to the small signal XGM configuration in [143] with a sine-modulated data signal, at optical frequency ω_{DATA}, as input:

$$P_{DATA}^{IN}[1 + m_0 \cos(\Omega t)],$$

where P_{DATA}^{IN}, m_0 and Ω are input power, modulation index and modulation frequency. The data signal will modulate the gain of the SOA and thus in turn XGM in the amplifier will transfer the modulation to the co-propagating continuous-wave (CW) signal at optical frequency ω_{CW} as an XGM converted signal with an inverse pattern.

For simplicity, by ideal flat-top selective optical bandpass filtering, the output intensity envelope centered around ω_{DATA} and ω_{CW} can be detected in the form of:

$$P_X^{OUT}[1 + m_X^{OUT} \cos(\Omega t + \varphi_X^{OUT})],$$

Here, P_X^{OUT}, m_X^{OUT} and φ_X^{OUT} (X=CW, DATA) are the mean output optical intensity, modulation index and RF phase shift at the given optical frequency. The corresponding RF optical gain is in the form of $P_X^{OUT} m_X^{OUT}/(P_{DATA}^{IN} m_0)$.

Note that there are two main changes compared to previous results. Firstly, the optical frequencies of the data signal ($\omega_{DATA} = \omega_E$) and CW signal ($\omega_{CW} = \omega_G$) are chosen corresponding to the two lowest discrete QD bound states, i.e., the excited (E) and ground (G) state, which are connected by fast (sub-picosecond) inter-subband electron relaxation. The frequency detuning ($\omega_{DATA} - \omega_{CW} = \omega_E - \omega_G$) is assumed much larger than the homogenous linewidth of the QDs, and thus FWM interaction between data and CW signals are neglected. Secondly, the input CW power P_{CW}^{IN} is variable and acts as a strong pump, while the average input data power P_{DATA}^{IN} is constant and relatively weak. Therefore the dynamic gain grating is no longer solely determined by the data signal as in the small signal regime. Instead, in terms of the two wave competition [143], both the data and XGM converted signal are considered to compete for the available carriers and interact with dynamic gain gratings (at frequencies ω_{DATA} and ω_{CW}) via fast intra-dot scattering effects in QDs. Recent calculations and experiments indicate that quantum dot (QD) based devices are good candidates for small signal cross gain modulation (XGM) up to 40 GHz in QD SOAs. The high-speed XGM can be increased by increasing the current injection and suppressing the total carrier density depletion [44]. As a consequence, we emphasize the phase shifting profile of the XGM converted signal (ω_{CW}) after the QD SOAs for a strong current injection (10 kA/cm^2).

Figure 7.6(left) shows the calculated incoherent modal gain of QD SOAs for different values of the input CW power. Details regarding the CW gain saturation are presented in Chapter 5. As the stimulated emission at frequency ω_{CW} (input CW power) increases, spectral holes are seen to develop in the gain spectrum, centered at the E and G states. Notice that the SHB corresponding to the E state transition originates from the large contrast between the fastest intradot electron relaxation and the intermediate electron capture from R to E states, which is synonymous to the existence of an injection bottleneck due to long capture time or short escape time [130]. As the rate of removal of carriers in the QD G state due to stimulated emission approaches the injection rate between reservoir and QDs, it is possible to deplete the E state carrier population and thus even switch from gain to absorption.

Now, in the presence of a modulated data signal, let us consider the modal gain

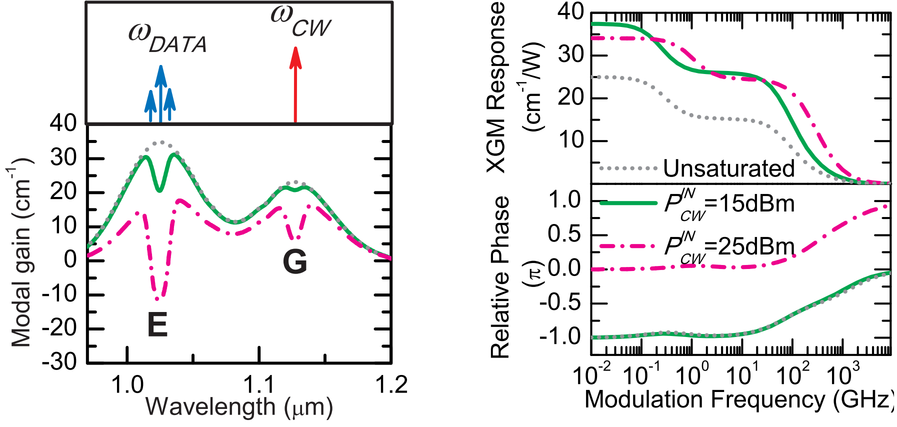

Figure 7.6: Calculated modal gain profile for the up-conversion scheme in QD SOAs at a strong current density (10kA/cm^2) for different input CW power, P^{IN}_{CW}. (Left) Static spectral modal gain. (Right) XGM response and relative phase. Input data signal is set to P^{IN}_{DATA}=1mW with 20% modulation index.

at frequency ω_{CW} in the form of a Fourier series:

$$\bar{g} + \sum_{n=1}^{\infty} \left[|\Delta g_n| \exp(in\Omega t + i\Delta\phi_n) + c.c. \right] /2,$$

Here $\bar{g}$ is the static gain. $|\Delta g_n|$ and $\Delta\phi_n$ are the modulated gain and phase for the nth order harmonics. The modulation index of input data signal (ω_{DATA}) is fixed at 20%. The corresponding higher order harmonics at this modulation index level give relatively small contributions (distortions) to the overall XGM. Hereby, we only keep the first order harmonics. The XGM response $|\Delta g_1|/(P^{IN}_{DATA}m_0)$ and relative phase $\Delta\phi_1$ are shown in Figure 7.6(right). Flat XGM responses approximately up to 100 GHz are observed. Regardless of different optical carriers used for XGM, the corresponding carrier dynamical contributions are similar to what is discussed in section 5.3. As the CW power is modest, the XGM responses in the low modulation frequency range have a phase shift of around $-\pi$ relative to the modulation of the input data signal, which is similar to wavelength conversion with an inverse pattern in the small signal regime [44]. As the CW power is strong and depletes the incoherent gain of E state into absorption, a π-shift of the XGM response is consistent with switching to "non-inverting" cross absorption modulation

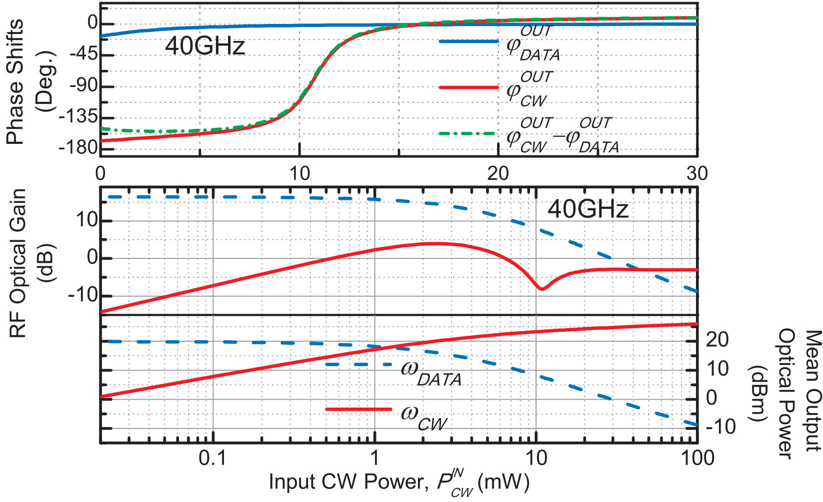

Figure 7.7: Characteristics of the RF output signal at a current of 10 kA/cm^2. (Top) Phase shift. (Bottom) RF optical gain and mean output optical power as a function of input CW power. The input data signal power is 1 mW and has a 20% modulation index at a modulation frequency of 40 GHz.

(XAM) [144]. Thus, by increasing the input CW power, the XGM converted signal experiences the corresponding π-shift and also benefits from the efficient conversion at high modulation frequencies.

Figure 7.7 shows the calculated characteristics of the RF output signal at a modulation frequency of 40 GHz in our wavelength conversion configuration under strong current injection. We fix the input data signal at 1 mW to retain a reasonable signal-to-noise level. Figure 7.7(Top) shows a $\sim$180 degree tunable phase shift φ_{CW}^{OUT} for the XGM converted output by controlling the input probe power. The sharp increase of the phase shift corresponds to the notch-type drop of the XGM efficiency (related to the RF optical gain) seen in Figure 7.7(bottom) at frequency ω_{CW}. By evaluating the mean output optical power in Figure 7.7(bottom), the wavelength conversion in QD SOAs can be divided into two regimes: a small signal regime ($P_{CW}^{OUT} \ll P_{DATA}^{OUT}$) and a two-wave-competing regime (where P_{CW}^{OUT} is comparable to or much larger than P_{DATA}^{OUT}). In the small signal regime, only the data signal dominates the dynamic gain grating and a linear increase of XGM efficiency can be observed. The intensity envelopes of the output data signal and the XGM converted

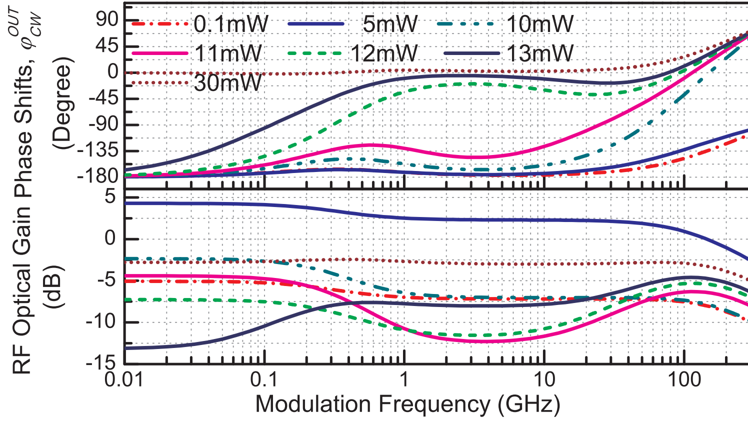

Figure 7.8: Spectral characteristics of the XGM converted output signal for different input CW power at a current density of 10 kA/cm^2. (Top) Phase shift. (Bottom) RF optical gain. The input data signal is 1 mW input with 20% modulation index.

signal are nearly in antiphase (~ -180 degree for $\varphi_{CW}^{OUT} - \varphi_{DATA}^{OUT}$). In the two-wave-competition regime, the dynamic gain gratings depend on the mean power of the spatially varying CW signal. As the stimulated emission at the G state transition reaches the maximum value imposed by the injection bottleneck, the amplifiers can be regarded as being spatially divided into a usual XGM section and an XAM section. Thus the intensity envelope of the XGM signal experiences a π-shift in between these two sections, which results in a notch-type drop in the XGM efficiency and a $\sim$180 degree phase shift.

Figure 7.8 shows the XGM converted output signal as a function of modulation frequency for different input CW power levels. Due to the fast intersubband carrier dynamics between E and G states, the dynamic gain grating (at frequencies ω_{DATA} and ω_{CW}) can balance and follow each other at high speed modulation. It is seen that a shift of π can be achieved by changing the input power from 5 mW to 30 mW for modulation frequencies even beyond 100 GHz. For different modulation frequencies, different input power levels are required to achieve a given phase shift, such as $\pi/4$, $\pi/2$, $3\pi/4$ etc. We also notice that the corresponding RF optical gain changes significantly, which is an undesirable feature. This feature is related to the properties of the dynamic gain grating as a function of modulation frequency shown in Figure 7.6(right). Especially in the two-wave-competition regime, the magnitude

and phase of the XGM response vary for different modulation frequency even for identical mean power. Therefore the cancellation and reconstruction of the XGM converted signal, with a notch-type drop appearance of RF optical gain in Figure 7.7, are sensitive to both modulation frequency and input CW power. In practice, there is a trade-off between the maximum modulation frequency and the minimum signal power to retain a reasonable signal to noise ratio.

In summary, we numerically demonstrated a scheme to realize a $\sim$180 degree broadband RF phase shifter based on high-speed XGM effects under strong injection. The non-equilibrium intra-dot electron relaxations in QD SOAs plays an important role in extending the bandwidth to 100 GHz or even higher. In addition, this configuration allows an alternative way of characterizing ultrafast QD dynamics in between discrete states.

Chapter 8

Optical Pulse Regeneration in QD Devices

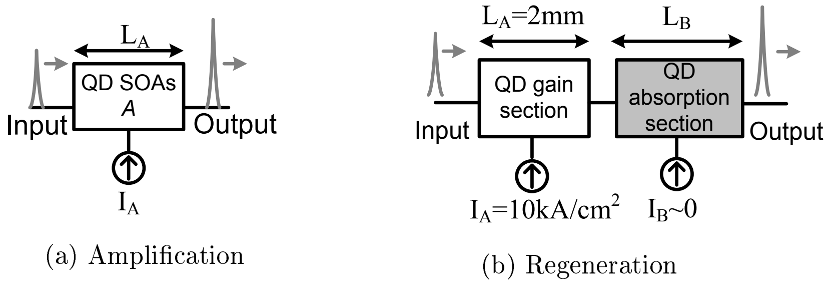

(a) Amplification

(b) Regeneration

Figure 8.1: Schematic diagram of QD waveguide based devices: (a) for amplification; (b) for regeneration.

This chapter presents the numerical simulations of QDs gain dynamics in the presence of picosecond transform-limited Gaussian-shape pulsed signals. The pattern effects are systematically investigated by periodic pulse train with various time spacing. And then we discuss the possibility of realizing an all-optical regenerator by incorporating a QD absorber section in an amplifier structure at bit rates up to 100 Gb/s. Here, the theoretical investigations are based on the time domain implementation of our MPREM model presented in Chapter 4. The treatment focuses on the gain dynamics corresponding to the lowest discrete QD states, i.e., the ground (G) states. The amplification and regeneration properties are quantified by the

ratio between the output and input pulse energy. Further topics, e.g., two photon absorption, pulse shape distortion, phase dynamics and dispersive propagation effect, are not considered. Gaussian homogeneous lineshape is used. The parameters are given in Appendix F.

Figure 8.1 schematically shows the QD waveguide devices we investigated. Figure 8.1(a) shows a QD gain section with length L_A under forward-bias injection current I_A, referred to as QD SOAs. Figure 8.1(b) shows our QD device configuration for regeneration of pulsed signals by incorporating a QD absorber section with length L_B in an amplifier structure, which is also close to the analysis of pulse shaping per pass in mode-locked lasers [145].

8.1 Amplification of Pulsed Signals

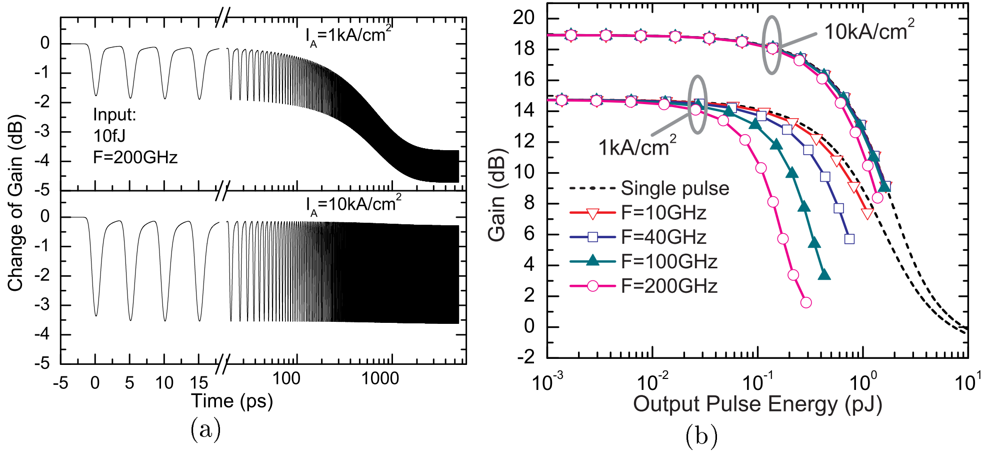

Figure 8.2: Amplification of 1ps pulsed signals in a QD SOAs (L_A=2 mm). (a) Calculated temporal gain variation of a QD SOAs (L_A=2 mm) at the injection current density of (top) 1 kA/cm^2 and (bottom) 10 kA/cm^2. (b) Steady gain vs. output pulse energy in a single QD gain section for amplification of periodic pulses at different repetition frequency, F, up to 200 GHz. Optical carrier frequency of pulsed signals are @ω_G.

Figure 8.2 shows the amplification results of 1ps pulsed signals in QD SOAs. Figure 8.2(a) shows an example of the calculated temporal variation of the gain change at different current densities. Here we used pulses with energy of 10 fJ at

repetition frequency 200 GHz starting from time '0'. The fast gain recovery corresponding to the first four pulses is due to the fast intra-dot relaxations between the ground and excited states. Due to the large contrast between electron scattering rates, the ground (G) states are refilled mainly via intra-dot relaxation from excited (E) states. As the following pulses continue to deplete carriers at the lowest QD states due to stimulated emission, first the excited states and then the reservoir carrier densities will be adjusted by different fast refilling mechanisms. Then the total carrier density becomes stabilized after several nanoseconds (longer than reservoir carrier lifetime) and determines the steady G state gain responses. At a weak injection current (1 kA/cm^2), the total carrier density is relatively difficult to be resupplied. Thus the G state gain starts to decline after tens of picoseconds and then approaches to a steady value after several nanoseconds, which is distinctively different from the single pulse response at time '0'. As the total carrier density decreases towards the transparency point, the differential gain increases and thus the saturation energy decreases. The nonlinear gain term induced by the ultrafast capture process makes the saturation energy decrease as the pulse width is shortened [146, 147]. At a strong injection current (10 kA/cm^2), the total carrier density is much more difficult to deplete and thus the ground state gain is only slightly changed. The gain recovery with the dependence on the injection current is consistent with the experimental pump probe observations [34].

Figure 8.2(b) shows the periodic pulse train amplification results of a QD gain section with a maximum small signal gain (~19 dB). The single pulse amplification is illustrated (dashed line). The gain saturation for the single pulse, which is much shorter than the carrier lifetime τ_s, is limited by the QD inter-subband relaxation times [131]. For pulse trains at a repetition frequency of 10 GHz, the gain recovery in the QDs is fast enough to achieve pJ output pulse energies without significant deviation of the gain from the single pulse case. As the repetition frequency increases to 200 GHz, only 20 fJ output pulse energies can be achieved for patterning free performance at the injection current density of 1 kA/cm^2. As the injection current density increases from 1 kA/cm^2 to 10 kA/cm^2, patterning effects at high bit rates, up to 200 Gb/s, with sub-pJ output pulse energies can be significantly suppressed.

8.2 Regeneration of Pulsed Signals

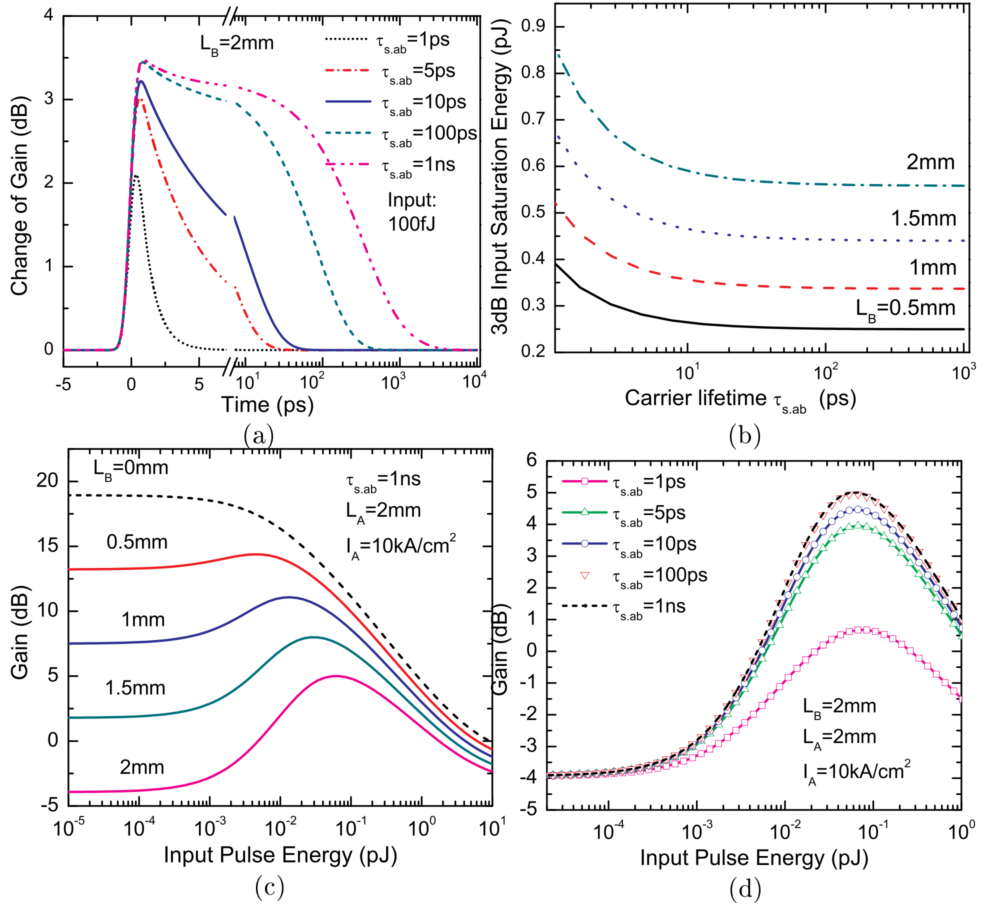

Figure 8.3: Regeneration of 1 ps single pulse in QD devices by incorporating a QD absorber section in an amplifier structure (L_A=2 mm, I_A=10 kA/cm^2) . a) Calculated temporal variation of the gain change and b) 3dB input saturation energy in a QD absorption section with different carrier lifetimes $\tau_{s,ab}$. Gain vs. input pulse energy in a QD gain section cascaded with c) a slow ($\tau_{s,ab}$=1 ns) absorption section with different device lengths L_B; d) an absorption section (fixed length L_B=2 mm) with different carrier lifetimes.

One of the biggest challenges here is how to properly simulate the absorption dynamics in a QD electro-absorber. Weak quantum-confined stark effect (QCSE)

and low absorption saturation energy have been observed in InGaAs QD under reverse biased voltage, whereas a reverse bias can be applied to reduce the QD absorber recovery time by introducing a sweep-out mechanism for carriers without increasing the absorber loss [148]. A rate equation model of reverse biased QD saturable absorbers have been used in the dynamic simulation and optimization of mode-locked QD lasers [149]. For simplicity, we still use our MPREM model to approximate the QD absorption recovery by using different absorber carrier lifetimes $\tau_{s,ab}$ (corresponding to the ground states transition [1]) scaling from 1 ns down to 1 ps. The other parameters are the same as the ones for the gain section. The intention is to verify the 2R regeneration with patterning free performance (above 10 Gb/s) in such QD structures, which make them superior to the bulk and QW counterparts [84, 85]. Figure 8.3(a) shows an example of the calculated temporal variation of the gain change in a QD absorber section, which approximates the ultrafast QD electroabsorption dynamics [148, 149]. As seen in Figure 8.3(b), the 3dB input saturation energy of the QD absorber for 1 ps pulses can be increased by shortening the carrier lifetime or propagating through a longer absorber.

Figure 8.3(c) shows the nonlinear amplification of a single pulse through a QD gain section cascaded with a slow ($\tau_{s,ab}$=1 ns) QD absorption section with different length L_B. Here we keep the high injection current density 10 kA/cm^2 to enable ultrafast gain recovery in the QD gain section with fixed length (L_A=2 mm) for patterning free amplification at high frequencies. Due to the difference between the saturation properties of QDs in the gain and absorption regime, we can realize 2R-regeneration for pulsed signals with the additional absorption section. Although this "bandpass"-like transfer function is non-ideal, it still suppresses the gain at low pulse energy levels while keeping the similar limiting amplification profile of the QD SOAs at high pulse energy levels. For example, $\sim$9 dB net regeneration, given by the net gain contrast between low and high input pulse energy, can be achieved for a single pulse in case of a long absorption section (L_B=2 mm). The net regeneration depends on the difference between the 3dB output saturation energy of the gain section and 3dB input saturation energy of the absorption section as well as the small signal device gain/absorption for 1ps pulse.

[1] $\tau_{s,ab}$ is used to replace the ground state spontaneous time τ_{spon} in Eq. (4.7). Meanwhile the excited state spontaneous lifetime and carrier lifetime in reservoir are also scaled down with the same ratio.

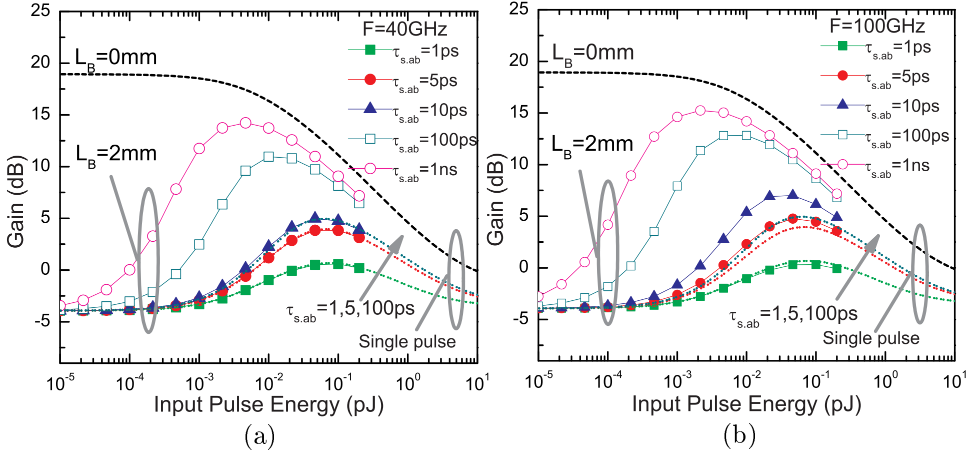

Figure 8.4: Regeneration of 1 ps periodic pulsed signals in a QD gain section (L_A=2 mm, I_A=10 kA/cm^2) cascaded with a QD absorption section. Different carrier lifetime $\tau_{s,ab}$ for absorption section has been used. Pulsed signals are at different repetition frequencies F. (a): 40 GHz. (b): 100 GHz. Dotted lines indicate single pulse results with different absorption carrier lifetime as in Fig. 8.3(d).

Figure 8.3(d) shows that decreasing the carrier lifetime from 1ns down to 1ps in the absorption section $\tau_{s,ab}$ reduces the net regeneration without shifting the operational pulse energy in such structures. When the pulse width τ_p is much shorter than $\tau_{s,ab}$, the absorption recovery is not fast enough to make a response to the pulse. But for pulses longer than or comparable to $\tau_{s,ab}$, there is a partial recovery during the pulse width. The 3dB input saturation energy of the absorption section can be increased by decreasing the carrier lifetime with fixed small signal device absorption.

Figure 8.4 shows results of the periodic 1 ps pulsed signals for the regenerator structure shown in Figure 8.1(b). Comparing with the single pulse case as in Figure 8.3(d), the regeneration of a pulse train at a repetition frequency F of 40 GHz or 100 GHz results in a large deviation, which degrades the high-speed patterning free performance of QD SOAs as in Figure 8.2(b). This bottleneck is severe in the case of slow absorption recovery in the absorption section, when the carrier lifetime $\tau_{s,ab}$ is longer than the inverse of the repetition frequency. We investigated the role of the absorber lifetime, $\tau_{s,ab}$, by decreasing its value from 1 ns to 1 ps, which effectively speeds up the absorption recovery and leads to small gain deviation from the

single pulse case. By increasing the repetition frequency from 40 GHz to 100 GHz, patterning free regeneration requires shorter absorption carrier lifetime at the expense of smaller net regeneration. As long as the absorption recovery is fast enough ($\tau_{s,ab}<$ 5 ps), the single pulse regeneration can provide a good estimation to high speed regeneration at a frequency close to 100 GHz.

8.3 Summary

Numerical simulations based on the QD carrier dynamics for picosecond pulsed signals have shown that the strong current injection enables high-speed amplification in QD SOAs and a fast integrated QD absorber enables high-speed 2R regeneration by shortening the carrier lifetime at the expense of lowering the net regeneration. Our simulations suggest that the use of QDs instead of bulk or QW materials is a positive solution to overcome degradation due to the pattern effects in the concatenated regenerator structures.

Chapter 9

Conclusions

This thesis has considered some properties and potential applications of quantum dot devices, i.e., QD SOAs, through a systematic numerical simulation and theoretical analysis of carrier dynamics.

The basis for the theoretical work has been described in the beginning of the thesis. Start with the semiclassical density matrix equations in the simplest two-level system, the adiabatic approximation assumptions and limitations of carrier rate equations are presented. We present a detailed quantum dot semiconductor optical amplifier model incorporating a carrier dynamics rate equation model for quantum dots with inhomogeneous broadening as well as equations describing propagation. A phenomenological balanced scattering description has been used to model the intradot electron scattering between discrete quantum dot states and the continuum. A local carrier density description has been used to model the hole scattering as in the continuum.

The basic properties of quantum dot devices are investigated. The QDs linear gain and refractive index changes are modeled only based on the interband transition contributions. It is argued that different interband transition contributions can lead to a large variety of linewidth enhancement factor (α-factor). As a consequence, our simulations for QD SOAs are limited in gain dynamics only. The QD gain saturation at the low injection current is found to be limited by total carrier density depletion. As the injection current increases, the total carrier density depletion is suppressed and dominated by the intra-dot carrier relaxation. For example, for the optical

frequency corresponding to the lowest QD states, a large saturation power around 20 dBm is predicted at high current densities.

Additional to the time domain implementation, an efficient semi-analytical approach is employed based on a microscopic footing. The small-signal medium response of inhomogeneously broadened QDs in the presence of an intensity modulated optical signal is investigated. Distinct oscillation contributions from electrons and holes are shown to be determined by the corresponding carrier dynamical processes. The electron intra-dot relaxation contributes to the corresponding coherent gain responses, also referred to as the dynamic gain grating, ranging from 10 to 100 GHz or higher. The variations of the modulation response and relative phase strongly depend on the input power and injection current density. The high-speed performance can be enhanced by increasing the input power or the injection current density, which is one of the interesting properties for nonlinear optical applications.

We have theoretically investigated the physical effects of CPO that contribute to microwave phase shifts in semiconductor optical waveguides using a general SOA carrier density pulsation model. In particular, the influence of optical filtering is analyzed. When optical filtering is included to selectively suppress a sideband of the optical signal before photodetection, the refractive index grating becomes important and leads to the observation of both phase delay and phase advance. The strength of the refractive index grating is quantified by the α-factor, which means that the influence of optical filtering can be increased significantly in QW and bulk devices, while QD devices with low α-factor are expected to show a smaller influence from filtering. Vice versa, our optical filtering scheme can be implemented as a standard experimental approach to distinguish whether or not all the available QD SOAs has a non-zero bulk-like α-factor, which will be important experimental arguments in the relevant debates. A large phase shift is achievable at higher modulation frequencies with a moderate small signal device gain when properly exploiting optical filtering. The theoretical results agree with the experimental values. The phase shifting effect induced by optical filtering is qualitatively explained by a simple perturbation approach. This approximate approach provides a simple physical explanation of the large difference, seen in both experiments and numerical simulations, between filtering the red and the blue modulation sideband.

For QD SOAs, the phase shifting has been simulated based on gain dynamics

with zero α-factor. A tunable RF phase shifter based on CPO effects (dynamic gain grating) can be achieved at the modulation frequencies, i.e., 30-100 GHz, much higher than the inverse of the carrier lifetime. This effect is explained as a result of nonequilibrium effects in QDs and highlights the importance of the intra-dot electron scattering processes. The magnitude of tunable phase shift can be possible enhanced by employing the idea of cascading and optical filtering. Another potential scheme based on XGM effects has also been investigated. $\sim$180 degree phase shifting is achieved over a broad bandwidth up to 100 GHz or even higher.

Finally, we have also investigate the gain dynamics of QD SOAs in the presence of picosecond pulsed signals, in particular the steady gain response to a periodic pulse trains with various time period. Our model predicts a high speed patterning free amplification up to 150-200 GHz in QD SOAs by increasing injection current. The fast gain recovery are benefitted from the ultrafast intra-dot relaxations between discrete QD states. The patterning effects induced by total carrier density depletion are greatly alleviated by the strong current injection. The QD absorber is schematically modeled by altering an effective absorber carrier lifetime. The possibility to realize a compact high-speed all-optical regenerator by incorporating a quantum dot absorption section in an amplifier structure has been discussed. By decreasing the absorber carrier lifetime, the speed performance is enhanced at the expense of lowering the net regeneration.

The future of QD Devices is pending on the progress in both theory and experiment, especially high-quality fabrications. Nowadays, the physics insight of QDs is still quite limited and most of the experimental results are justified by implementing heuristically approximated models, including the work in this thesis. Nevertheless, I hope that my work is to be one of the many paving stones on the road towards the promising future.

Appendix A

Propagation Effects in Semiconductor Waveguide

In this appendix, we briefly discuss different levels of approximations in describing propagation effects in semiconductor waveguide.

In a practical semiconductor waveguide, the evolution of the complex electric field along the propagation direction is described in the framework of Maxwell-Bloch equations [92]. Like all the electromagnetic phenomena, the optical propagation in semiconductor waveguide is governed by Maxwell's equations [150]. For optical waveguiding structures with small transverse inhomogeneities of the medium polarization [96], the three dimensional scalar wave equation can be written as [151, 152, 153]:

$$\left(\nabla_z^2 + \nabla_\perp^2\right) \mathbf{E}(\mathbf{r}, t) - \frac{1}{c^2} \partial_t^2 \mathbf{E}(\mathbf{r}, t) = \mu_0 \partial_t^2 \mathbf{P}_b(\mathbf{r}, t) + \mu_0 \partial_t^2 \mathbf{P}(\mathbf{r}, t) \tag{A.1}$$

where $\nabla_\perp^2$ is the transversal Laplace operator, c is the speed of light in vacuum satisfying $1/c^2 = \mu_0 \epsilon_0$ with vacuum permittivity ϵ_0 and permeability μ_0. $\mathbf{r}$ is the 3D spatial vector. The electric field $\mathbf{E}$ propagates along the z direction. $\mathbf{P}_b$ is the material polarization induced by the background (linear effect). $\mathbf{P}$ is material polarization induced from medium response (typically including linear and third-order nonlinear effects),which are defined as:

$$\mathbf{P}_b(\mathbf{r}, t) \quad = \quad \epsilon_0 \int_{-\infty}^{t} \chi_b(\mathbf{r}, t - t') \mathbf{E}(\mathbf{r}, t') dt' \tag{A.2}$$

$$\begin{aligned}\mathbf{P}(\mathbf{r},t) &= \epsilon_0\int_{-\infty}^{t}\chi^{(1)}(\mathbf{r},t-t')\mathbf{E}(\mathbf{r},t')dt' \\ &+\epsilon_0\int_{-\infty}^{t}\int_{-\infty}^{t}\int_{-\infty}^{t}\chi^{(3)}(\mathbf{r},t-t_1,t-t_2,t-t_3)\vdots \\ &\times\mathbf{E}(\mathbf{r},t_1)\mathbf{E}(\mathbf{r},t_2)\mathbf{E}(\mathbf{r},t_3)dt_1dt_2dt_3 \qquad \text{(A.3)}\end{aligned}$$

These relations are valid in the electric-dipole approximation and assume that the medium response is local. χ_b is the background linear susceptibility. $\chi^{(1)}$ and $\chi^{(3)}$ are the linear and third-order susceptibility of the medium response [1].

The time and spectral representation of the linear susceptibility satisfies a simple relation as:

$$\chi^{(1)}(\mathbf{r},t)=\frac{1}{2\pi}\int_{-\infty}^{\infty}d\omega\chi^{(1)}(\mathbf{r},\omega)e^{-i\omega t}$$

As the usual treatment in nonlinear optics [151, 152], a slowly varying envelope approximation $\mathbf{E}=A(z,t)F(\mathbf{r}_\perp)e^{i(\beta_0 z-\omega_0 t)}$ is introduced. $A(z,t)$ is the slowly varying envelope along the propagation direction with the wave number $\beta_0=\omega_0 n_0/c$, n_0 is the refractive index at optical carrier frequency ω_0. $F(\mathbf{r}_\perp)$ is the transversal field distribution profile.

Quite often in a passive waveguide structure, the 3D wave equation is often approximated as a monochromatic wave problem and decoupled into two independent parts according to the spatial coordinates :

$$\begin{cases}\left[\nabla_\perp^2+\epsilon_b(\mathbf{r}_\perp,\omega)k_0^2-\beta_{eff}^2\right]F(\mathbf{r}_\perp)=0 \\ \left[2i\beta_0\partial_z+(\beta_{eff}^2-\beta_0^2)\right]A(z)=0\end{cases} \qquad \text{(A.4)}$$

where the background dielectric constant $\epsilon_b(\mathbf{r}_\perp,\omega)=1+\chi_b(\mathbf{r}_\perp,\omega)$. β_{eff} is the effective wave number. The transversal 2D eigenvalue equation determines the transverse mode profile $F(\mathbf{r}_\perp)$ and the 1D propagation equation determines the evolution of electric field envelope along the propagation direction z. By expanding $\beta_{eff}(\omega)$ in a Taylor series about the carrier frequency ω_0 as:

$$\beta_{eff}(\omega)=\beta_0+(\omega-\omega_0)\beta_1+\frac{1}{2}(\omega-\omega_0)^2\beta_2+\frac{1}{6}(\omega-\omega_0)^3\beta_3+\cdots$$

[1] We should be aware of the fact that the susceptibilities $\chi^{(1)}(\mathbf{r})$ and $\chi^{(3)}(\mathbf{r})$ used here are effective notations of the one in Eq. (3.6) with the complex summations over the momentum vector $\mathbf{k}$.

where

$$\beta_m = \left(\frac{d^m \beta_{eff}}{d\omega^m} \right)_{\omega=\omega_0} \qquad (m = 1, 2, \cdots)$$

The corresponding dispersion operator is:

$$\hat{D} = \beta_0 + \sum_{m=1}^{\infty} \beta_m (i\partial_t)^m$$

The propagation equation are often derived into a form of nonlinear Schrödinger equation [151] for the field envelope:

$$\frac{\partial A}{\partial z} = i \left[\hat{D} - \beta_0 + \hat{N}(A) \right] A(z,t) \tag{A.5}$$

where $\hat{N}(A) = k_0 n_{kerr} |A|^2$ is the nonlinear operator used to describe the kerr effects, n_{kerr} is nonlinear kerr coefficient. More general derivations [96, 154] have been developed to refine the dispersion properties especially for ultrashort pulse propagation.

In active semiconductor waveguide structures, by treating the medium response as a perturbation, which does not affect the transverse field distribution, the corresponding slowly varying material polarization $B(z,t)$ induced by the the material response can be approximated as:

$$\mathbf{P}(\mathbf{r},t) \approx \Gamma B(z,t) F(\mathbf{r}_\perp) e^{i(\beta_0 z - \omega_0 t)} \tag{A.6}$$

where Γ is defined as the overlap of the transverse optical mode distribution and the active region,

$$\Gamma = \frac{\int_{active} |F(\mathbf{r}_\perp)|^2 d\mathbf{r}_\perp}{\int_{-\infty}^{+\infty} |F(\mathbf{r}_\perp)|^2 d\mathbf{r}_\perp} \tag{A.7}$$

Notice that this confinement factor only provides a rough estimation of the linear optical effects [155], the corresponding confinement factor for the third-order effects can be defined in a similar form as:

$$\Gamma^{(3)} = \frac{\int_{active} |F(\mathbf{r}_\perp)|^4 d\mathbf{r}_\perp}{\int_{-\infty}^{+\infty} |F(\mathbf{r}_\perp)|^2 d\mathbf{r}_\perp} \tag{A.8}$$

Thus a refined representation [156] of slow varying linear and third-order material polarization, $B^{(1)}(z,t)$ and $B^{(3)}(z,t)$ can also be used as following:

$$\mathbf{P}(\mathbf{r},t) \approx \left[\Gamma B^{(1)}(z,t) + \Gamma^{(3)} B^{(3)}(z,t) \right] F(\mathbf{r}_\perp) e^{i(\beta_0 z - \omega_0 t)} \tag{A.9}$$

The additional treatment to the third-order confinement factor has been well-understood in the multi-mode laser dynamics theory [157, 90], where a more general spatial mode function can be used to evaluate the high-order interactions between multi modes and the semiconductor medium. For the comprehensive carrier dynamical system typically with many-body effects or even quantum kinetic descriptions, such transverse field effects are often intentionally neglected to reduce computational complexity [46]. While the laser dynamics theory is further simplified for narrow band single mode operation with an plane wave form as $A(z,t)e^{i(\beta_0 z - \omega_0 t)}$, such approximation is still not changed. In recent literature for simulations of semiconductor optical amplifier, the third-order confinement factor $\Gamma^{(3)}$ is mostly replaced by the linear confinement factor Γ. Normally for the condition $\Gamma > \Gamma^{(3)}$, this substitution leads to an overestimation of the third-order effect induced by the carrier dynamics.

In this thesis, we focus on solving the 1D optical propagation problem of the electric field envelope with much smaller computational efforts than the complete set of Maxwell's equations. Similar to derivation of the nonlinear schrödinger equation Eq.(A.5), we have:

$$\begin{aligned} \frac{\partial A(z,t)}{\partial z} &= -\frac{\alpha_{int}}{2} A(z,t) + i\left[\hat{D} - \beta_0\right] A(z,t) \\ &+ i\left[k_0 n_{kerr} + i\frac{\beta_{TPA}}{2}\right] |A|^2 A(z,t) \\ &+ i\frac{\beta_0}{2n_0^2\epsilon_0}\Gamma B(z,t) \end{aligned} \tag{A.10}$$

α_{int} is internal loss. $\hat{D} - \beta_0$ is the background dispersion operator as in a passive waveguide. n_{kerr} is the Kerr coefficient, β_{TPA} is the two photon absorption (TPA) coefficient. $B(z,t)$ is the summation of all the linear and third-order effects of medium responses, which are solved from the dimensionless density matrix equations and its approximation forms.

In reality, the dispersion effect in a short semiconductor waveguide is relatively weak. For example, using group velocity dispersion values $-\lambda\frac{\partial^2 n_{eff}}{\partial \lambda^2} = -0.63\ \mu\text{m}^{-1}$ [158], the corresponding characteristic dispersion length $L_D = \tau_p^2/\beta_2$ =8.98 mm is calculated for an ultrashort pulse with FWHM width τ_p=150 fs. Such characteristic dispersion length is much longer than the device length used in practice, e.g., 0.3-0.5 mm. So the dispersion operator $\hat{D} - \beta_0$ is often neglected. The two photon

absorption and Kerr effects contributed from different materials in the waveguiding region, can be weighted with the corresponding confinement factors [132].

Notice that Eq. (A.10) can still keep track of the detailed microscopic polarizations from different states. However, it is complex in computation as well as notation for most simulations of semiconductor devices with a narrow signal spectral bandwidth (well within adiabatic approximation limit).

As a consequence, at the monochromatic wave limit, gain coefficient g and linewidth enhancement factor α from the linear susceptibility with respect to carrier density N have been defined [159]:

$$\begin{aligned} i\frac{\beta_0}{2n_0^2\epsilon_0}\Gamma B(z,\omega_0) &= i\frac{\beta_0}{2n_0^2}\Gamma\chi(z,\omega_0)A(z,\omega_0) \\ &\Rightarrow \Gamma\frac{g(\omega_0)}{2}(1-i\alpha)A(z,\omega_0) \end{aligned} \tag{A.11}$$

where

$$\begin{cases} \chi(\omega_0) = \chi_r + i\chi_i \\ g(\omega_0) = -\frac{\omega_0}{cn_0}\chi_i \\ \alpha = \frac{\partial\chi_r}{\partial N} / \frac{\partial\chi_i}{\partial N} \end{cases} \tag{A.12}$$

Following the adiabatic approximation for the rate equations, we obtain the approximated medium response as:

$$i\frac{\beta_0}{2n_0^2\epsilon_0}\Gamma B(z,t) \approx i\frac{\beta_0}{2n_0^2}\Gamma\chi(z,t)A(z,t) = \Gamma\frac{g(t)}{2}(1-i\alpha)A(z,t) \tag{A.13}$$

The propagation equation of the field envelope can be simplified as:

$$\frac{\partial A(z,t)}{\partial z} = -\frac{\alpha_{int}A(z,t)}{2} + \Gamma\frac{g(z,t)A(z,t)}{2}(1-i\alpha) \tag{A.14}$$

The corresponding propagation equation of the optical intensity,

$$P(z,t) = \frac{n_0 c\epsilon_0\omega_0^2}{2}A(z,t)^2,$$

has s simple form as:

$$\frac{\partial P(z,t)}{\partial z} = \left[\Gamma g(z,t) - \alpha_{int}\right]P(z,t) \tag{A.15}$$

Hereby, optical intensity propagation equation is the simplest way to estimate the gain dynamics with propagation effects based on the footing of the adiabatic approximation.

Appendix B

Derivations of Small-Signal Harmonic Analysis

B.1 General Formulism in a Two-level System

This appendix presents the derivation of the small-signal harmonic analysis for the density matrix equation and the corresponding carrier rate equation approximations in a simple two-level system.

Based on the principle of small-signal analysis, we assume that the steady slow-varying envelope solution of all variables in the density matrix equations for the two level system of state k, $n_c^k(t)$, $n_v^k(t)$, p_{cv}^k and $A(t)$, can be well approximated by a Fourier series expansion with finite orders of harmonics ($m = 0, \pm 1, ..., \pm M$):

$$y(t) = \sum_{m=-M}^{M} y_m e^{-im\Delta\Omega t} \tag{B.1}$$

where $y_m^* = y_{-m}$ is satisfied for $y(t)$ with real values.

By substituting the Fourier series expansions into the spectral solution of Eq.(3.14), we have:

$$p_{cv,m}^k = \frac{d_k}{\hbar} L_k(\omega_0 + m\Delta\Omega) \times \left\{ \sum_{m_1} 2n_{\alpha,m_1}^k A_{m-m_1} - A_m \right\} \tag{B.2}$$

and the generation rate as:

$$R_{stim,m}^k = \frac{i}{\hbar} \left\{ d_k^* \sum_{m_1} p_{cv,m_1}^k A_{m_1-m}^* - d_k \sum_{m_1} p_{cv,m_1}^{k*} A_{m+m_1} \right\} \tag{B.3}$$

Let us form the variables' Fourier series into $(2M+1) \times 1$ column vector as:

$$\mathbf{p}_{cv}^{k} = [p_{cv,-M}^{k}, ..., p_{cv,0}^{k}, ..., p_{cv,M}^{k}]^T \tag{B.4}$$

$$\mathbf{n}_{\alpha}^{k} = [n_{\alpha,-M}^{k}, ..., n_{\alpha,0}^{k}, ..., n_{\alpha,M}^{k}]^T \tag{B.5}$$

and rearrange Eq. (3.8) and (3.9) into a set of linear matrix equations for Fourier series of each harmonics as:

$$\underbrace{\begin{pmatrix} \mathbb{X}_{pp} & \mathbb{X}_{pn} & 0 & 0 \\ \mathbb{X}_{np} & \mathbb{X}_{nn} & 0 & \mathbb{X}_{np^*} \\ \mathbb{X}_{n^*p} & 0 & \mathbb{X}_{n^*n^*} & \mathbb{X}_{n^*p^*} \\ 0 & 0 & \mathbb{X}_{p^*n^*} & \mathbb{X}_{p^*p^*} \end{pmatrix}}_{\mathbb{X}} \cdot \underbrace{\begin{pmatrix} \mathbf{p}_{cv}^{k} \\ \mathbf{n}_{\alpha}^{k} \\ (\mathbf{n}_{\alpha}^{k})^* \\ (\mathbf{p}_{cv}^{k})^* \end{pmatrix}}_{\mathbf{y}} = \underbrace{\begin{pmatrix} \mathbf{b}_p \\ \mathbf{b}_n \\ (\mathbf{b}_n)^* \\ (\mathbf{b}_p)^* \end{pmatrix}}_{\mathbf{b}} \tag{B.6}$$

where the $(2M+1) \times (2M+1)$ block matrixes satisfy the following relations:

$$\mathbb{X}_{pn} \Rightarrow -2\sum_{m}\sum_{m_1} \frac{d_k}{\hbar} L_k(\omega_0 + m\Delta\Omega) A_{m-m_1} \tag{B.7}$$

$$\mathbb{X}_{np} \Rightarrow \sum_{m}\sum_{m_1} \frac{i}{\hbar} d_k^* A_{m_1-m}^* \tag{B.8}$$

$$\mathbb{X}_{np^*} \Rightarrow -\sum_{m}\sum_{m_1} \frac{i}{\hbar} d_k A_{m+m_1} \tag{B.9}$$

$$\mathbb{X}_{nn} \Rightarrow \sum_{m}(-im\Delta\Omega) + \sum_{m} \gamma_{\alpha}^{k} \tag{B.10}$$

here block matrix $\mathbb{X}_{pn}$ indicates the impact of occupation probability to polarization $(n \to p)$ and represents the summation (convolution matrix) relation in Eq. (B.2). $\mathbb{X}_{np}$ and $\mathbb{X}_{np^*}$ indicates the impact of polarization probability to occupation probability $(p, p^* \to n)$ and represents the summation (convolution matrix) relation in Eq. (B.3). $\mathbb{X}_{nn}$ indicates the temporal-differential and phenomenological relaxation terms of occupation probability. $\mathbb{X}_{pp} = \mathbb{X}_{p^*p^*}$ is an simply identity matrix. The rest of block matrixes are the corresponding conjugate representation as:

$$\mathbb{X}_{p^*n^*} \equiv (\mathbb{X}_{pn})^* \quad , \quad \mathbb{X}_{n^*p^*} \equiv (\mathbb{X}_{np})^*$$

$$\mathbb{X}_{n^*p} \equiv (\mathbb{X}_{np^*})^* \quad , \quad \mathbb{X}_{n^*n^*} \equiv (\mathbb{X}_{nn})^*$$

And $(2M+1) \times 1$ stimulus vector $\mathbf{b}_p$ indicates the interaction between electric field and the empty state k. $\mathbf{b}_n$ indicates the equilibrium terms in the phenomenological relaxation processes. The stimulus vectors are in the form:

$$\mathbf{b}_p \Rightarrow \underbrace{[..., -\frac{d_k}{\hbar} L_k(\omega_0 + m\Delta\Omega) A_m, ...]^T}_{2M+1} \tag{B.11}$$

$$\mathbf{b}_n \Rightarrow \gamma_\alpha^k n_\alpha^{k,eq} [\underbrace{0, ..., 0}_{M}, 1, \underbrace{0, ..., 0}_{M}]^T \tag{B.12}$$

For linear matrix equations as $\mathbb{X}\mathbf{y} = \mathbf{b}$, the solution can be easily solved by simple linear algebra.

Following the discussion in previous section, the adiabatic approximation replaces all the $L_k(\omega_0 + m\Delta\Omega)$ with a constant $L_k(\omega_0)$.

While the semi-adiabatic approximation replace the matrix form Eq.(B.7) as:

$$\mathbb{X}_{pn} \Rightarrow -2 \sum_m \sum_{m_1} \frac{d_k}{\hbar} L_k(\omega_0 + (m - m_1)\Delta\Omega) A_{m-m_1} \tag{B.13}$$

For more complex carrier or even energy phenomenological relaxations involving nonlinear relations between occupation probabilities, it is still possible to get the solutions by using numerical iteration method.

B.2 First-order Derivations in QDs

This appendix presents a semi-analytical approach to solve the first-order small-signal harmonic solutions of the QD multi-population rate equations, including Eq. (4.6), (4.7), (4.13), (4.15) and (4.16).

For a weakly, harmonically modulated optical signal:

$$P_p(t) = \bar{P}_p + (\widetilde{\Delta P_p} e^{-i\Omega t} + c.c.)/2$$

The corresponding first-order perturbation over different carrier densities in the

conduction band:

$$N_R = \bar{N}_R + \left(\widetilde{\Delta N_R} e^{-i\Omega t} + c.c.\right)/2 \tag{B.14}$$

$$\begin{aligned} N_E^i &= \bar{N}_E^i + \left(\widetilde{\Delta N_E^i} e^{-i\Omega t} + c.c\right)/2 \\ &= \frac{\varepsilon_E}{V_0}\left[\bar{f}_E^i + \left(\widetilde{\Delta f_E^i} e^{-i\Omega t} + c.c\right)/2\right] \end{aligned} \tag{B.15}$$

$$\begin{aligned} N_G^i &= \bar{N}_G^i + \left(\widetilde{\Delta N_G^i} e^{-i\Omega t} + c.c\right)/2 \\ &= \frac{\varepsilon_G}{V_0}\left[\bar{f}_G^i + \left(\widetilde{\Delta f_G^i} e^{-i\Omega t} + c.c\right)/2\right] \end{aligned} \tag{B.16}$$

where $\bar{N}_R$, $\bar{N}_E^i$, $\bar{N}_G^i$ are the CW part of solutions. $\widetilde{\Delta N_R}$, $\widetilde{\Delta N_W}$, $\widetilde{\Delta N_B}$ are the corresponding complex amplitude of modulation. We also assume the common conduction band quasi-fermi level $E_{f,c}$ in the reservoir and occupation probability of WL f_w oscillates in the form:

$$E_{f,c} = \bar{E}_{f,c} + \left(\widetilde{\Delta E_{f,c}} e^{-i\Omega t} + c.c\right)/2, \tag{B.17}$$

$$f_w = \bar{f}_w + \left(\widetilde{\Delta f_w} e^{-i\Omega t} + c.c\right)/2 \tag{B.18}$$

where

$$\widetilde{\Delta N_R} = \left(\left.\frac{\partial N_W}{\partial E_{f,c}}\right|_{\bar{E}_{f,c}} + \left.\frac{\partial N_B}{\partial E_{f,c}}\right|_{\bar{E}_{f,c}}\right)\widetilde{\Delta E_{f,c}} \tag{B.19}$$

$$\widetilde{\Delta f_w} = \left.\frac{\partial f_W}{\partial E_{f,c}}\right|_{\bar{E}_{f,c}} \widetilde{\Delta E_{f,c}} \tag{B.20}$$

First-order perturbation of valence band QD carrier densities can be defined in a similar form as Eq. (B.15) and (B.16).

$$\begin{aligned} N_{E,v}^i &= \bar{N}_{E,v}^i + \left(\widetilde{\Delta N_{E,v}^i} e^{-i\Omega t} + c.c\right)/2 \\ &= \frac{\varepsilon_E}{V_0}\left[\bar{f}_{E,v}^i + \left(\widetilde{\Delta f_{E,v}^i} e^{-i\Omega t} + c.c\right)/2\right], \end{aligned} \tag{B.21}$$

$$\begin{aligned} N_{G,v}^i &= \bar{N}_{G,v}^i + \left(\widetilde{\Delta N_{G,v}^i} e^{-i\Omega t} + c.c\right)/2 \\ &= \frac{\varepsilon_G}{V_0}\left[\bar{f}_{G,v}^i + \left(\widetilde{\Delta f_{G,v}^i} e^{-i\Omega t} + c.c\right)/2\right], \end{aligned} \tag{B.22}$$

The corresponding valence band quasi-equilibrium quantities are:

$$\begin{aligned} N_{E,v}^{i,eq} &= \bar{N}_{E,v}^{i,eq} + \left(\Delta N_{E,v}^{i,eq} e^{-i\Omega t} + c.c\right)/2 \\ &= \frac{\varepsilon_E}{V_0}\left[\bar{f}_{E,v}^{i,eq} + \left(\widetilde{\Delta f_{E,v}^{i,eq}} e^{-i\Omega t} + c.c\right)/2\right] \end{aligned} \tag{B.23}$$

$$\begin{aligned} N_{G,v}^{i,eq} &= \bar{N}_{G,v}^{i,eq} + \left(\widetilde{\Delta N_{G,v}^{i,eq}} e^{-i\Omega t} + c.c\right)/2 \\ &= \frac{\varepsilon_G}{V_0}\left[\bar{f}_{G,v}^{i,eq} + \left(\widetilde{\Delta f_{G,v}^{i,eq}} e^{-i\Omega t} + c.c\right)/2\right] \end{aligned} \tag{B.24}$$

We also assume the common valence band quasi-fermi level $E_{f,v}$ and quasi-equilibrium oscillate in the form:

$$E_{f,v} = \bar{E}_{f,v} + \left(\widetilde{\Delta E_{f,v}} e^{-i\Omega t} + c.c\right)/2 \tag{B.25}$$

where we can get the relation based on charge neutrality,

$$\widetilde{\Delta E_{f,v}} = \frac{\left(\left.\frac{\partial N_W}{\partial E_{f,c}}\right|_{\bar{E}_{f,c}} + \left.\frac{\partial N_B}{\partial E_{f,c}}\right|_{\bar{E}_{f,c}}\right)\widetilde{\Delta E_{f,c}} + \sum_i \xi^i \left(\frac{\varepsilon_E}{V_0}\widetilde{\Delta f_E^i} + \frac{\varepsilon_G}{V_0}\widetilde{\Delta f_G^i}\right)}{\left.\frac{\partial N_{W,v}}{\partial E_{f,v}}\right|_{\bar{E}_{f,v}} + \left.\frac{\partial N_{B,v}}{\partial E_{f,v}}\right|_{\bar{E}_{f,v}} + \sum_i \xi^i \left(\left.\frac{\partial N_{E,v}^{i,eq}}{\partial E_{f,v}}\right|_{\bar{E}_{f,v}} + \left.\frac{\partial N_{h,G}^{i,eq}}{\partial E_{f,v}}\right|_{\bar{E}_{f,v}}\right)}, \tag{B.26}$$

Notice that the relations between harmonic components depend heavily on the derivative values of carrier density or occupation factor with respect to the quasi-fermi levels determined by the CW solutions. The CW solutions can be numerically solved by setting all the time derivatives of the carrier densities to zero.

By collecting all the first order terms, the complex modulation amplitudes can be found by solving a set of coupled equations for modulation amplitude of QD occupation probabilities:

$$\begin{aligned} & i\Omega\widetilde{\Delta f_E^i} - \widetilde{\Delta f_E^i}\tau_{spon}^{-1} + \widetilde{\Delta f_w} R_{RE}^i - \widetilde{\Delta f_E^i} R_{ER}^i \\ & \quad - \widetilde{\Delta f_E^i} R_{EG}^i + \widetilde{\Delta f_G^i} R_{GE}^i \\ & \quad = \widehat{g_E^i}\left[\left(\widetilde{\Delta f_E^i} + \widetilde{\Delta f_{E,v}^i}\right)\bar{P}_p + \left(\bar{f}_E^i + \bar{f}_{E,v}^i - 1\right)\widetilde{\Delta P_p}\right], \end{aligned} \tag{B.27}$$

$$\begin{aligned} & i\Omega\widetilde{\Delta f_G^i} - \widetilde{\Delta f_G^i}\tau_{spon}^{-1} + \widetilde{\Delta f_w} R_{RG}^i - \widetilde{\Delta f_g^i} R_{GR}^i \\ & \quad + \frac{\varepsilon_E}{\varepsilon_G}\left(\widetilde{\Delta f_E^i} R_{EG}^i - \widetilde{\Delta f_G^i} R_{GE}^i\right) \\ & \quad = \widehat{g_G^i}\left[\left(\widetilde{\Delta f_G^i} + \widetilde{\Delta f_{G,v}^i}\right)\bar{P}_p + \left(\bar{f}_G^i + \bar{f}_{G,v}^i - 1\right)\widetilde{\Delta P_p}\right], \end{aligned} \tag{B.28}$$

$$
\begin{aligned}
& i\Omega\widetilde{\Delta f^i_{E,v}} - \widetilde{\Delta f^i_{E,v}}\tau^{-1}_{1,v} + \left.\frac{\partial f^{i,eq}_{E,v}}{\partial E_{fv}}\right|_{\bar{E}_{f,v}} \widetilde{\Delta E_{fv}}\tau^{-1}_{1v} \\
& \quad = \widehat{g^i_E}\left[\left(\widetilde{\Delta f^i_E} + \widetilde{\Delta f^i_{E,v}}\right)\bar{P}_p + \left(\bar{f}^i_E + \bar{f}^i_{E,v} - 1\right)\widetilde{\Delta P_p}\right],
\end{aligned} \tag{B.29}
$$

$$
\begin{aligned}
& i\Omega\widetilde{\Delta f^i_{G,v}} - \widetilde{\Delta f^i_{G,v}}\tau^{-1}_{1,v} + \left.\frac{\partial f^{i,eq}_{G,v}}{\partial E_{fv}}\right|_{\bar{E}_{f,v}} \widetilde{\Delta E_{fv}}\tau^{-1}_{1v} \\
& \quad = \widehat{g^i_G}\left[\left(\widetilde{\Delta f^i_G} + \widetilde{\Delta f^i_{G,v}}\right)\bar{P}_p + \left(\bar{f}^i_G + \bar{f}^i_{G,v} - 1\right)\widetilde{\Delta P_p}\right],
\end{aligned} \tag{B.30}
$$

where

$$
\widehat{g^i_x} = \frac{D_D\sigma_D}{D^i_D H_{mod} W} Q^{p,i}_x, \qquad (x = G, E) \tag{B.31}
$$

$$
\begin{cases}
R^i_{RE} = \tau^{-1}_{RE} - \bar{f}^i_E\left(\tau^{-1}_{RE} - {\tau^i_{ER}}^{-1}\right), \\
R^i_{ER} = \tau^{-1}_{ER} + \bar{f}_w\left(\tau^{-1}_{RE} - {\tau^i_{ER}}^{-1}\right), \\
R^i_{RG} = \tau^{-1}_{RG} - \bar{f}^i_G\left(\tau^{-1}_{RG} - {\tau^i_{GR}}^{-1}\right), \\
R^i_{GR} = \tau^{-1}_{GR} + \bar{f}_w\left(\tau^{-1}_{RG} - {\tau^i_{GR}}^{-1}\right), \\
R^i_{EG} = \tau^{-1}_{EG} - \bar{f}^i_G\left(\tau^{-1}_{EG} - {\tau^i_{GE}}^{-1}\right), \\
R^i_{GE} = \tau^{-1}_{GE} + \bar{f}^i_E\left(\tau^{-1}_{EG} - {\tau^i_{GE}}^{-1}\right),
\end{cases} \tag{B.32}
$$

The corresponding modulation amplitude of WL occupation probability $\widetilde{\Delta f_w}$ has the form as following;

$$
\widetilde{\Delta f_w} = \frac{\left(\sum \xi^i \frac{\varepsilon_E}{V_0}\widetilde{\Delta f^i_E}R^i_{ER} + \sum \xi^i \frac{\varepsilon_G}{V_0}\widetilde{\Delta f^i_G}R^i_{GR}\right)\left.\frac{\partial f_w}{\partial N_R}\right|_{\bar{E}_{f,c}}}{\tau_r^{-1} + \left(\sum \xi^i \frac{\varepsilon_E}{V_0}\widetilde{\Delta f^i_E}R^i_{RE} + \sum \xi^i \frac{\varepsilon_G}{V_0}\widetilde{\Delta f^i_G}R^i_{RG}\right)\left.\frac{\partial f_w}{\partial N_R}\right|_{\bar{E}_{f,c}} - i\Omega}, \tag{B.33}
$$

$$
\tau_r^{-1} = \frac{(A_B + 2B_BN_B + 3C_BN_B^2)\left.\frac{\partial N_B}{\partial E_{f,c}}\right|_{\bar{E}_{f,c}} + (A_W + 2B_WN_W + 3C_WN_W^2)\left.\frac{\partial N_W}{\partial E_{f,c}}\right|_{\bar{E}_{f,c}}}{\left.\frac{\partial N_R}{\partial E_{f,c}}\right|_{\bar{E}_{f,c}}}, \tag{B.34}
$$

Appendix C

Continuous Band Approximation for QD Electronic Structures

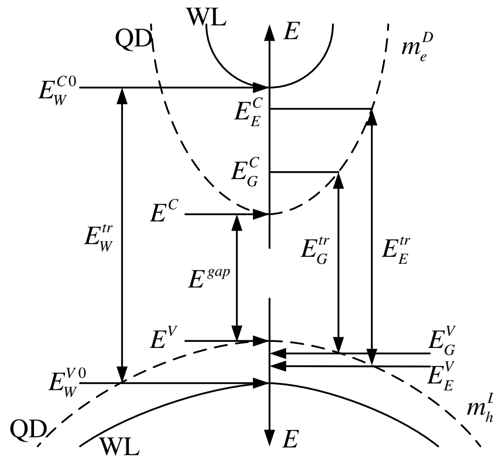

Figure C.1: Schematic band diagram based on continuous band approximation.

This appendix presents a continuous band approximation method [31] used to calculate QD electronic band structure. The advantages of this approach is that it requires only a little detailed knowledge of the exact electronic structure.

Hereby, a continuous bulk-like valence band is assumed and the hole effective mass is introduced to estimate the valence band energy and density of states. By assuming charge neutrality and quasi-equilibrium in the valence band, a common

Fermi energy in the QD valence band can be calculated to estimate the occupation probabilities in the valence band.

Thus the calculation of the QD hole occupation probabilities f_G^V and f_E^V for the QD gain terms, requires:

- a determination of the valence band energy;
- an estimation of the valence band DOS;
- a calculation of the Fermi energy of the total valence band;

As shown in Figure C.1, the conduction band energy E_G^C for the G state and E_E^C for the E state are fitted to a parabolic band (corresponding to a bulk DOS) with curvature determined by the effective electron mass of the QD material, m_e^D. By integrating over the bulk-like DOS from the effective conduction bandedge E^C to the bound energy of either the G or E state, multiplying by the effective volume of a single dot V_0 and equating it with either the number of states including degeneracy of the G state ε_G or that of combined G and E states $\varepsilon_E + \varepsilon_G$, two equations are formed:

$$\varepsilon_G = \frac{V_0}{2\pi^2}\left[\frac{2m_e^D}{\hbar^2}\left(E_G^C - E^C\right)\right]^{3/2} \tag{C.1}$$

$$\varepsilon_E + \varepsilon_G = \frac{V_0}{2\pi^2}\left[\frac{2m_e^D}{\hbar^2}\left(E_E^C - E^C\right)\right]^{3/2} \tag{C.2}$$

By solving these two equations, the effective conduction bandedge E^C and the effective volume of a single dot V_0 can be found:

$$E^C = \frac{E_G^C\left(1+\frac{\varepsilon_E}{\varepsilon_G}\right)^{2/3} - E_E^C}{\left(1+\frac{\varepsilon_E}{\varepsilon_G}\right)^{2/3} - 1} \tag{C.3}$$

and

$$V_0 = 3\pi^2\varepsilon_G\hbar^3\left(2m_e^D\left[E_E^C - E_G^C\right)\right]^{-3/2} \tag{C.4}$$

By using the effective parabolic band approximation and 'k-conservation' assumption in the transition, the relations between energies follows:

$$E_G^C = E^C + \frac{m_h^D}{m_e^D + m_h^D}\left(E_G^{tr} - E^{gap}\right) \tag{C.5}$$

$$E_E^C = E^C + \frac{m_h^D}{m_e^D + m_h^D}\left(E_E^{tr} - E^{gap}\right) \tag{C.6}$$

where m_h^D is the effective hole mass of the QD material. E_G^{tr} and E_E^{tr} is the transition energy of the G state and ES. E^{gap} is the energy gap between the conduction bandedge E^C and valence bandedge E^V. Substitute E_E^C and E_G^V into Eq. (C.3), we have:

$$E^C = \frac{\left[E^C + \frac{m_h^D}{m_e^D+m_h^D}\left(E_G^{tr} - E^{gap}\right)\right]\left(1+\frac{\varepsilon_E}{\varepsilon_G}\right)^{2/3} - \left[E^C + \frac{m_h^D}{m_e^D+m_h^D}\left(E_E^{tr} - E^{gap}\right)\right]}{\left(1+\frac{\varepsilon_E}{\varepsilon_G}\right)^{2/3} - 1}$$

$$= E^C + \frac{\frac{m_h^D}{m_e^D+m_h^D}\left(E_G^{tr} - E^{gap}\right)\left(1+\frac{\varepsilon_E}{\varepsilon_G}\right)^{2/3} - \frac{m_h^D}{m_e^D+m_h^D}\left(E_E^{tr} - E^{gap}\right)}{\left(1+\frac{\varepsilon_E}{\varepsilon_G}\right)^{2/3} - 1} \tag{C.7}$$

thus the energy gap E^{gap} can be derived from Eq. (C.7):

$$E^{gap} = \frac{E_G^{tr}\left(1+\frac{\varepsilon_E}{\varepsilon_G}\right)^{2/3} - E_E^{tr}}{\left(1+\frac{\varepsilon_E}{\varepsilon_G}\right)^{2/3} - 1} \tag{C.8}$$

In order to calculated the E^C level, we introduce relation:

$$\frac{E_W^{C0} - E^C}{E_W^{V0} - E^V} = \frac{\Delta^C}{1-\Delta^C} \tag{C.9}$$

where the conduction and valence bandedge of WL E_W^{C0},E_W^{V0} are set as reference zero level, Δ^C is the relative band offset between the QD and QW materials. Due to the fact of large variety of dot sizes and strains, Δ^C is expected to be different [160]. In this thesis, $\Delta^C = \frac{m_h^D}{m_h^D+m_e^D}$ is used.

The DOS of the QD valence band for a single QD, $\rho^{V,D}(E)$, is now given as:

$$\rho^{V,D}(E) = \begin{cases} \frac{1}{2\pi^2}\left(\frac{2m_e^D}{\hbar^2}\right)^{3/2}\sqrt{E-E^V} & ,E > E^V \\ 0 & ,E < E^V \end{cases} \tag{C.10}$$

With the knowledge of DOS, a common Fermi energy E_F^D in the valence band can be calculated through an integral equation:

$$N^V = \int_{-\infty}^{\infty} \rho^V(E)\left[1+\exp\left(\frac{E-E_F^D}{k_BT}\right)\right]^{-1} dE \tag{C.11}$$

where ρ^V is density of states of the total valence band, which includes the contribution from the QD as well as the WL and barrier. N^V is the hole density, which is correlated with the electron density according to the charge neutrality relation. Thus the hole occupation probability calculated reflects the characteristics of the bulk-like semiconductor material.

Appendix D

Analytical Derivation of Three Wave Mixing in SOA

This appendix includes the derivations of a semi-analytical solution of the three wave mixing in SOA.

Based on Eq. 6.2, the propagation equation for optical intensity S is

$$\frac{dS}{dz} = \left(\gamma_0 + \gamma_0^*\right) S \tag{D.1}$$

The propagation equation ofE_0 can be transformed by substituting variable z with normalized optical intensity S:

$$\frac{dE_0}{dS} - \frac{\gamma_0}{\left(\gamma_0 + \gamma_0^*\right) S} E_0 = 0 \tag{D.2}$$

Which can be solved for E_0 to obtain:

$$\begin{aligned} &E_0\left(z\right) = E_0\left(0\right) e^{F(z)}; \\ &F\left(z\right) = \int\limits_{S(0)}^{S(z)} \frac{\gamma_0}{\left(\gamma_0+\gamma_0^*\right) S'} dS' \\ &= \frac{1}{2} \frac{a_{\text{int}}-\Gamma g_0+i\Gamma g_0 \alpha}{a_{\text{int}}-\Gamma g_0} \ln\left(\frac{S(z)}{S(0)}\right) - \frac{1}{2} \frac{i\Gamma g_0 \alpha}{a_{\text{int}}-\Gamma g_0} \ln\left(\frac{a_{\text{int}}-\Gamma g_0+a_{\text{int}} S(z)}{a_{\text{int}}-\Gamma g_0+a_{\text{int}} S(0)}\right) \end{aligned} \tag{D.3}$$

Here, $S(z)$ and $S(0)$ are the output and input power of S, which can easily be related numerically by Eq. (D.1). We can also keep the function $F(z)$ in the form of an integral over the propagation length z in SOA with implicit relation between power S and propagation length z as:

$$F\left(z\right) = \int\limits_0^z \gamma_0 dz' \tag{D.4}$$

Here we introduce the new normalized complex amplitude $\tilde{E}_{\pm 1}$:

$$E_{\pm 1} = \tilde{E}_{\pm 1} e^{F(z)} \tag{D.5}$$

Inserting $\tilde{E}_{\pm 1}$ into the propagation equations of $E_{\pm 1}$, When $|e^{F(z)}| \neq 0$ and $|E_0(0)| = E_0(0)$, we have a new set of propagation equations of $\tilde{E}_{\pm 1}$:

$$\begin{cases} \frac{d\tilde{E}_{-1}}{dz} = \xi_{-1}\left(\tilde{E}_{-1} + \tilde{E}^*_{+1}\right)|E_0(z)|^2 \\ \frac{d\tilde{E}_{+1}}{dz} = \xi_{+1}\left(\tilde{E}_{+1} + \tilde{E}^*_{-1}\right)|E_0(z)|^2 \end{cases} \tag{D.6}$$

By defining an extra pair of variables

$$\begin{cases} u = \tilde{E}_{+1} + \tilde{E}^*_{-1} \\ v = \tilde{E}_{+1} - \tilde{E}^*_{-1} \end{cases} \tag{D.7}$$

We have

$$\begin{cases} \frac{du}{dz} = \left(\xi_{+1} + \xi^*_{-1}\right)|E_0\left(z\right)|^2 u \\ \frac{dv}{dz} = -i\alpha\left(\xi_{+1} + \xi^*_{-1}\right)|E_0\left(z\right)|^2 u \end{cases} \tag{D.8}$$

A propagation equation of the form:

$$\frac{du}{dS} - P_{sat}\frac{\left(\xi_{+1} + \xi^*_{-1}\right)S}{\left(\gamma_0 + \gamma^*_0\right)S}u = 0 \tag{D.9}$$

can be solved for u, v to obtain:

$$\begin{cases} u\left(z\right) = u\left(0\right)e^{H(z)} \\ v\left(z\right) = v\left(0\right) + i\alpha u\left(0\right)\left(1 - e^{H(z)}\right) \end{cases} \tag{D.10}$$

Where

$$H\left(z\right) \equiv \gamma_1 + i\beta_1 = P_{sat}\int_{S(0)}^{S(z)}\frac{\left(\xi_{+1} + \xi^*_{-1}\right)S'}{\left(\gamma_0 + \gamma^*_0\right)S'}dS' \tag{D.11}$$

$$\begin{aligned} \gamma_1 = \Gamma g_0 \Bigg[& \frac{a_{\text{int}}{\tau_s}^2\Omega^2}{\tau_s\Omega\left((\Gamma g_0)^2 + {a_{\text{int}}}^2{\tau_s}^2\Omega^2\right)}\text{Arctan}\left(\frac{\Omega\tau_s(S(z)-S(0))}{(\Omega\tau_s)^2 + (1+S(z))(1+S(0))}\right) \\ & + \frac{\Gamma g_0}{(\Gamma g_0)^2 + {a_{\text{int}}}^2{\tau_s}^2\Omega^2}\ln\left(\frac{a_{\text{int}} - \Gamma g_0 + a_{\text{int}}S(z)}{a_{\text{int}} - \Gamma g_0 + a_{\text{int}}S(0)}\right) \\ & - \frac{1}{2}\frac{\Gamma g_0}{(\Gamma g_0)^2 + {a_{\text{int}}}^2{\tau_s}^2\Omega^2}\ln\left(\frac{1+2S(z)+S(z)^2+{\tau_s}^2\Omega^2}{1+2S(0)+S(0)^2+{\tau_s}^2\Omega^2}\right)\Bigg] \end{aligned} \tag{D.12}$$

$$\beta_1 = \Gamma g_0 \Omega \tau_s \left[-\frac{\Gamma g_0}{\tau_s \Omega \left((\Gamma g_0)^2 + {a_{\mathrm{int}}}^2 {\tau_s}^2 \Omega^2 \right)} \mathrm{Arctan} \left(\frac{\Omega \tau_s (S(z) - S(0))}{(\Omega \tau_s)^2 + (1+S(z))(1+S(0))} \right) \right.$$
$$+ \frac{a_{\mathrm{int}}}{(\Gamma g_0)^2 + {a_{\mathrm{int}}}^2 {\tau_s}^2 \Omega^2} \ln \left(\frac{a_{\mathrm{int}} - \Gamma g_0 + a_{\mathrm{int}} S(z)}{a_{\mathrm{int}} - \Gamma g_0 + a_{\mathrm{int}} S(0)} \right) \tag{D.13}$$
$$\left. - \frac{1}{2} \frac{a_{\mathrm{int}}}{(\Gamma g_0)^2 + {a_{\mathrm{int}}}^2 {\tau_s}^2 \Omega^2} \ln \left(\frac{1 + 2S(z) + S(z)^2 + {\tau_s}^2 \Omega^2}{1 + 2S(0) + S(0)^2 + {\tau_s}^2 \Omega^2} \right) \right]$$

This result is equivalent to the semi-analytical solution for the time delay given in [66]. When the internal loss a_{int} is neglected, Eq. (D.13) is equivalent to the semi-analytical solution for the time delay given in [52]. The function H(z) can be kept in the form of an integral over the propagation length z with implicit relations between power S and propagation length z.

$$H(z) = \int_0^z \xi_u |E_0(z')|^2 dz' = P_{sat} \int_0^z \xi_u S dz' \tag{D.14}$$

Thus a general solution to the evolution of electric fields in SOA is:

$$\begin{cases} E_0(z) = E_0(0) e^{F(z)} \\ E_{+1}(z) = \tilde{E}_{+1}(z) e^{F(z)} = e^{F(z)} \left\{ \frac{1}{2} v(0) + \frac{1}{2} u(0) \left[e^{H(z)} + i\alpha \left(1 - e^{H(z)} \right) \right] \right\} \\ E_{-1}^*(z) = \tilde{E}_{-1}^*(z) e^{F(z)^*} = e^{F(z)^*} \left\{ -\frac{1}{2} v(0) + \frac{1}{2} u(0) \left[e^{H(z)} - i\alpha \left(1 - e^{H(z)} \right) \right] \right\} \end{cases} \tag{D.15}$$

Appendix E

Simulation Parameters

Table E.1: Typical Parameter Values for MPREM model

W	2μm	$m_e^D = m_e^W$	$0.026m_0$
H	250nm	$m_h^D = m_h^W$	$0.0742m_0$
L	2mm	m_e^B	$0.062m_0$
D_D	4×10^{10}cm^{-2}	m_h^B	$0.1628m_0$
H_W	1nm	$\bar{V}_0$	4.509×10^{-24}m^3
H_{mod}	400nm	Z_{RG}^P	1.6×10^{11}s^{-1}
Γ_a	0.3	Z_{RG}^A	1×10^{11}s^{-1}
Γ_{W0}	0.0012	Z_{RE}^P	2.5×10^{11}s^{-1}
Γ_W	0.006	Z_{RE}^A	1.5×10^{11}s^{-1}
T	300K	Z_{EG}^P	5×10^{11}s^{-1}
Δ^C	0.742	Z_{EG}^A	4.5×10^{12}s^{-1}
E_W^{tr}	1.3eV	A_W	2×10^8s^{-1}
$\hbar\omega_E = E_E^{tr0}$	1.21eV	B_W	1.2×10^{-16}m^{3}s^{-1}
$\hbar\omega_G = E_G^{tr0}$	1.1eV	C_W	5×10^{-42}m^{6}s^{-1}
E_B^{gap}	1.42eV	A_B	4.7×10^8s^{-1}
ε_G	2	B_B	5×10^{-17}m^{3}s^{-1}
ε_E	4	C_B	5.24×10^{-41}m^{6}s^{-1}
γ_H	3.3meV	δ_X	γ_H or smaller
γ_G	67meV	γ_E	80meV
α_{int}	2cm^{-1}	σ_D	1×10^{-20}m^{2}eV
n_l	5		

Appendix F

List of PhD Publications

Journal Contributions:

1. Jerper Mørk, Per Lunnemann Hansen, Weiqi Xue, **Yaohui Chen**, Per Kaer Nielsen and Torben Roland Nielsen, Slow and fast light in semiconductor waveguides, Semicond. Sci. Technol. 25, 083002, 2010

2. **Yaohui Chen**, Jesper Mørk, Ultrahigh-Frequency Microwave Phase Shifts Mediated by Ultrafast Dynamics in Quantum Dot Semiconductor Optical Amplifiers, IEEE Photonic. Technol. Lett., 22, 935-937, 2010

3. **Yaohui Chen**, Jesper Mørk, Enhancing Slow and Fast Light Effects in Quantum Dot Semiconductor Waveguides through Ultrafast Dynamics, Opt. Lett., 35, 697-699, 2010

4. Lei Wei, Weiqi Xue, **Yaohui Chen**, Thomas Tanggaard Alkeskjold, Anders Overgaard Bjarklev, Optically fed microwave true-time delay based on a compact liquid-crystal hotonic-bandgap-fiber device, Opt. Lett., 34, 2757-2759, 2009

5. Weiqi Xue, **Yaohui Chen**, Filip Öhman, Jesper Mørk, The role of input chirp on phase shifters based on slow and fast light effects in semiconductor optical amplifiers, Opt. Express, 17, 1404-1413, 2009

6. Weiqi Xue, **Yaohui Chen**, Filip Öhman, Salvador Sales, Jesper Mørk, Enhancing light slow-down in semiconductor optical amplifiers by optical filtering, Opt. Lett., 33, 1084-1086, 2008

7. Jesper Mørk, Filip Öhman, Mike van der Poel, **Yaohui Chen**, Per Lunnemann Hansen, Kresten Yvind, Slow and fast light: Controlling the speed of light using semiconductor waveguides, Laser Photonics Rev.,3, 30, 2009

8. **Yaohui Chen**, Weiqi Xue, Filip Öhman, Jesper Mørk, Theory of Optical-Filtering Enhanced Slow and Fast Light Effects in Semiconductor Optical Waveguides, J. Lightwave Technol., 26, 3734, 2008

9. Weiqi Xue, Filip Öhman, Søren Blaaberg, **Yaohui Chen**, Salvador Sales, Jesper Mørk, Broadband microwave photonic phase shifter based on polarisation rotation, Electron. Lett., 44, 684-685, 2008

Conference Contributions:

1. **Yaohui Chen**, Jesper Mørk, Microwave Signal Processing based on Ultrafast Dynamics in Quantum Dot Waveguides, We.B3.3, ICTON 2010, Munich. (invited)

2. Jesper Mørk, Weiqi Xue, **Yaohui Chen**, Søren Blaaberg, Salvador Sales, and Jose Capmany, Recent advances in slow and fast light for applications in microwave photonics, SPIE Photonics West, paper 7612-33, San Francisco, Jan. 2010 (Invited Paper).

3. **Yaohui Chen**, Jesper Mørk, Enhancing slow and fast light effects in quantum dot optical amplifiers through ultrafast dynamics, LEOS 2009, ThG 5, Belek-Antalya, Turkey, 2009

4. **Yaohui Chen**, Jesper Mørk, Broadband microwave shifter based on high speed cross gain modulation in quantum dot semiconductor optical amplifiers, Slow and fast light (SL) 2009, STuB5, Honolulu, Hawaii, USA, 2009

5. **Yaohui Chen**, Jesper Mørk, Quantum dot waveguides: ultrafast dynamics and applications, ICTON 2009, Mo.C.1.1, Azores, Portugal, 2009 (invited)

6. Lei Wei, Weiqi Xue, **Yaohui Chen**, Thomas Tanggaard Alkeskjold, Anders Overgaard Bjarklev, Compact optically-fed microwave true-time delay using liquid crystal photonic bandgap fiber device, Slow and Fast Light, (SL2009), JTuB27, 2009

7. Weiqi Xue, **Yaohui Chen**, Salvador Sales, Søren Blaaberg, Jesper Mørk, Jose Capmany, Microwave photonics processing controlling the speed of light in semiconductor waveguides, ICTON 2009, Mo.D5.3, Azores, Portugal, 2009 (invited)

8. Jose Capmany, Salvador Sales, Weiqi Xue, **Yaohui Chen**, Søren Blaaberg, Jesper Mørk, Optical signal processing using slow and fast light technologies, 14th European conference on networks and optical communications, 351-359, 2009, Valladolid, Spain

9. Jesper Mørk, Weiqi Xue, **Yaohui Chen**, Søren Blaaberg, Controlling the speed of light in semiconductor waveguides: Physics and applications, CLEO / Europe EQEC 2009, JTuF4, 2009

10. Weiqi Xue, **Yaohui Chen**, Filip Öhman, Salvador Sales, Kresten Yvind, Jesper Mørk , Slow and fast light effects in semiconductor waveguides for applications in microwave photonics, SPIE Photonics West, 7226-32, 2009, San Jose, CA, USA

11. Jesper Mørk, Weiqi Xue, **Yaohui Chen**, Filip Öhman, Per Kær Nielsen, Henri Thyrrestrup Nielsen, Torben Roland Nielsen, Exploring carrier dynamics in semiconductors for slow light, 2009 IEEE/LEOS Winter Topicals Meeting Series, TuB4.2, pages: 150-151, 2009, Innsbruck, Austria

12. Mørk, Jesper ; Nielsen, Torben Roland ; Xue, Weiqi ; **Chen, Yaohui** ; Hansen, Per Lunnemann, Slow and fast light in semiconductor structures: physics and applications [invited] International Nano-Optoelectronics Workshop (iNOW), 2009, Berlin, Germany

13. Jesper Mørk, Filip Öhman, Weiqi Xue, **Yaohui Chen**, Søren Blaaberg, Salvador Sales, Slow and fast light effects in semiconductor waveguides for applications in microwave photonics, International Topical Meeting on Microwave Photonics (MWP 2008), 210-213, 2008, Gold Coast, Brisbane, Australia

14. **Yaohui Chen**, Filip Öhman, Jesper Mørk, Pulse train amplification and regeneration based on semiconductor quantum dots waveguide, Semiconductor quantum dot devices and applications workshop, 2008, Rennes, France

15. **Yaohui Chen**, Weiqi Xue, Filip Öhman, Jesper Mørk, Semi-analytical model of filtering effects in microwave phase shifters based on semiconductor optical amplifiers, Slow and Fast Light (SL) 2008, JMB14, 2008, Boston, Massachusetts, USA

16. Weiqi Xue, **Yaohui Chen**, Filip Öhman, Salvador Sales, Jesper Mørk, Chirp Dependence of Filter Assisted Slow and Fast Light Effects in Semiconductor Optical Amplifiers, Slow and Fast Light (SL) 2008, JMB12, 2008, Boston, Massachusetts, USA

17. Weiqi Xue, Filip Öhman, **Yaohui Chen**, Salvador Sales, Jesper Mørk, Experimental demonstration of strongly enhanced light slow-down in semiconductor optical amplifiers by optical filtering, Slow and Fast Light (SL) 2008, STuA5, 2008, Boston, Massachusetts, USA

18. **Yaohui Chen**, Filip Öhman, Weiqi Xue, Jesper Mørk, Analysis of an effective optical filtering technique to enhance microwave phase shifts based on slow and fast light effects, CLEO/QELS 2008, CME4, San Jose, CA, 2008

19. Weiqi Xue, Filip Öhman, Søren Blaaberg, **Yaohui Chen**, Salvador Sales, Jesper Mørk, Microwave phase shifter based on mach-zehnder intensity modulator and polarization rotation in an SOA, CLEO/QELS 2008, CMP2, San Jose, CA, 2008

20. Jesper Mørk , Filip Öhman, Mike van der Poel, **Yaohui Chen**, Weiqi Xue, Per L. Hansen, Kresten Yvind, Carrier dynamics and slow light in semiconductor nanostructure, CLEO/QELS 2008, CTuJ1, San Jose, CA, 2008 (invited)

21. Jesper Mørk, Filip Öhman, **Yaohui Chen**, Mike van der Poel, Kresten Yvind, Slow and fast light in semiconductor waveguides for applications in microwave photonics Photonics West, 2008, San Jose, USA

22. Filip Öhman, Salvador Sales; **Yaohui Chen**; E. Granell; Jesper Mørk, Large microwave phase shift and small distortion in an integrated waveguide device, OSA Topical meeting Slow and fast light, 2007

Bibliography

[1] S. Prasad, H. Schumacher, and A. Gopinath. *High-speed electronics and optoelectronics: devices and circuits.* Cambridge University Press, 2009.

[2] H.J.S. Dorren, M.T. Hill, Y. Liu, E. Tangdiongga, M.K. Smit, and G.D. Khoe. Digital optical signal processing for telecomminication applications. In *Proceedings of 2005 7th International conference on Transparent Optical Network, ICTON 2005*, pages 25–28, 2005.

[3] D. Cotter, R. J. Manning, K.J. Blow, D. Ellis, A. E. Kelly, D. Nesset, I.D. Phillips, A. J. Poustie, and D. C. Rogers. Nonlinear optics for high-speed digital information processing. *Science*, 286:1523–1528, November 1999.

[4] A. J. Seeds and K. J. Williams. Microwave photonics. *J. of Lightwave Technol.*, 24:4628, 2006.

[5] J. Yao. Microwave photonics. *J. of Lightwave Technol.*, 27:314–335, 2009.

[6] Y. Arakawa and H. Sakaki. Multidimensional quantum well laser and temperature dependence of its threshold current. *Appl. Phys. Lett.*, 40:939, 1982.

[7] Al. L. Efros and A.L. Efros. Pioneering effort i. *Sov. Phys. Semicond.*, 16:772, 1982.

[8] D.Bimberg, M. Grundmann, and N.N. Ledentsov. *Quantum Dot Heterostructures.* John Wiley and Sons Ltd., 1999.

[9] Y. Masumoto. *Semiconductor Quantum Dots, Physics, Spectroscopy and Applications.* Springer-Verlag, 2002.

[10] M. Sugawara, N. Hatori, M. Ishida, H. Ebe, Y. Arakawa, K. Otsubo, T. Yamamoto, and Y. Nakata. Recent progress in self-asembled quantum-dot optical devices for optical telecommunication: temparature-insensitive 10gb s^{-1} directly modulated lasers and 40 gb s^{-1} signal-regenerative amplifiers. *J. Phys. D: Appl. Phys.*, 38:2126–2134, 2005.

[11] C. Meuer, H. Schmeckebier, G. Fiol, D. Arsenijevic, J. Kim, G. Eisenstein, and D. Bimberg. Cross-gain modulation and four-wave mixing for wavelength conversion in undoped and p-doped 1.3- quantum dot semiconductor optical amplifiers. *Photonics Journal, IEEE*, 2:141 –151, april 2010.

[12] C. Liu, Z. Dutton, C. H. Behroozi, , and L. V. Hau. Observation of coherent optical information storage in an atomic medium using halted light pulses. *Nature*, 409:490–493, 2001.

[13] M. S. Bigelow, N. N. Lepeshkin, and R. W. Boyd. Observation of ultra-slow light propagation in a ruby crystal at room temperature. *Phys. Rev. Lett.*, 90(11):113903, 2003.

[14] R. Nötzel. Self-organized growth of quantum-dot structures. *Semiconductor Science and Technology*, 11:1365–1379, 1996.

[15] Ivan V. Markov. *Crystal Growth for Beginners: Fundamentals of Nucleation, Crystal Growth, and Epitaxy.* Singapore: World Scientific, 1995.

[16] K. Jacobi. Atomic structure of inas quantum dots on gaas. *Progress in Surface Science*, 71:185–215, 2003.

[17] L.E. Vorobjev, N.K. Fedosov, V. Yu Panevin, D.A. Firsov, V.A. Shalygin, M.I. Grozina, A. Andreev, V.M. Ustinov, I.S. Tarasov, N.A. Pikhtin, Yu B Samsonenko, A.A. Tonkikh, G.E. Cirlin, V. A. Egorov, F.H. Julien, F.Fossard, A. Helman, and Hh Moumanis. Interband light absorption and pauli blocking in inas/gaas quantum dots covered by ingaas quantum wells. *Semicond. Sci. Technol.*, 22:814–818, 2007.

[18] O. Stier, M. Grundmann, and D. Bimberg. Electronic optical properties of strained quantum dots modeled by 8-band $k \cdot p$ theory. *Phys. Rev. B*, 59:5688–5701, 1999.

[19] C. Lok, L. Yan Voon, and M. Willatzen. *The* $\boldsymbol{k}\cdot\boldsymbol{p}$ *Method: Electronic Properties of Semiconductors.* Springer-Verlag Berlin Heidelberg, 2009.

[20] J. M. Luttinger and W. Kohn. Motion of electrons and holes in perturbed periodic fields. *Phys. Rev.*, 97:869, 1955.

[21] E. O. Kane. Band structure of indium antimonide. *J. Phys. Chem. Solids*, 1:249, 1957.

[22] A.J. Williamson, L. W. Wang, and A. Zunger. Theoretical interpretation of the experimental electronic structure of lens-shaped self-assembled inas/gaas quantum dots. *Phys. Rev. B*, 62, 2000.

[23] A.V. Uskov, J. Mcinerney, F. Adler, H. Schweizer, and M.H. Pilkuhn. Auger carrier capture in self-assembled quantum dot structures. *Appl. Phys. Lett.*, 72:58–60, 1998.

[24] B. Ohnesorge, M. Albrecht, J. Oshinowo, and A. Forchel. Rapid carrier relaxation in self-assembled $\mathrm{in}_x\mathrm{ga}_{1-x}\mathrm{as}$/gaas quantum dots. *Phys. Rev. B*, 54:11532–11538, 1996.

[25] S. Raymand, K. Hinter, S. Fafard, and J.L. Merz. Experimental determination of auger capture coefficients in self-assembled quantum dots. *Phys. Rev. B*, 61:16331–4, 2000.

[26] R. Heitz, H. Born, F. Guffarth, O. Stier, A. Schliwa, A. Hoffmann, and D. Bimberg. Existence of a phonon bottleneck for excitons in quantum dots. *Phys. Rev. B*, 64:241305, 2001.

[27] I. Magnusdottir, A. V. Uskov, S. Bischoff, B. Tromborg, and J. Mørk. One- and two-phonon capture processes in quantum dots. *J. Appl. Phys.*, 92:5982–5990, 2002.

[28] T.R.Nilsen, P. Gartner, F. Jahnke, and A.A. Sawchuk. Many-body theory of carrier capture and relaxation in semiconductor quantum-dot lasers. *Phys. Rev. B*, 69:235314, 2004.

[29] T. Markussen, P. Kristensen, B. Tromborg, T. W. Berg, and J. Mørk. Influence of wetting layer wave functions on phonon-mediated carrier capture into self-assembled quantum dots. *Phys. Rev. B*, 74:195342–1–6, 2006.

[30] M. Sugawara, H. Ebe, N. Hatori, and M. Ishida. Theory of optical signal amplification and processing by quantum-dot semicondcutor optical amplifiers. *Phy. Rev. B*, 69:235332, 2004.

[31] T.W. Berg and J. Mørk. Saturation and noise properties of quantum-dot optical amplifiers. *IEEE J. Quantum Elect.*, 40:1527–1539, 2004.

[32] P. Borri, W. Langbein, J.M. Hvam, F. Heinrichsdorff, M.-H. Mao, and D. Bimberg. Spectral hole-burning and carrier heating dynamics in ingaas quantum dot amplifiers. *J. Sel. Topics. Q. El.*, 6:544, 2000.

[33] I.O'Driscoll, T. Piwonski, C.F. Schleussner, J. Houlihan, G. Huyet, and R.J. Manning. Electron and hole dynamics of inas/gaas quantum dot semiconductor optical amplifier. *Appl. Phys. Lett.*, 91:071111, 2007.

[34] S. Dommers, V. V. Temnov, U. Woggon, J. Gomis, J. Martinez-Pastor, M. Laemmlin, and D. Bimberg. Complete ground state gain recovery after ultrashort double pulses in quantum dot based semiconductor optical amplifer. *Appl. Phys. lett.*, 90:033508, 2007.

[35] V. Cesari, W. Langbein, P. Borri, M. Rossetti, A. Fiore, S. Mikhrin, I. Krestnikov, and A. Kovsh. Ultrafast gain dynamics in 1.3 micron inas/gaas quantum-dot optical amplifiers: The effect of p doping. *Appl. Phys. Lett.*, 90:201103, 2007.

[36] A. J. Zilkie, J. Meier, M. Mojahedi, P. J. Poole, P. Barrios, D. Poitras, T. J. Rotter, C. Yang, A. Stintz, K. J. Malloy, P. W.E. Smith, and J.S. Aitchison. Carrier dyanamics of quantum-dot, quantum-dash, and quantum-well semiconductor optical amplifiers operating at 1.55μm. *IEEE J. Quantum Elect.*, 43:982, 2007.

[37] T. Vallaitis, C. Koos, R. Bonk, W. Freude, M. Laemmlin, C. Meuer, D. Bimberg, and J. Leuthold. Slow and fast dynamics of gain and phase in a quantum dot semiconductor optical amplifier. *Opt. Expr.*, 16:170–178, 2008.

[38] T. Akiyama, H. Kuwatsuka, T. Simoyama, Y. Nakata, K. Mukai, M. Sugawara, O. Wada, and H. Ishikawa. Application of spectral-hole burning in the inhomogeneously broadened gain of self-assembled quantum dots to a

multiwavelength-channel nonlinear optical device. *IEEE Photonic. Technol. Lett.*, 12:1301–1303, 2000.

[39] C. Meuer, H. Schmeckebier, G. Fiol, D. Arsenijevic, J. Kim, G. Eisenstein, and D. Bimberg. Cross-gain modulation and four-wave mixing for wavelength conversion in undoped and p-doped 1.3μm quantum dot semiconductor optical amplifiers. *IEEE Photonics Journal*, 1:141–151, 2010.

[40] C. Meuer, J. Kim, M. Laemmlin, S. Liebich, D. Bimberg, A. Capua, G. Eisenstein, R. Bonk, T. Vallaitis, J. Leuthold, A.R. Kovsh, and I.L. Krestnikov. 40 ghz small-signal cross-gain modulation in 1.3 μm quantum dot semiconductor optical amplifiers. *Appl. Phys. Letts.*, 93:051110, 2008.

[41] T. Akiyama, M. Ekawa, M. Sugawara, K. Kawaguchi, H. Sudo, A. Kuramata, H. Ebe, and Y. Arakawa. An ultrawide-band semiconductor optical amplifier having an extremely high penalty-free output power of 23dbm achieved with quantum dots. *IEEE Photonic. Tech. Lett.*, 8, 2005.

[42] A. Bilenca and G. Eisenstein. On the noise properties of linear and nonlinear quantum-dot semiconductor optical amplifiers: The impact of inhomogeneously broadened gain and fast carrier dynamics. *IEEE J. Quantum Elect.*, 40:690–702, 2004.

[43] A. Markus, M. Rossetti, V. Calligari, J.X. Chen, and A. Fiore. Role of thermal hopping and homogeneous broadening on the spectral characteristics of quantum dot laers. *J. Appl. Phys.*, 98:1–8, 2005.

[44] J. Kim, M. Laemmlin, C. Meuer, D. Bimberg, and G. Eisenstein. Theoretical and experimental study of high-speed small-signal cross gain modulation of quantum-dot semiconductor optical amplifiers. *IEEE J. Quantum Elect.*, 45:240–248, 2009.

[45] E. Gehrig and O. Hess. Mesoscopic spatiotemporal theory for quantum dot laser dynamics. *Phys. Rev. A*, 65:033804, 2002.

[46] W.W. Chow and S.W. Koch. Theory of semiconductor quantum-dot laser dynamics. *IEEE J. Quantum Elect.*, 41:495–505, 2005.

[47] M. van der Poel, E. Gehrig, O. Hess, D. Birkedal, and J.M. Hvam. Ultrafast gain dynamics in quantum-dot amplifiers: Theoretical analysis and experimental investigations. *IEEE J. Quantum Elect.*, 41:1115–1123, 2005.

[48] D.W. Reschner, E. Gehrig, and O. Hess. Pulse amplification and spatio-spectral hole-burning in inhomogeneously broadened quantum-dot semiconductor optical amplifiers. *IEEE J. Quantum Elect.*, 45:21–33, 2009.

[49] J. Mørk, F. Öhman, M. van der Poel, Y. Chen, and K. Yvind P. L. Hansen. Slow and fast light: Controlling the speed of light using semiconductor waveguides. *Laser Photonics Rev.*, 3:30, 2009.

[50] P. Ku, F. Sedgwick, C.J. Chang-Hasnain, P. Palinginis, T. Li, H. Wang, S. Chang, and S. Chuang. slow light in semiconductor quantum wells. *Opt. Lett.*, 29:2291, 2004.

[51] P. Palinginis, S. Crankshaw, F. Sedgwick, E.-T. Kim, M. Moewe, and C. J. Chang-Hasnain. Ultra-slow light (<200 m/s) propagation in a semiconductor nanostructure. *Appl. Phys. Lett.*, 87(17):171102, 2005.

[52] J. Mørk, R. Kjær, M. van der Poel, and K. Yvind. Slow light in a semiconductor waveguide at gigahertz frequencies. *Opt. Express*, 13:8136–8145, 2005.

[53] Y. Okawachi, M.S. Bigelow, J.E. Sharping, Z.Zhu, A. Schweinsberg, D.J. Gauthier, R.W. Boyd, and A.L. Gaeta. Tunable all-optical delay via brillouin slow light in an optical fiber. *Phys. Rev. Lett.*, 94:153902, 2005.

[54] K.Y. Song, M.G. Hrráez, and L. Thévenaz. Observation of pulse delaying and advancement in optical fibers using stimulated brillouin scattering. *Opt. Express*, 13:82–88, 2005.

[55] D. Dahan and G. Eisenstein. Tunable all optical delay via slow and fast light propagation in a raman assisted fiber optical parametric amplifier: a route to all optical buffering. *Opt. Express*, 13:6234, 2005.

[56] Y.A. Vlasov, M. O'Boyle, H.F. Hamann, and S.J. McNab. Active control of slow light on a chip with photonic crystal waveguide. *Nature*, 438:65, 2005.

[57] L.H. Frandsen, A. Lavrinenko, J. Fage-Pedersen, and P. I. Borel. Photonic crystal waveguides with semi-slow light and tailored dispersion properties. *Opt. Express*, 14:9444–9450, 2006.

[58] M. Fleischhauer, A. Imamoglu, and J. P. Marangos. Electromagnetically induced transparency: Optics in coherent media. *Rev. Mod. Phys.*, 77:633, 2005.

[59] R. S. Tucker, P.-C. Ku, and C. J. Chang-Hasnain. Slow-light optical buffers: capabilities and fundamental limitations. *J. Lightwave Technol.*, 23:4046, 2005.

[60] J. Capmany, B. Ortega, D. Pastor, and S. Sales. Discrete-time optical processing of microwave signals. *J. Lightwave Technol.*, 23:702, 2005.

[61] C. Chang-Hasnain, P.-C. Ku, J. Kim, and S.-L. Chuang. Variable optical buffer using slow-light in semiconductor nanostructures. *Proc. IEEE*, 91(1884), 2003.

[62] P. Kaer Nielsen, H. Thyrrestrup, J. Mørk, and B. Tromborg. Numerical investigation of electromagnetically induced transparency in a quantum dot structure. *Opt. Express*, 15:6396, 2007.

[63] M. van der Poel, J. Mørk, and J. M. Hvam. Controllable delay of ultrashort pulses in a quantum dot optical amplifier. *Opt. Express*, 13:8032–8037, 2005.

[64] A. Uskov, J.Mørk, and J. Mark. Wave mixing in semiconductor laser amplifiers due to carrier heating and spectral-hole burning. *IEEE J. Quantum Electon.*, 30:1769–1781, 1994.

[65] A.P. Bogatov, P.G. Elissev, O.G. Okhotnikov, M.P. Rakhval'skii, and K.A.Khairetdinov. Interaction of modes and self-stabilization of single-frequency emission from injection lasers. *Sov. J. Qauntum Electronics*, 13:1221–1229, 1983.

[66] H. Su, P. K. Kondratko, and S. L. Chuang. Variable optical delay using population oscillation and four-wave-mixing in semiconductor optical amplifiers. *Opt. Express*, 14:4800–4807, 2006.

[67] H. Su and S. L. Chuang. Room temperature slow and fast light in quantum dot semiconductor optical amplifiers. *Applied Phys. Lett.*, 88(6):061102, 2006.

[68] C. Chang-Hasnain and S. L. Chuang. Slow and fast light in semiconductor quantum-well and quantum-dot devices. *J. Lightwave Technol.*, 24:4642, 2006.

[69] T.Liu, K. Obermann, K. Petermann, F. Girardin, and G. Guekos. Effect of saturation cased by amplified spontaneous emission on semiconductor optical amplifier performance. *Opt. Lett.*, 33(24):2042–2043, 1997.

[70] P. K. Kondratko and S. L. Chuang. Slow-to-fast light using absorption to gain switching in quantum-well semiconductor optical amplifier. *Opt. Express*, 15:9963–9969, 2007.

[71] K. Yvind F. öhman and J. Mørk. Voltage-controlled slow light in an integrated semiconductor structure with net gain. *Opt. Express*, 14:9955–9962, 2006.

[72] F. öhman. Slow light in a semiconductor waveguide for true-time delay applications in microwave photonics. *IEEE Photonic. Technol. Lett.*, 19:1145–1147, 2007.

[73] W. Xue, Y. Chen, F. Öhman, S. Sales, and J. Mørk. Enhancing light slow-down in semiconductor optical amplifiers by optical filtering. *Opt. Lett.*, 21:1084–1086, 2008.

[74] Y. Chen, W. Xue, F. Öhman, and J. Mørk. Theory of optical-filtering enhanced slow and fast light effects in semiconductor optical waveguide. *J. Lightwave Technol.*, 26:3734–3743, 2008.

[75] G.P. Agrawal. *Fiber-optic communication systems.* John Wiley and Sons Ltd., third edition, 2002.

[76] R. J. Manning, A. D. Ellis, A.J. Poustie, and K.J. Blow. Semiconductor laser amplifiers for ultrafast all-optical signal processing. *J. Opt. Soc. Am. B*, 14:3204–3116, 1997.

[77] D. Wolfson, A. Kloch, T. Fjelde, C. Janz, B. Dagens, and M. Renaud. 40-gb/s all-optical wavelength conversion, regeneration and demultiplexing in an

soa-based all-active mach-zehnder interferometer. *IEEE Photonic. Technol. Lett.*, 12:332–334, 2000.

[78] J. Leuthold, B. Mikkelsen, R. E. Behringer, G. Raybon, C.H. Joyner, and P.A.Besse. Novel 3r regeneration based on semiconductor optical amplifier delayed-interference configuration. *IEEE Photonic. Technol. Lett.*, 13:860–862, 2001.

[79] J.De Merlier, G. Morthier, S. Verstuyft, T.Van Caenegem, I. Moerman, P. van Daele, and R. Baets. Experimental demonstration of all-optical regeneration using an mmi-soa. *IEEE Photonic. Technol. Lett.*, 14:660–662, 2002.

[80] W. Freude, R. Bonk, T. Vallatis, A. Marculescu, A. Kapoor, E.K. Sharma, C. Meuer, D. Bimberg, R. Bronot, F. Lelarge, G.H. Duan, C. Koos, and J. Leuthold. Linear and nonlinear semiconductor optical amplifiers. In *2010 International Conference on Transparent Optical Networks (ICTON)*, page We.D4.1, 2010.

[81] C. Knöll, M. Gölles, Z. Bakonnyi, G. Onishchukov, and F. Lederer. Optimization of signal transmission by an in-line semiconductor optical amplifier-saturable absorber module. *Opt. Commun.*, 187:141–153, 2001.

[82] F. Öhman, S. Bischoff, B. Tromborg, and J. Mørk. Noise and regeneration in semiconductor waveguides with saturable gain and absorption. *IEEE J. Quantum Elect.*, 40:245–255, 2004.

[83] M.J.R. Heck, A.J.M. Bente, Y. Barbarin, D. Lenstra, and M.K. Smit. Monolithic semiconductor waveguide device concept for picosecond pulse amplification, isolation and spectral shaping. *J. Quantum Elect.*, 43:910–922, 2007.

[84] M.J.R. Heck, A.J.M Bente, Y. Barbarin, A. Fryda, H-D Jung, Y-S Oei, R. Notzel, D. Lenstra, and M.K.Smit. Pulse shaping - characterization of a monolithic concaternated soa/sa waveguide device for picosecond pulse amplification and shaping. *J. Quantum Elect.*, 44:360, 2008.

[85] F. Öhman, R. Kjaer, L.J. Christiansen, K. Yvind, and J. Mørk. Steep and adjustable transfer functions of monolithic soa-ea 2r regenerators. *IEEE Photonic. Technol. Lett.*, 18:1067, 2006.

[86] T. Vivero, N. Calabretta, I.T. Monroy, G. Kassar, F. Öhman, K.Yvind, A.P. González-Marcos, and J. Mørk. 2r-regeneration in a monolithically integrated four-section soa-ea chip. *Opt. Commun.*, 282:117–121, 2009.

[87] J. Xu and J. Mørk X. Zhang. Investigation of patterning effects in ultrafast soa-based optical switches. *J. Quantum Elect.*, 46:87–94, 2010.

[88] A. V. Uskov, T.W.Berg, and J. Mørk. Theory of pulse-train amplification without patterning effects in quantum dot semiconductor optical amplifier. *J. Quantum Elect.*, 40:306–320, 2004.

[89] R. Loudon. *The Quantum Theory of Light.* Oxford Unviersity Press, second edition edition, 1983.

[90] W.W. Chow, S.W. Koch, and M. Sargent III. *Semiconductor-Laser Physics.* Springer-Verlag, 1994.

[91] H. Haug and S.W. Koch. *Quantum theory of the optical and electronic properties of semiconductors.* World Scientific Publishing, fourth edition edition, 2004.

[92] W.W. Chow and S.W. Koch. *Semiconductor-Laser Fundamentals: Physics of the gain materials.* Berlin, Germany: Springer-Verlarg, 1999.

[93] M. Asada and Y. Suematsu. Density matrix theory of semiconductor lasers with relaxation broadening model - gain and gain suppression in semiconductor lasers. *IEEE J. Quantum Elect.*, QE-21:434–441, 1985.

[94] N. Ogasawara and R. Ito. Longitudinal mode competition and asymmetric gain saturation in semiconductor injection lasers. ii. theory. *Jap. J. Appl. Phys.*, 27:615–626, 1988.

[95] J. Mørk and A. Mecozzi. Theory of the ultrafast optical response of active semiconductor waveguides. *J. Opt. Soc. Am. B*, 13:1803–1816, 1996.

[96] B. Thomas and K. Ferenc. Nonlinear optical pulse propagation in the single-cycle regime. *Phys. Rev. Lett.*, 78:3282–3285, Apr 1997.

[97] T.W. Berg, S. Bischoff, I. Magnusdottir, and J. Mørk. Ultrafast gain recovery and modulation limitations in self-assembled quantum-dot devices. *IEEE Photonic. Technol. Lett.*, 13:541–543, 2001.

[98] L.A. Colden and S.W. Corzine. *Diode Lasers and Photonic Integrated Circuits*. John Wiley and Sons, Inc., 1995.

[99] S.L. Mccall and E.L. Hahn. Self-induced transparency by pulsed coherent light. *Phys. Rev. Lett.*, 18:908–911, May 1967.

[100] R. W. Ziolkowski, J. M. Arnold, and D. M. Gogny. Ultrafast pulse interactions with two-level atoms. *Phys. Rev. A*, 52(4):3082–3094, October 1995.

[101] S. Hughes. Breakdow of the area theorem: carrier-wave rabi flopping of femtosecond optcial pulses. *Phys. Rev. Lett.*, 81:3363–3366, October 1998.

[102] O.D. Mücke, T.Tritschler, M. Wegener, U. Morgner, and F. X. Kärtner. Signatures of carrier-wave rabi flopping in gaas. *Phys. Rev. Lett.*, 87:057401–1–4, 2001.

[103] H. Giessen, S. Linden, J. Kuhl, A. Knorr, S.W. Koch, M. Hetterich, M. Grün, and C. Klingshirn. High-intensity pulse propgation in semiconductors: on-resonant self-induced transmission and effects in the continuum. *Opt. Express*, 4:121–128, 1999.

[104] A. Knorr, R. Binder, M. Lindberg, and S.W. Koch. Theoretical study of resonant ultrashort-pulse propagation in semiconductors. *Phy. Rev. A*, 46(11):7179–7186, 1992.

[105] M. Okumura, T. Sugawara, and H. Tanimoto. An efficient small signal frequency analysis method for nonlinear circuits with two frequency excitations. *IEEE T. Comput. Aid D.*, 9(3):225–235, 1990.

[106] O. Nastov, R. Telichevesky, K. Kundert, and J. White. Fast simulation algorithms for rf circuits. In *Proceedings of THE IEEE*, volume 95 of *3*, pages 600–621, 2007.

[107] E. Malic, M. Richter, G. Hartmann, J. Gomis-Bresco, U. Woggon, and A. Knorr. Analytical description of gain depletion and recovery in quantum dot optical amplifiers. *New Journal of Physics*, 12:063012, 2010.

[108] M. Grupen and K. Hess. Simulation of carrier transport and nonlinearities in quantum-well laser diodes. *IEEE J. Quantum Elect.*, 28:1990–2008, 1998.

[109] K.Y. Lau. ***Quantum Well Lasers*** *Ch 5 Dynamics of quantum well lasers*. Boston, MA:Academic, 1993.

[110] A. Markus and A. Flore. Modeling carrier dynamics in quantum dot lasers. *Phys. Stat. Sol. A*, 201:338–344, 2004.

[111] J. Mark and J. Mørk. Subpicosecond gain dynamics in ingaasp optical amplifiers: Experiment and theory. *Appl. Phys. Lett.*, 61:2281–2283, 1992.

[112] H. Ju, A.V. Uskov, R. Nötzel, Z. Li, J. Molina Vázquez, D. Lenstra, G.D. Khoe, and H.J.S.Dorren. Effects of two-photon absorption on carrier dynamics in quantum-dot optical amplifiers. *Appl. Phys. B*, 82:615–620, 2006.

[113] P. Blood. On the dimensionality of optical absorption, gain and recombination in quantum-confined structure. *IEEE J. Quantum Elect.*, 36, 2000.

[114] S.W. Osborne, P. Blood, P.M. Smowton, Y. C. Xin, A. Stintz, D. Huffaker, and L.F. Lester. Optical absorption cross section of quantum dots. *J. Phys.-Condens. Mat.*, 16:S3749–S3756, 2004.

[115] L.F. Shampine and M. W. Rechelt. The matlab ode suite. *SIAM Journal on Scientific computing*, 18:1–22, 1997.

[116] D. C. Hutchings, M. Sheik-bahae, D. J. Hagan, and E.W. Van Stryland. Kramers-krönig relations in nonlinear optics. *Opt. Quant. Electron.*, 24:1–30, 1992.

[117] F.W. King. Numerical evaluation of truncated kramers-kronig transforms. *J. Opt. Soc. Am. B*, 24:1589–1595, 2007.

[118] T.C. Newell, D.J. Bossert, A. Stintz, B. Fuchs, K.J. Malloy, and L.F. Lester. Gain and linewidth enhancement factor in inas quantum-dot laser diodes. *IEEE Photon. Technol. Lett.*, 11:1527–1529, 1999.

[119] J. Muszalski, J. Houlihan, G. Huyet, and B. Corbert. Measurement of linewidth enhancement factor in self-assembled quantum dot semiconductor lasers emitting at 1310nm. *Electron. Lett.*, 40:428–430, 2004.

[120] S. Schneider, P. Borri, W. Langbein, U. Woggon, R.L. Sellin, D. Ouyang, and D. Bimberg. Linewidth enhancement factor in ingaas quantum-dot lasers. *J. Quantum Elect.*, 40:1423–1429, 2004.

[121] B. Dagens, A. Markus, J.X.Chen, J.-G. Provost, D. Make, O. Le gouezigou, J. Landreau, A. Fiore, and B. Thedrez. Giant linewidth enhancement factor and purely frequency modulated emission from quantum dot lasers. *Electron. Lett.*, 41:323–324, 2005.

[122] J. Oksanen and J. Tulkki. Linewidth enhancement factor and chirp in quantum dot lasers. *J. Appl. Phys.*, 94:1983–1989, 2003.

[123] H.C. Wong, G.B. Ren, and J.M. Rorison. Mode amplification in inhomogeneous qd semiconductor optical amplifiers. *Opt. Quant. Electron.*, 38:395–409, 2006.

[124] M. Willatzen, T. Tanaka, Y. Arakawa, and J. Singh. Polarization dependence of optoelectronic properties in quantum dots and quantum wires - consequences of valence-band mixing. *J. Quantum Elect.*, 30:640–653, 1994.

[125] H.C. Schneider, W.W. Chow, and S.W. Koch. Anomalous carrier-induced dispersion in quantum-dot active media. *Phys. Rev. B*, 66:041310–1–4, 2002.

[126] A.V. Uskov, E.P.O'Reilly, D.McPeake, N.N. Ledentsov, D.Bimberg, and G. Huyet. Carrier-induced refractive index in quantum dot structures due to transitions from discrete quantum dot levels to continuum states. *Appl. Phys. Lett.*, 84:272–274, 2004.

[127] S. Melnik, G. Huyet, and A. V. Uskov. The linewidth enhancement factor α of quantum dot semiconductor lasers. *Opt. Express*, 14:2950–2955, 2006.

[128] J. Kim, C. Meuer, D. Bimberg, and G. Eisenstein. Numerical simulation of temporal and spectral variation of gain and phase recovery in quantum-dot semiconductor optical amplifiers. *IEEE J. Quantum Elect.*, 46:405 –413, march 2010.

[129] A.V. Uskov, E.P. O'Reilly, R.J. Manning, R.P. Webb, D. Cotter, M. Laemmlin, N.N. Ledentsov, and D.Bimberg. On ultrafast optical switching based on

quantum-dot semiconductor optical amplifiers in nonlinear interferometers. *IEEE Photonic. Technol. Lett.*, 16:1265–1267, 2004.

[130] M. Tessler, R. Nagar, and G. Eisenstein. Structure dependent modulation responses in quantum-well lasers. *J. Quantum Elect.*, 28:2242–2250, 1992.

[131] A.V. Uskov, E.P. O'Reilly, M. Laemmlin, N.N. Ledentsov, and D. Bimberg. On gain saturation in quantum dot semicondcutor optical amplifiers. *Opt. Commun.*, 248, 2005.

[132] P. W. Juodawlkis, J. J. Plant, J.P. Donnelly, A. Motamedi, and E.P. Ippen. Continuous-wave two-photon absorption in a watt-class semiconductor optical amplifier. *Opt. Express*, 16:12387–12396, 2008.

[133] T. W. Berg, J. Mørk, and J. M. Hvam. Gain dynamics and saturation in semiconductor quantum dot amplifiers. *New Journal of Physics*, 6:178–1–23, 2004.

[134] A. Uskov and C. J. Chang-Hasnain. Slow and superluminal light in semiconductor optical amplifiers. *Electron. Lett.*, 41:922–924, 2005.

[135] A. Uskov, F. Sedgwick, and C. J. Chang-Hasnain. Delay limit of slow light in semiconductor optical amplifiers. *IEEE Photonic. Technol. Lett.*, 18:731–733, 2006.

[136] Y. Chen, F. Öhman, W. Xue, and J. Mørk. Analysis of an effective optical filtering technique to enhance microwave phase shifts based on slow and fast light effects. In *CLEO 2008*, page CME4, San Jose,CA, USA, 2008.

[137] B. Pesala, Z. Cheng, A.V. Uskov, and C. J. Chang-Hasnain. Experimental demonstration of slow and superluminal light in the semiconductor optical amplifiers. *Opt. Express*, 14:12968–12975, 2006.

[138] Y. Shi, L. Yan, and A. E. Willner. High-speed electrooptic modulator characterization using optical spectrum analysis. *J. Lightwave Technol.*, 21:2358–2367, 2003.

[139] G. P. Agrawal. Population pulsations and nondegenerated four-wave mixing in semiconductor lasers and amplifiers. *J. Opt. Soc. Am. B*, 14:147–159, 1988.

[140] M.R. Fisher and S.L. Chuang. A microwave photonic phase-shifter based on wavelenth conversion in a dfb laser. *IEEE Photonic. Technol. Lett.*, 18:1714–1716, 2006.

[141] J. Mørk, F. Öhman, M. Van der Poel, Y. Chen, P. Lunnemann, and K. Yvind. Slow and fast light: controlling the speed of light using semiconductor waveguides. *Laser Photon. Rev.*, 3:30–44, 2009.

[142] A. Matsudaira. Electrically tunable slow and fast lights in a quantum-dot semiconductor optical amplifier near 1.55μm. *Opt. Lett.*, 32:2894–2896, 2007.

[143] G. Bramann, H.J. Wunsche, U.Busolt, C. Schimdt, M. Schlak, B. Sartorious, and H.P. Nolting. Two-wave competition in ultralong semiconductor optical amplifiers. *J. Quantum Elect.*, 41:1260–1267, 2005.

[144] N. Cheng and J.C. Cartledge. Measurement-based model for cross-absorption modulation in an mqw electroabsorption modulator. *J. Lightwave Technol.*, 22:1805–1810, 2004.

[145] D.J. Derickson, R.J. Helkey, A. Mar, J.R. Karin, J.G. Wasserbauer, and J.E. Bowers. Short pulse generation using multisegment mode-locked semiconductor lasers. *J. Quantum Elect.*, 28:2186–2202, 1992.

[146] A. Uskov, J. Mørk, and J. Mark. Theory of short-pulse gain saturation in semiconductor laser amplifiers. *IEEE Photonic. Technol. Lett.*, 4:443–446, 1992.

[147] P. Borri, S.Scaffetti, J. Mørk, W. Langbein, J.M. Hvam, A. Mecozzi, and F. Martelli. Measurement and calculation of critical pulsewidth for gain saturaiton in semiconductor optical amplifiers. *Opt. Commun.*, 164:51–55, 1999.

[148] D.B. Malins, A. Gomez-Iglesias, S.J. White, W.Sibbert, A. Miller, and E.U. Rafailov. Ultrafast electroabsorption dynamics in an inas quantum dot saturable absorber at 1.3μm. *Appl. Phys. Lett.*, pages 171111–1–3, 2006.

[149] A.R. Rae, M.G. Thompson, R.V. Penty, and I.H. White. Dynamic simulation of mode-locked quantum-dot laser. In *CLEO 2008*, page CTHF1, 2008.

[150] J.D. Jackson. *Classical Electrodynamics*. John Wiley and Sons, Inc., 1975.

[151] G.P. Agrawal. *Nonlinear Fiber Optics.* Academic Press, third edition, 2001.

[152] Y.R. Shen. *The principles of nonlinear optics.* J. Wiley and Sons, New York, 1984.

[153] H.A. Haus. *Electromagnetic fields and energy.* Prentice Hall., 1989.

[154] J. Laegsgaard. Mode profile dispersion in the generalised nonlinear schrödinger equation. *Opt. Express*, 15:16110–16123, 2007.

[155] T. D. Visser, H. Blok, B. Demeulenaere, and D. Lenstra. Confinement factors and gain in optical amplifiers. *IEEE J. Quantum. Elect.*, 33(10):1763–1766, 1997.

[156] A. Mecozzi and J. Mørk. Theory of heterodyne pump-probe experiments with femtosecond pulses. *J. Opt. Soc. Am. B*, 13:2437–2452, 1996.

[157] M. Sargent III, M. Q. Scully, and W.E. Lamb Jr. *Laser Physics.* Addison-Wesley Publication Co. Reading, MA, 1974.

[158] K. L. Hall, G. Lenz, and Erich P. Ippen. Femtosecond time domain measurements of group velocity dispersion in diode lasers at 1.5μm. *J. Lightwave Technol.*, 10:616–619, 1992.

[159] C.H. Henry. Theory of the linewidth of semiconductor lasers. *J. Quantum Elect.*, QE-18:259–264, 1982.

[160] I. Vurgaftman, J.R. Meyer, and L.R. Ram-Mohan. Band parameters for iii-v semiconductor and their alloys. *J. Appl. Phys.*, 89:5815–5875, 2001.